Development of lab-on-a-chip acoustofluidic platform with a potential application in extracellular vesicles purification

by

Erfan Taatizadeh

B.Sc., K. N. Toosi University of Technology, 2017

A THESIS SUBMITTED IN PARTIAL FULFILLMENT OF
THE REQUIREMENTS FOR THE DEGREE OF

MASTER OF APPLIED SCIENCE

in

THE COLLEGE OF GRADUATE STUDIES

(Mechanical Engineering)

THE UNIVERSITY OF BRITISH COLUMBIA

(Okanagan)

December 2019

The following individuals certify that they have read, and recommend to the College of Graduate Studies for acceptance, a thesis/dissertation entitled:

Development of lab-on-a-chip acoustofluidic platform with a potential application in extracellular vesicles purification

---

submitted by Erfan Taatizadeh in partial fulfillment of the requirements of

the degree of Master of Applied Science

Dr. Mina Hoorfar, School of Engineering, Faculty of Applied Science

---

Supervisor

Dr. Isaac T. S. Li, Department of Chemistry, Irving K. Barber School of Arts and Sciences

---

Co-supervisor

Dr. Homayoun Najjaran, School of Engineering, Faculty of Applied Science

---

Supervisory Committee Member

Dr. Jonathan F. Holzman, School of Engineering, Faculty of Applied Science

---

Supervisory Committee Member

Dr. Chen Feng, School of Engineering, Faculty of Applied Science

---

University Examiner

Abstract

Extracellular vesicles (EVs) play an important role in intercellular communication, as they are responsible for the transportation of proteins from their cells of origin to other locations within the body. They are found in a variety of bodily fluids and have proven to be promising candidates for the early diagnosis of different types of diseases. To use EVs as diagnostic tools their purification is a prerequisite step. Traditional methods of EV purification are time-consuming and expensive and can lead to morphology disruptions due to high induced shear stress. To address these problems, novel lab-on-a-chip-based purification methods have been employed. Among various methods introduced for separation and purification of EVs, cells, and synthetics microparticles, acoustofluidics (i.e., a combination of microfluidics and acoustics) has been one of the most effective methods. Unlike common separation techniques carried out in clinical laboratories that are based on chemical properties, the acoustofluidic process relies on the physical properties of the sample. Using acoustofluidics, the manipulation of cells and microparticles can be achieved in a label-free, contact-free, and highly biocompatible manner. This thesis reviews two types of acoustofluidic platforms which work based on parallel standing surface acoustic wave (pSSAW) and tilted standing surface acoustic wave (tSSAW). pSSAW is mainly used for microparticle alignments while tSSAW is implemented for microparticle separation based on particle size differences. In order to optimize the functionality of the aforementioned platforms, a two-dimensional numerical simulation has been established in this thesis. Such a model has subsequently followed by an experimental test using the pSSAW method. The numerical simulation is used to investigate the effects of the platform geometrical and operational conditions on the separation efficiency. Next, the optimal values are tested in an experimental setting to validate the optimal parameters and conditions. A similar experimental approach is applied to

design and test the tSSAW platform although numerical simulation cannot be developed as such geometry requires three-dimensional modeling which is computationally expensive. Using the tSSAW chip, a separation efficiency of > 90% is demonstrated for the separation of 0.6 μm microparticles from 15 μm and 20 μm microparticles by adjusting the operational conditions.

Lay Summary

The bodily fluids have a nanoscale size biological component called extracellular vesicles (EVs). One of the important applications of EVs is in the early diagnosis of various diseases. The separation of these biological components is a prerequisite and inevitable step. However, traditional separation methods have not shown high efficiency and they could be extremely time-consuming. To eliminate the drawbacks associated with the traditional isolation methods, researchers have been developing alternative novel isolation methods based on miniaturized devices called lab-on-a-chip platforms. In this study, we show the potential integration of the sound waves energy into lab-on-a-chip platforms regarding the separation of EVs in a cost-effective and efficient manner. In this research, such platforms are optimized by carrying out numerical simulation and experimental studies. Results obtained have shown the high capabilities of the aforementioned device in a successful EVs like microparticles isolation.

Preface

The research presented in this thesis is the original work performed by the author. This thesis was supervised by Dr. Mina Hoorfar at the Advanced Thermo-Fluidic Laboratory (ATFL) in School of Engineering, Faculty of Applied Science and co-supervised by Dr. Isaac T. S. Li at the Single Molecule Mechano-Biology Lab (SMMBL) in Department of Chemistry, Irving K. Barber School of Arts and Sciences, University of British Columbia, Okanagan Campus. Parts of this thesis have been published in different journals and presented at conferences. The details of the publications and the author's contributions to them are explained below:

a. Refereed journal publications

[1] Li, X., Corbett, A.L., Taatizadeh, E., Tasnim, N., Little, J.P., Garnis, C., Daugaard, M., Guns, E., Hoorfar, M. and Li, I.T., 2019. Challenges and opportunities in exosome research—Perspectives from biology, engineering, and cancer therapy. APL bioengineering, 3(1), p.011503 - Used with permission.

Contribution: My contribution in this paper included the following: (i) reviewing the relevant published papers regarding the lab-on-a-chip (microfluidics-based) isolation techniques for EVs and exosomes purification, (ii) writing section V titled "Isolation", and (iii) revising a manuscript.

[2] Taatizadeh, E., Li, I., Hoorfar, M., "Numerical simulation of the microscale acoustofluidic driven device by standing surface acoustic wave", To be submitted.

Contribution: My contribution in this paper included the following: (i) the development of the numerical simulation, (ii) conducting the experiment, and (iii) writing the paper.

[3] Taatizadeh, E., N., Li, I., Hoorfar, M., “Nano-scale particle separation with tilted standing surface acoustic wave—Experimental and numerical approaches”, To be submitted.

Contribution: My contribution in this paper included the following: (i) the development of the numerical simulation, (ii) conducting the experiment, and (iii) writing the paper.

b. Conference proceedings and presentations

[1] Poster presentation, “Acoustophoretic-based microfluidic platform for sorting extracellular vesicles”, Erfan Taatizadeh, Arash Dalili, Nishat Tasnim, Cathie Garnis, Mads Daugaard, Isaac Li, Mina Hoorfar, International Society for Extracellular Vesicles 2019 (ISEV 2019), Kyoto, Japan.

Contribution: My contribution to this poster presentation included the following: (i) developing the numerical simulation, (ii) providing the simulation results, (iii) preparation of the poster, and (iv) attending the conference and presentation of the poster to audiences.

[1] Dalili, A., Taatizadeh, E. and Hoorfar, M., 2018. Characterization of the electrodes of DEP-based micro-separator.

Contribution: My contribution to this poster presentation included the following: (i) developing the numerical simulation, (ii) providing the simulation results, and (iii) participating in the manuscript preparation.

Table of Contents

List of tables

List of figures

List of symbols

ρ	Density
T	Temperature
t	Time
g	Gravity acceleration
u	Acoustic velocity
mg	Milligram
μm	Micrometer
Å	Angstrom
L	Liter
μL	Microliter
s	Second
min	Minute
d_P	Microparticle diameter
d_c	Cutoff size microparticle diameter
MHz	Megahertz
H_i	Height of the corresponding medium
W_i	Width of the corresponding medium

U	Acoustic potential field
P_0	Acoustic pressure
K^2	Electromechanical coupling constants
v_f	Sound wave velocity in the free substrate
v_m	Sound wave velocity measured along a short-circuited plane
λ_{SAW}	Surface acoustic wave wavelength
c_i	Speed of sound in the corresponding medium
f_0	Resonance frequency
F_{rad}	Acoustic radiation force
ϕ	Acoustic contrast factor
V_p	Volume of the microparticle
β	Compressibility
k	Wave number
x	Distance from a pressure node
σ	Mechanical stress vector
C	Elasticity matrix
ϵ	Strain vector
e	Piezoelectric stress matrix

tr	Transpose of a matrix
E	Electric field vector
D	Electric displacement vector
ε	Dielectric matrix
φ	Electrical potential
ω	Angular frequency
α	Attenuation coefficient
μ	Dynamic viscosity
μ_B	Bulk viscosity
θ_R	Rayleigh angle
N_P	Number of IDT finger
N	Newton
nN	Nano Newton
PN	Pico Newton
V_0	Applied voltage
Z	Acoustic impedance
θ	Microchannel tilt angle
A	Aperture length

B	Bandwidth
A_c	Aperture cut-off length
D_F	Distance between two pair of IDTs edges
F	Fresnel parameter
Q_c	Flow rata threshold value
∇	Nabla/Del operator
%	Percentage
COP_{rad}	Acoustic coefficient of performance

List of abbreviations

1D	One-dimensional
2D	Two-dimensional
3D	Three-dimensional
ABs	Apoptotic bodies
AC	Alternating current
Al	Aluminum
AP	Acoustic pressure
APM	Acoustic plate mode
ARF	Acoustic radiation force
ASF	Acoustic streaming flow
Au	Gold
AVE	Average
BAW	Bulk acoustic wave
BCs	Boundary conditions
Cr	Chromium
DI water	Deionized water
EVs	Extracellular vesicles

EXOs	Exosomes
FEM	Finite element method
HDL	High-density lipoproteins
HIV	Human Immunodeficiency Virus
HSW	Harmonic standing waves
IDT	Interdigital transducer
IPA	Isopropyl alcohol
LDL	Low-density lipoproteins
$LiNbO_3$	Lithium niobate
$LiTaO_3$	Lithium tantalate
LSAW	Leaky surface acoustic wave
mRNA	messenger ribonucleic acids
MVs	Microvesicles
PANs	Pressure anti-nodes
PBS	Phosphate-buffered saline
PDMS	Polydimethylsiloxane
PLTs	Platelets
PNs	Pressure nodes

PS	Polystyrene
pSSAW	parallel Standing surface acoustic wave
RBCs	Red blood cells
RF	Radiation frequency
RPM	rotation per minute
SAW	Surface acoustic wave
SSAW	Standing surface acoustic wave
Ti	Titanium
TSAW	Travelling surface acoustic wave
tSSAW	tilted Standing surface acoustic wave
UC	Ultracentrifugation
UF	Ultrafiltration
UV	Ultraviolet
WBCs	White blood cells

Acknowledgments

First and foremost, I would like to express my sincere gratitude to my amazing parents for all their sacrifices and devotion. Without their permanent support, none of these achievements would have been possible. Great thanks to my sister, for bringing happiness and encouragement to my life.

I would like to express my deepest appreciation to my supervisor, Dr. Mina Hoorfar, for all her support during my master's journey. I remembered the day we met for the first time, January 4th, 2018. You with your welcoming manner caused all of my stress and uncertainties to go away. You taught me to believe in myself and accept challenges. Many thanks to my co-supervisor, Dr. Isaac T. S. Li, for providing me continuous support and encouragement. I had the privilege of working with both my supervisors for guiding my studies in the best direction.

During my master's., I was honored to work with hard-working, attentive and supportive lab manager, Nishat Tasnim, and my labmates who providing a friendly academic atmosphere which made conducting research delightful. My special thanks to Dr. Arash Dalili and Pamela Ines Rellstab for his permanent support, mentorship, and companionship since the beginning of my master's study.

There were some moments I told myself that I cannot continue anymore. There are some moments in your life that you only could share with a few people who can truly understand you without judging. I would like to send my deepest appreciation to those who made this journey memorable.

And last but not least, I would like to thank myself! There are some moments in everyone's life when they are in doubt. Whenever I am thinking about the past, I truly could manage and solve all of the problems step by step by considering all aspects and consequences. Of course, there were some inevitable mistakes, but you should only consider them as lessons should be learned. BELIEVE IN YOURSELF!

Dedication

Parents are life givers! To my beloved parents for all of the sacrifices, they have made…

To my favorite scientist and his inspirational quote that I will never forget:

"Imagination is more important than knowledge. For knowledge is limited, whereas imagination embraces the entire world, stimulating progress, giving birth to evolution."

Albert Einstein

Chapter 1: Introduction[1]

1.1 Background

1.1.1 Extracellular Vehicles (EVs) and their role in clinical uses

EVs are small cell-derived vesicles that range in size from $30\ nm$ to $1\ \mu m$ [2], [3]. They can be found in various body fluids such as blood, urine, saliva, and milk [4], [5]–[7]. EVs have an important role in intercellular communication [8]–[12], molecular exchange [13], viral transfer (Human Immunodeficiency Virus (HIV)) [14] and cell signaling [3] as they carry valuable molecular components of their parent cells such as proteins, lipids, and messenger ribonucleic acids (mRNAs) [13], [15]–[19]. These components are promising tools for disease biomarkers detection, drug delivery vehicles, and vaccinate candidate's development [3], [20], [21]. Additionally, the disease states and responses to medications can be monitored by checking the status of the EVs [3] highlighting their importance and potential as a pathway to personalized medicine [22]. It is not an over-exaggeration that EVs are the future of biomarkers in medicine [23]. Previous studies reported applications of EVs in diseases diagnosis such as cardiovascular [24], diabetes [7], [25], central nervous system, Alzheimer's [26]–[28], Parkinson's [29], [30], chronic hepatitis C [31], [32], acute kidney injury [33]–[35], and the most important one, cancer [36]–[41] which have been the main focus of researchers over the last decades [2], [42]–[45].

1.1.2 Challenges in EVs purification

The efficient purification of EVs is a prerequisite step for the clinical usages. The main challenge of EVs purification is their nano-scale sizes [1]. Another challenge in EVs purification is their size

[1] The information presented in this chapter have been previously published [1] and are utilized with permission of the publisher.

overlaps with other biological components of biofluids such as high-density lipoproteins (HDLs), low-density lipoproteins (LDLs), and chylomicrons [6], [46]. Various methods have been introduced to overcome these drawbacks. These methods can be classified into two subgroups: traditional and microfluidics-based methods (Li et al. [1] called these methods established protocols and emerging protocols, respectively). Unlike the low efficiency and recovery yield demonstrated by most traditional methods [47], microfluidics platforms (mainly applied to EVs isolation after 2010 [48].) have shown to be powerful devices for EVs' purification by offering high purity, low sample volume consumption, high sensitivity, and reduced procedural costs [49]–[52].

1.2 Literature review

1.2.1 Traditional methods of EVs isolation

The traditional methods of EVs purification have been widely used in the last decades in laboratories and clinics [53]. These methods isolate EVs either based on their physical properties such as density and/or size or their chemical properties such as surface biomarkers. The following sections discuss working principles, advantages, and demerits of various traditional methods of the EVs purification.

The purification of EVs based on their density can be accomplished by ultracentrifugation (UC) with and without a density gradient [54], [55]. UC is currently the "gold-standard" method in EVs purification and has been used in laboratories [54] where roughly 56% of all EVs purification is performed by this technique [56]. By applying centrifugal forces, the components of the sample are separated according to their size, density, and viscosity. Typically, live or dead cell and cell debris are first removed as pellets at a lower speed (300×g to 1000×g), and the supernatant is

carefully aspirated and used for the next round of centrifugation. Finally, ultracentrifugation is carried out at 100,000×g for 70 mins to obtain the pellet of EVs [54]. Despite the popularity of the UC method, it has some inevitable drawbacks: it is an extremely time-consuming process (normally lasting between 5-10 hours or more [3], [57]–[59]) and it has low recovery rates (ranging between 5% and 25% [60]) [20], [55], [61]. These last two factors lead to the need for large sample volumes for isolation. Furthermore, EVs' morphology disruption is another inevitable outcome of the high centrifugal forces [62]–[64].

Ultrafiltration (UF) is another common EVs purification method which is often combined with UC, replacing a few low-speed rounds of spinning in the UC method with filtration [20]. A nanoporous membrane with the typical pore size ranging between 0.1 to 0.001 μm [20], [65] is used to filter the suspension of bioparticles that are sorted out based on their sizes [66]. Compared to the UC technique, UF method has shown higher purity (5-folds higher compare to UC) of isolated EVs as well as less time consumption (1 to 2 hours) [67], [68]. Despite the advantages of UF, trapping bioparticles in nanopores can cause clogging issues resulting in low recovery rates [69]. Furthermore, due to the high forces applied to bioparticles as they pass through nanopores, high shear stress can be generated which may change the morphology of EVs or even cause lysis.

Aside from density and size-based separation techniques, EVs isolation can be performed based on the functionality of biomolecules such as the immunoaffinity-based techniques [66]. In these methods, the chemical properties of bioparticles' surfaces play vital roles in the separation process. Each type of EVs has specific proteins on its surfaces that interact with their specific antibodies. Thus, EVs can be pulled down from other components of the sample [20], [70], [71]. EVs can be isolated by immobilizing these antibodies on various surfaces such as magnetic beads, plates, chromatography matrices, and microfluidic platforms [10], [16], [50]. As an example of the

immunoaffinity-based EVs isolation, Zarovni et al. [56] found that antibody-coated magnetic particles can provide a similar efficiency as UC using only a small amount of the cell culture supernatant (0.1 mL). In this method, an external force displaces the bonded magnetic beads and bioparticles to the area of interest. They found that even higher yields (10 to 15 times higher than UC) can be obtained using the plasma sample instead of the cell culture supernatant. Tauro et al. [55] reported that immunoaffinity isolation provides a higher purity (about triple times compare to the UC method. The main drawback of this method is that large quantities of biological samples cannot be processed [72]. Instead, only pre-concentrated small volumes are suitable for this method [20], [54].

1.2.2 Microfluidic-based EVs isolation

Though still at the early stages of development, microfluidics-based cell/microparticle manipulation technologies have shown great potential due to low sample and reagent volumes consumption, high product purity, high sensitivity, ease of use, and short isolation time [73], [74]. Microfluidic platforms generally include micron-sized channels for processing small amounts of fluid (microliter to picolitre) [75], [76]. Most of the microfluidic devices are fabricated with a specific polymer called polydimethylsiloxane (PDMS) [75] which is optically transparent and biocompatible [77]. Microfluidic devices can have different components based on their applications as well as the approach of separation. These components include microchannels, connecting tubes, microvalves, micromixers and micropumps [75], [78], [79]. Generally, microfluidic-based isolation methods are classified into two main groups: active and passive methods. In the first group, the isolation is performed by the action of external forces, while in the second one, the hydrodynamic and surface forces play the main roles in the isolation [80], [81].

The passive methods (such as filtration [7], [82], [83], [89], immuno-affinity [49], [84]–[86], inertial centrifugation [87], lateral displacement with nanopillar [88], and viscoelastic flow [89]) have higher throughput and also easier configuration as compared to the active methods. However, lower purity in biomolecules separation has been observed using passive methods compared to active methods.

On the other hand, active methods use external forces which can be generated by the electrical field [82], magnetic field [84], [86], and acoustic field [6], [90] for biomolecules sorting and manipulation. Tuning the devices working based on these methods highly depends on operational conditions. Also, the throughput of active methods is relatively lower than that of the passive methods. However, they have shown higher efficiency and purity compared to passive methods. All of the aforementioned active isolation methods rely on the size of the microparticles. However, the main difference of them is the dependency of the acting forces on different physical and/or chemical properties of working samples. As an example, the electrical permittivity and magnetic susceptibility determine the order of the forces exerting to the microparticles in electrical and magnetic-based isolation methods [81]. However, similarities (in terms of the order and sign values) in the electrical permittivity of the microparticles and medium decrease efficiency of the electrical-based isolation method significantly [91]. With a similar approach, the magnetic-based isolation method can be only employed when the microparticles are magnetic. In particular, the acoustofluidic-based isolation method addresses and fulfills these obstacles these issues as it is the only active microfluidic-based isolation method working based on mechanical properties as compared to electrical or magnetic properties. Additionally, it has shown to be a promising tool for biomolecules isolation/recovery due to their cost-effectiveness, ease of fabrication and

capability of label-free and contact-free microparticles/cells manipulation, high biocompatibility, and reproducibility [92]–[94].

1.2.3 Acoustofluidic chip for EVs isolation

Acoustics is one branch of science that has extended from *sound*. It deals with the generation, propagation, and reception of waves in various mediums such as liquid, gas, and solid and covers a vast range of frequencies from the *infrasound* to *ultrasound* [95]. Most biomedical applications of the acoustics have been only developed in *ultrasound*. The acoustics has powerful capabilities in manipulating both fluids and microparticles in the microscale medium [96]. The combination of acoustic with microfluidics initiated a new field in the science called acoustofluidics. The acoustofluidics represents the application of the ultrasonic in the microfluidic platforms. In general, acoustofluidic platforms can be classified into three types based on the acoustic wave guiding process [97]: bulk acoustic wave (BAW) [98], surface acoustic wave (SAW) [99], [100], and acoustic plate mode (APM) [99], [101]. Among them, SAW has been widely used for various biological applications as BAW is limited to the use of high frequency and APM is difficult to operate in a standard oscillator circuit [99]. Surface acoustic waves are mechanical waves that primarily propagate upon the surface of an elastic material. These waves consist of a longitudinal compression motion coupled with a transversal shear motion [92], [93], [102], [103]. The wave generation is achieved by interdigital transducers (IDTs), the comb-shape electrodes which are patterned upon a surface of a piezoelectric material, and the wave propagation continues until they reach the PDMS made microchannel filled with the fluid (e.g. water).

Acoustofluidic-based cell/microparticle isolation has proven itself to be cost-effective, easy to fabricate, label-free, reliable, highly biocompatible as well as being commercially available in compact-sized devices [92]–[94]. Since the operating frequencies of the micro-scale acoustofluidic

chips are in order of tens of MHz, their time scales are smaller than the molecular relaxation time, causing the least possible shear damages [74]. Moreover, comparing to other microfluidic-based isolation methods, it only relies on density, size, and compressibility differences of particles [104], the electrochemical properties of the particles (such as conductivity, permittivity, and surface charges) and the buffers (such as ionic strength and pH) do not influence the separation productivity. All these factors add to the potential of acoustofluidics as a label-free particle/cell

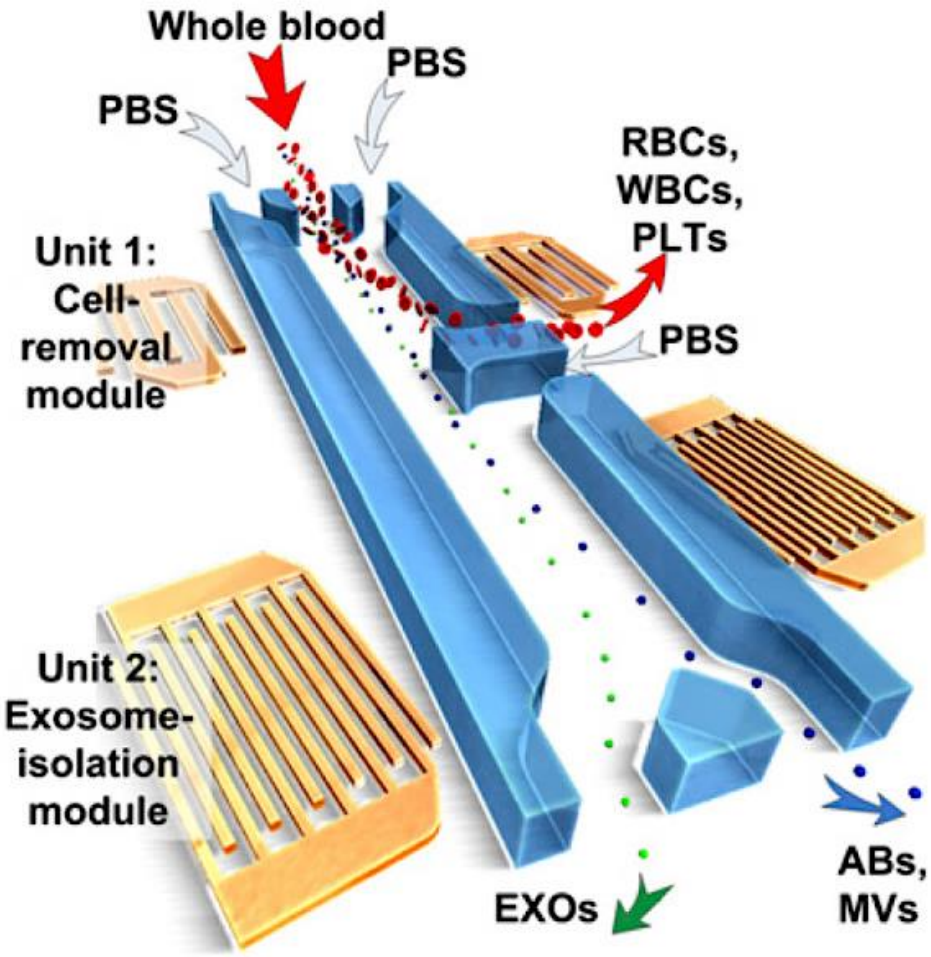

Figure 1-1. Schematic of an acoustofluidic chip used for separation of exosomes (EXOs), apoptotic bodies (ABs), and micro-vesicles (MVs) from the whole undiluted blood. Reproduced from [6] with permission from National Academy of Sciences of the United States of America (PNAS), copyright 2017.

purification method integrated into the microfluidic platforms. SAW-based cell/microparticle manipulation has successfully been applied in various microfluidic applications such as cell/particle washing [105], separation [106], patterning [107], and enrichment [108]. However, only two groups have implemented SAW in the microfluidic devices for EVs isolation. Wu et al. [6] developed a numerical simulation and fabricated an acoustofluidic chip to separate EVs subgroups (exosomes (EXOs), apoptotic bodies (ABs), and micro-vesicles (MVs)) from whole unprocessed and undiluted blood. Their device consisted of two sequential SSAW modules where the first module separates larger bio components of the blood (bigger than 1 μm) such as red blood cells (RBCs), white blood cells (WBCs), and platelet (PLTs). This module creates a cell-free

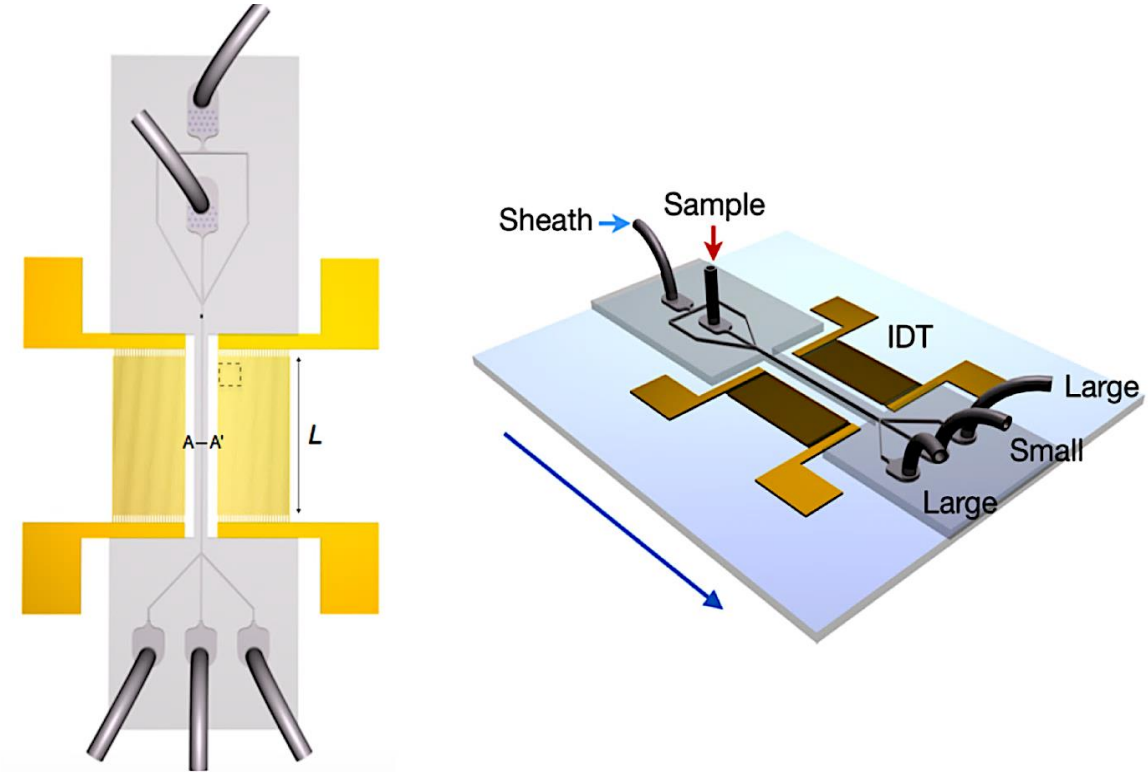

Figure 1-2. Schematic view of the SSAW device. Top view of proposed micro-chip; IDTs (yellow color located on two sides of the microchannel (grey color side). One the right side of the image, isotropic view of micro-chip has been shown; three outlets were used to collect large (Micro-vesicles) and small (Exosomes) components of the input sample. Reproduced from [90] with permission from ACS Nano, ACS Publications, copyright 2015.

plasma used for isolating nanoscale components of the cell-free (Figure 1-1). Their results indicated that less than 0.1% of blood cells remained in the isolated EVs subgroup. However, the main drawback of this work is their numerical simulation which was used to optimize the operating conditions of their chip. They simplified the sound wave propagation phenomena in the fluid and assumed that the direction of the sound wave propagation is perpendicular to the microchannel length. Additionally, they employed simplified numerical simulation (1D) to optimize their proposed device. This approach leads to added bias in prediction of the microparticles migration inside the microchannel as the sound wave propagate in three dimensions.

In another research, Lee et al. [90] employed SSAW for EVs isolation. This device was designed based on the cutoff size (d_c) determining that larger particles of this size are deflected toward the microchannel sidewalls while the particles smaller than this size remain at the center of the microchannels (Figure 1-2). The d_c can be adjusted by controlling the IDT input power and the sample flow rate leading to a modifiable size threshold in the separation. However, a lack of a parametric study in the device geometry characteristic before the chip fabrication is the main demerit of this research.

1.3 Motivation

Most of the current numerical studies only considered a 1D harmonic standing waves (HSW) modeling method to simulate the acoustic pressure distribution in the fluid numerically [6], [109], [110]. Mao et al. [111] claimed that 1D HSW modeling does not have the capability of calculating the actual acoustic pressure distribution inside the microchannel. The difference between the actual distribution and that modeled using 1D HSW is mainly caused by the longitudinal waves when SSAW is leaking into the fluid and PDMS domains. In essence, the mismatch in the acoustic

impedances between PDMS and the fluid causes the acoustic energy reflection due to the longitudinal waves. In this regard, it is highly desirable to establish an accurate representation of the acoustic pressure distribution originating from SSAW inside the microfluidic channel.

Some attempts have been made to improve the accuracy of the numerical simulation by considering 2D HSW modeling [112]. More recently, Nama et al. [113] calculated the first-order fields that drive the acoustic streaming, as well as the time-averaged acoustic radiation forces acting on suspended particles using a 2D numerical simulation. However, they simplified the system by employing the effect of the piezoelectric substrate instead of modeling it as a separate domain. This simplification adds an inevitable bias to the estimated acoustic pressure as the internal energy dissipation in the piezoelectric is ignored. Due to such a thing, the energy dissipations caused by the PDMS domain was not observed precisely as either the PDMS domain was not included in the simulation or just the impedance boundary condition was applied to the microchannel walls. In another study, Hsu et al. [114] investigated the application of dual-wavelength standing surface acoustic waves for controlling microparticles migration towards the microchannel. However, these studies were limited to the fluid domain and the influence of the PDMS walls and the influence of the piezoelectric domain were not well understood [113], [115], [116] which means the numerical modeling of acoustophoresis driven by SAW is still largely unexplored. As a result, most of the previous research focused on experimental designing and testing were solely based on trial and error processes. In essence, random device geometry characteristic values have been chosen from a wide range of data. For instance, the number of the electrode fingers and the aperture length in an interdigital transducer (IDT) are suggested to be in the range of 50 to 100 and at least 30 times the wave wavelength, respectively [95].

All of the aforementioned drawbacks of the previous studies lead to further necessary efforts for gaining an insight into the acoustophoresis-based microparticle manipulation along with optimization of the preliminary designing factors of acoustofluidic chips. By employing the optimized parameters involved in the development of the acoustofluidic chip, a highly precise and controllable manner in particle/cell manipulation and separation would be achieved. The presented results in this work would be helpful for the future design of acoustofluidic chips providing higher reproducibility and efficiency.

1.4 Objectives

There are three main objectives of this research:

1) Developing the numerical simulation for the parametric study of the effect of different operational conditions and device characteristics. In order to carry out the numerical simulation of the SSAW field, the first-order equations are used to determine the optimum values for the operational conditions and geometry. Upon calculating the optimum values, microparticle trajectories are evaluated with different sizes of the microparticles.

2) Validating the numerical simulation with the experimental tests conducted under the same conditions. This objective is achieved by comparing the percentage of the affected microparticles in the experimental tests with that obtained from the numerical simulation.

3) Employing the validated optimum values in the final design of the acoustofluidic chip. The focus of this step is to determine the separation efficiency of different sizes of the microparticles.

1.5 Organization of thesis

In the next chapter (Chapter 2), the background theory and working principle of the acoustofluidic chips are presented followed by the experimental setup Chapter where the microfabrication procedures of the proposed acoustofluidic chip and experiment details are explained (Chapter 3).

Chapter 4 and Chapter 5 are devoted to the results and discussions of two types of implemented acoustofluidic chips: parallel standing surface acoustic wave (pSSAW) and tilted standing surface acoustic wave (tSSAW), respectively. The first type is used for the microparticle manipulation while the second one focuses on the microparticle separation. In the last chapter, the thesis main achievements and results are summarized, and potential future works for the current research are presented.

Chapter 2: Background theory and working principles

2.1 Piezoelectricity background theory

There are various methods for generating ultrasonic waves such as piezoelectric [117], magnetostriction [118], electrostriction [119], electromagnetic [120], and laser-generated waves [121]. Among them, the piezoelectric-based method is widely used in the excitation of ultrasonic waves in SAW-based microfluidic devices due to its advantages mainly for its capability in generating highly repeatable complex shape and frequency content waves, and excitation of different modes of waves [122]. Additionally, the piezoelectric transduction offers large forces with small strain rates for actuation along with relatively large voltages and small currents for sensing [122].

To generate piezoelectric waves, a piezoelectric crystal without a center of symmetry (inversion center) must be used. Piezoelectric materials exhibit strong anisotropy in mechanical and electrical properties. Thus, a mechanical displacement field is generated by the surface charge density variation upon the crystal face. SAW has both longitudinal and transverse components of the mechanical displacement traveling in the vicinity of the piezoelectric material's surface. SAW can generate a wide range of frequencies within the MHz and GHz magnitude that significantly reduce the acoustic wavelength and increase the efficiency of these devices [123]. The following section provides details of promising piezoelectric materials for SAW generation.

2.2 Lithium Niobate for SAW generation

The single crystalline piezoelectric materials are formed from ions; the ions exhibit a minuscule, thermodynamically favorable misalignment that forms dipoles over each unit cell of the crystal

material. This misalignment tends to be identically oriented throughout the crystal, and so its effect accumulates for each repeated unit in the crystal as polarization, which grows to become physically significant and present in a natural state as remanent polarization (when the electrical field goes down to zero, the piezoelectric material still remained polarized) [124]. The materials most popularly used to make SAW devices include quartz, lithium tantalate ($LiTaO_3$) and lithium niobate ($LiNbO_3$). All piezoelectric materials are anisotropic, and hence the type of the waves generated from them is strongly dependent on the material orientation [125]. Due to its exceptionally high coupling coefficient and spontaneous polarization, high acoustic velocity and low-temperature coefficient of delay, and low acoustic attenuation (relative to other single crystalline piezoelectric materials used for SAW generation), lithium niobate ($LiNbO_3$) has become ubiquitous for the SAW generation [92], [126], [127].

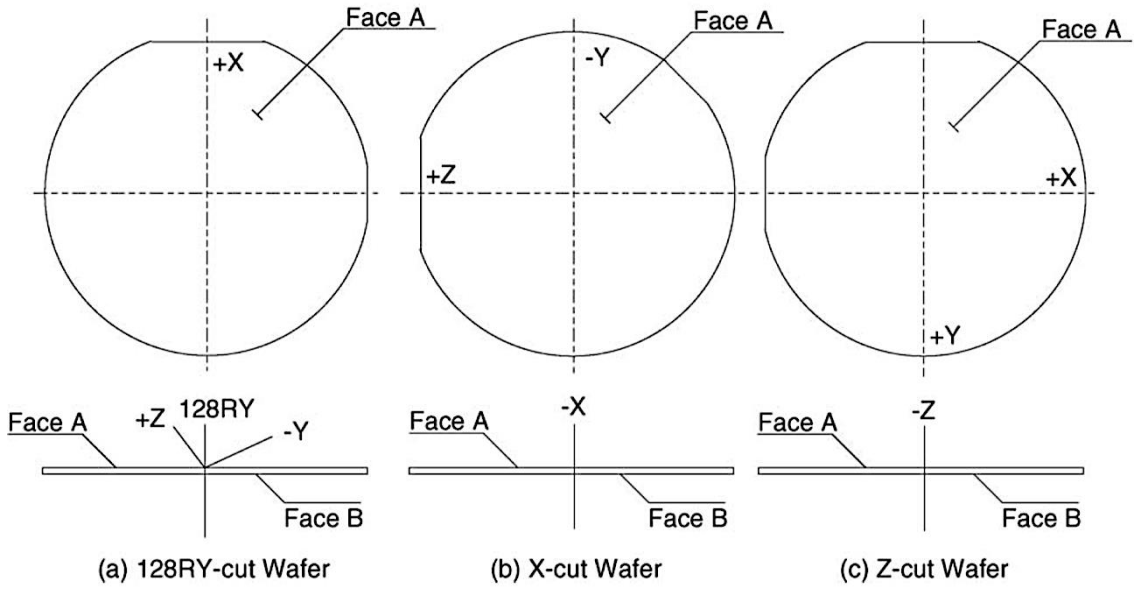

Figure 2-1. Three commons $LiNbO_3$ wafer cuts representing their origins and the wave propagation reference directions. Reproduced from [128] with permission from Materials Science and Engineering: A, Elsevier, copyright 2005.

Typically, lithium niobate wafers are obtained by growing a boule of $LiNbO_3$ from a seed crystal with the desired orientation, which is cut into wafers of the required thickness. The three

commonly processed wafers of lithium niobate are X-cut, Z-cut, and 128° Y-cut. The reference direction for 128° Y-cut wafer and Z-cut wafer is X-axis, while that for X-cut wafer is Z-axis (Figure 2-1).

In 1976, Shibayama et al. [129] determined that the 128° Y-rotated cut (Table 2-1) results in the highest electromechanical coupling coefficient (the electromechanical coupling constants defined as $K^2 = 2\Delta v/v = 2(v_f - v_m)/v_f$ where v_f is the sound wave velocity in the free substrate and v_m is the sound wave velocity measured along a short-circuited plane), and hence the lowest insertion loss (e.g. the electrical reflection and dissipation) [92]. Since then, the 128° Y-rotated X-propagating cut of $LiNbO_3$ (128° YX $LiNbO_3$) has become the most popular and widely accepted orientation for applications requiring SAW.

Table 2-1. Commonly used cuts of LiNbO3 and their corresponding electromechanical coupling coefficients and velocities. Reproduced from [92] with permission from Lab on a Chip, The Royal Society of Chemistry, copyright 2018.

Crystal Cut	***Electromechanical coupling coefficient (%)***	***Speed of sound (m/s)***
YZ	4.82	3488
ZX	0.53	3798
XZ	5.00	3483
YX	1.54	3769
120° XY	4.10	3403
20° XY	1.60	3727
128° YX	**5.30**	**3992**

The thickness of the wafers controls maximum frequency would be achieved for the SAW generation. The SAW energy is dissipated through the thickness of the wafer in four to five

wavelengths ($4\lambda_{SAW} - 5\lambda_{SAW}$) of distance from the substrate's surface. This sets a lower limit of 40 MHz for the resonance frequency to generate Rayleigh waves as most suppliers provide 0.5 mm thick wafers. Thin wafers shed energy through the backside of the substrate and affect the wave propagation and chip performance [92]. However, most studies have reported the generation of SAW at frequencies well below 40 MHz without noting or apparently being aware of this problem. In this research, we have also employed various frequencies between 20 MHz to 40 MHz and did not face energy shedding.

2.3 Interdigital transducer (IDT) geometry characteristics

To generate SAWs, an electric alternating current (AC) signal at a resonant frequency is applied to an acoustic wave production module [103] called interdigitated transducer (IDT). The IDTs are

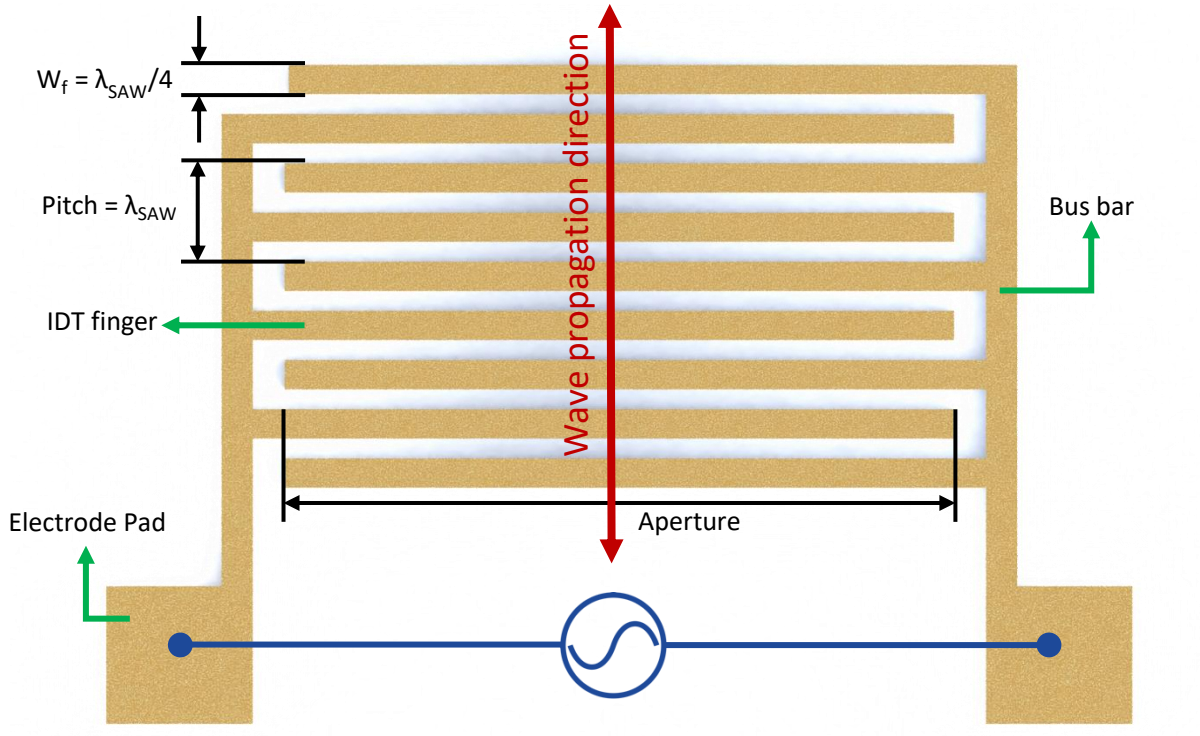

Figure 2-2. The IDT structure containing comb-shape electrode (IDT finger), and electrode pads patterned on the surface of the piezoelectric substrate. The aperture length and the pitch determine geometry characteristics of the acoustofluidic chip.

comprised of comb-shaped metal electrodes deposited on top of a piezoelectric substrate implemented converting the electrical energy to a mechanical one or vice versa [130]. The geometry parameters of IDTs need to be optimized to ensure excitation at the resonance frequency and hence increase the stability and the reproductivity of the SAWs along with the maximum energy transformation from the electrical power to the mechanical power [131]. The simplest IDT structure consists of two sets of spatially periodic straight rectangular metal bars, called fingers, which are in parallel to each other (Figure 2-2). The periodicity of the finger pairs (pitch) defines the wavelength of the resulting SAW (λ_{SAW}) such that the distance from one finger to the next is $\lambda_{SAW}/4$. In order to generate stable Rayleigh waves, the IDT pitch must be equivalent to the SAW wavelength. The speed of sound in the piezoelectric materials (c_{piezo}) depends on the material properties of the substrate and the propagation direction. Thus, the resonant frequency of a given device is determined by the choice of substrate, propagation direction, and IDT design which is expressed as:

$$f_0 = \frac{c_{Piezo}}{\lambda_{SAW}} \qquad (2.1)$$

As the structure of the IDT is symmetric, the SAWs are generated in two opposite directions perpendicular to the electrode fingers (the represented red-colored arrow in Figure 2-2).

2.4 Acoustic Radiation Force working principles

When the SAW waves reach the liquid/solid medium, they are converted to leakage waves called leaky SAW (LSAW) [132]. The propagating LSAW loses the energy (due to the viscous damping induced by the acoustic streaming flow (ASF) in the fluid) and transfers an acoustic radiation force (ARF) to microparticles [102], [103]. The microparticles motion resulting from ARF is denoted as acoustophoresis, playing a key role in on-chip microparticle manipulation [133]. SAW, which is

radiated away from the IDT, is called traveling SAW (TSAW); while standing SAW (SSAW) is formed if two oppositely propagating identical TSAWs are generated and interfere with constructively [74], [109], [134]. Both types of SAW create ARF and ASF in the fluid; however, the main interest is to minimize the effect of ASF to maximize the effect of ARF for microparticle manipulation [135]. This goal can be achieved easier by SSAW compared to TSAW, as ASF developed by oppositely propagating TSAWs cancel one another, and hence the overall power of ASF diminishes [103]. Besides, SSAW has better controllability and works with lower frequencies in comparison with TSAW (~10MHz in the case of SSAW compared to ~100 MHz for TSAW) [136].

The SSAW generates a periodic distribution of pressure nodes (minimum pressure amplitude) and anti-nodes (minimum pressure amplitude) inside the microchannel. The ARF caused by the

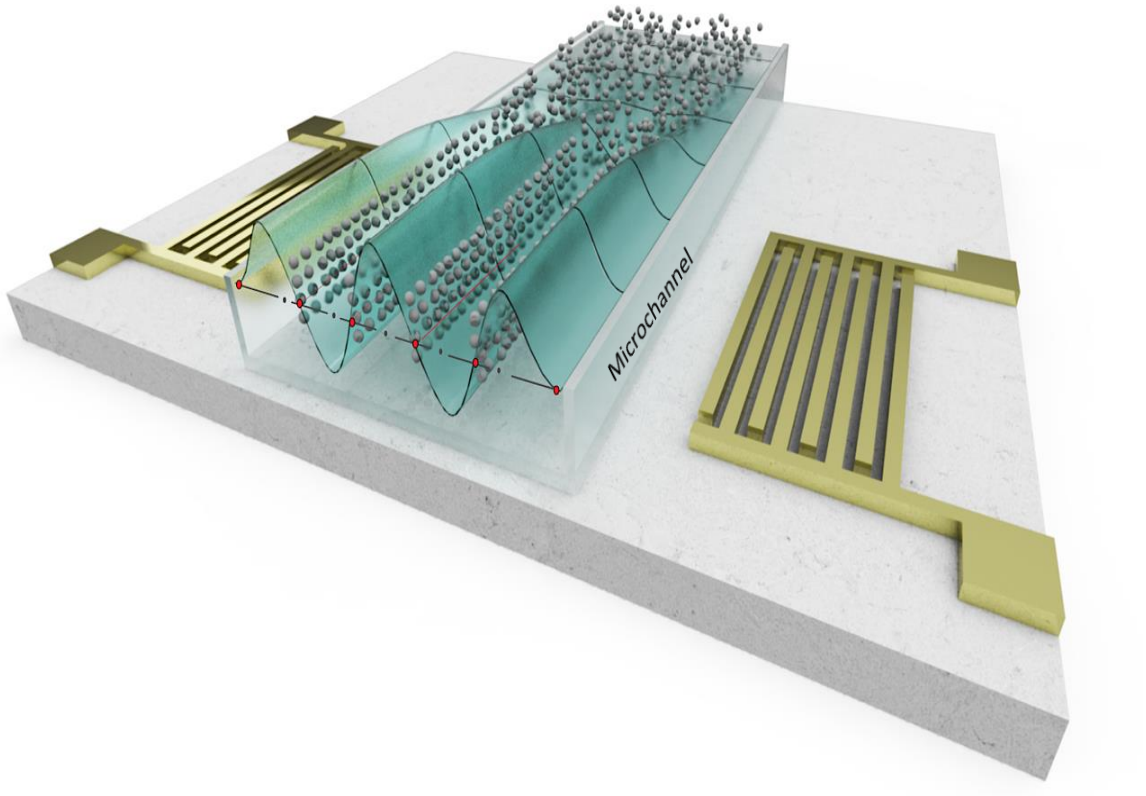

Figure 2-3. The 3D rendering of the acoustofluidic chip showing its different components.

acoustic pressure and velocity moves the microparticle/cell toward the pressure nodes (PNs) or anti-nodes (PANs) in the SSAW field based on density, compressibility, and size of microparticles and medium.

The migration of microparticles under the influence of ARF in acoustofluidic devices in a 1D harmonic standing waves (HSW) can be expressed based on two equations: 1) direct ARF and 2) indirect (Bjerknes) ARF [92]. The direct ARF equation, first developed by King [137] in 1934, only considers the microparticles as incompressible spheres. Also, the direct method can only be applied to traveling SAW (TSAW). On the other hand, the indirect ARF equations, by Yosioka and Kawasima in 1955 [138], consider the compressibility of the microparticles. The indirect ARF equations are expressed as:

$$F_{rad} = -\left(\frac{\pi P_0^2 V_p \beta_f}{2\lambda}\right) \phi(\beta, \rho)\, sin(2kx) \qquad (2.2)$$

$$\phi(\beta, \rho) = \frac{5\rho_p - 2\rho_f}{2\rho_p + \rho_f} - \frac{\beta_p}{\beta_f} \qquad (2.3)$$

where P_0, V_p, β, ρ, λ, k, and x are the acoustic pressure, the volume of the microparticle, compressibility, density, wavelength, wave number, and distance from a pressure node, respectively. The subscripts p and f represent the microparticle and the fluid, respectively. The acoustic contrast factor (ϕ) determines whether the microparticle moves toward the pressure nodes or antinodes by not only adjusting the ARF magnitude but also changing the sign of F_{rad}; the positive acoustic contrast factor ($\phi > 0$) causes the microparticles to move toward PNs while the negative acoustic contrast factor ($\phi < 0$) acts in the opposite way.

As it is indicated in Eq. (2.2), ARF is proportional to the volume of the microparticles which means that larger microparticles move toward PNs faster than smaller microparticles. Therefore, the microparticles can be separated based on their sizes gave a proper microchannel length [139]. For

similar size microparticles, the density and compressibility of the particles have been used as alternative factors for separation [140]. However, the density and compressibility of most bioparticles are in the same order, resulting in not a significant variation in the ARF magnitude.

2.5 Background theory and governing equations for numerical simulation

In order to study the effects of piezoelectricity in the $LiNbO_3$ substrate, the electrical field and mechanical motion should be coupled with each other. There are two forms of the coupling: 1) coupling the material stress and its permittivity at constant stress, 2) coupling the material strain and its permittivity at constant strain [93]. In general, the second method of coupling has been preferred due to the availability of material properties information for a stress-based constitutive relation.

In general, wave propagation in a piezoelectric crystal involves the coupling of the material atomic displacement and the electric and magnetic fields. The equation of motion must be coupled with Maxwell's equations (for electromagnetic fields) through the piezoelectric constitutive equations. The linear piezoelectric constitutive equations, consisting of Maxwell's equations, for the electric field, and the stress-strain equations, for mechanical motion, as presented below [104]:

$$\sigma = C.\epsilon - e^{tr}.E \qquad (2.4)$$

$$D = e.\epsilon + \varepsilon.E \qquad (2.5)$$

where σ is the mechanical stress vector, C is the elasticity matrix, ϵ is the strain vector, e is the piezoelectric stress matrix that couples the electric field and mechanical motion (the superscript ''tr'' represents the transpose of the matrix), E is the electric field vector, D is the electric displacement vector, and ε is the dielectric matrix.

Since the solutions of interest are the acoustic waves, the magnetic field is assumed to be static and the electric field is calculated as the negative gradient of the electric potential. Consequently, in Eqs. 2.4 and 2.5, the strain vector ϵ and electrical field E can be replaced by $\epsilon = \nabla u$ and $E = -\nabla\varphi$ and as a result:

$$\sigma = C.\nabla u + e^{tr}.\nabla\varphi \qquad (2.6)$$

$$D = e.\nabla u - \varepsilon.\nabla\varphi \qquad (2.7)$$

The material properties of $LiNbO_3$ YX 128° cut were used in this study. The proper physical properties of piezoelectric materials must be precisely defined in the numerical simulation [97]; however, this information is only available for general cuts of piezoelectric materials, and for a specific cut of interest (here, YX 128° cut $LiNbO_3$), a matrix transformation must be applied on all the tensors in order to calculate new values. In this study, a MATLAB code was developed based on the work of Ben Khelil et. al. [141] to calculate values of the transformed matrices for YX 128° cut $LiNbO_3$. The new values of each cell in the material properties matrices were calculated and provided in Table 2-2.

Table 2-2. Material properties of YX 128° cut $LiNbO_3$. Reproduced from [141] with permission.

	Elasticity matrix C [GPa]	**Piezoelectric stress matrix e [C/m^2]**	**Dielectric matrix ε [1]**
Tensor forms	$[C_{ij}] = \begin{pmatrix} C_{11} & C_{12} & C_{13} & C_{14} & 0 & 0 \\ C_{11} & C_{22} & C_{23} & C_{24} & 0 & 0 \\ C_{13} & C_{23} & C_{33} & C_{34} & 0 & 0 \\ C_{14} & C_{24} & C_{34} & C_{44} & 0 & 0 \\ 0 & 0 & 0 & 0 & C_{55} & C_{56} \\ 0 & 0 & 0 & 0 & C_{56} & C_{66} \end{pmatrix}$	$[e_{ij}] = \begin{pmatrix} 0 & 0 & 0 & 0 & e_{15} & e_{16} \\ e_{21} & e_{22} & e_{23} & e_{24} & 0 & 0 \\ e_{31} & e_{32} & e_{33} & e_{34} & 0 & 0 \end{pmatrix}$	$[\varepsilon_{ij}] = \begin{pmatrix} \varepsilon_{11} & 0 & 0 \\ 0 & \varepsilon_{22} & \varepsilon_{23} \\ 0 & \varepsilon_{23} & \varepsilon_{33} \end{pmatrix}$
Values of each element	$C_{11} = 199.5000$ $C_{12} = 68.4116$ $C_{13} = 54.5283$ $C_{14} = 08.1205$ $C_{22} = 188.0868$ $C_{23} = 84.1732$ $C_{24} = 07.8428$ $C_{33} = 213.6066$ $C_{34} = 07.3722$ $C_{44} = 75.9832$ $C_{55} = 55.8275$ $C_{56} = -04.0251$ $C_{66} = 75.7674$	$e_{15} = 4.3476$ $e_{16} = 0.3638$ $e_{21} = -1.6924$ $e_{22} = 4.4801$ $e_{23} = -1.3470$ $e_{24} = 0.2032$ $e_{31} = 1.7157$ $e_{32} = -2.4286$ $e_{33} = 2.5569$ $e_{34} = 0.7092$	$\varepsilon_{11} = 45.0530$ $\varepsilon_{22} = 37.9081$ $\varepsilon_{23} = -09.1451$ $\varepsilon_{33} = 33.3478$

The harmonic acoustic pressure field in the fluid and PDMS domains is governed by the Helmholtz wave equation [142]–[144] with the consideration of the acoustic attenuation for the PDMS walls and the effects of viscosity of the fluid, respectively. The general harmonic Helmholtz wave equation is defined as follows:

$$\nabla.\left(-\frac{1}{\bar{\rho}_k}\nabla P\right) - \frac{\omega^2}{\bar{\rho}_k \bar{c}_k^2} P = 0 \qquad (2.8)$$

where $P, \bar{\rho}_k, \bar{c}_k, \omega$ indicate the acoustic pressure, the equivalent density of the medium, equivalent sound velocity of the medium, angular frequency, respectively. The angular frequency is defined as $\omega = 2\pi f_0$.

For a linear elastic material with an attenuation (like PDMS), $\bar{\rho}_k$ and $\bar{c}_k$ are calculated as follows:

$$\begin{cases} \bar{\rho}_k = \frac{\rho_{PDMS} c_{PDMS}^2}{\bar{c}_k^2} \\ \bar{c}_k = \frac{\omega}{\left(\frac{\omega}{c_{PDMS}} - j\alpha_{PDMS}\right)} \end{cases} \quad (2.9)$$

To account for the viscous effect of the domains such as fluids, like water and phosphate-buffered saline (PBS), $\bar{\rho}_k$ and $\bar{c}_k$ are calculated based on:

$$\begin{cases} \bar{\rho}_k = \frac{\rho_{fluid} c_{fluid}^2}{\bar{c}_k^2} \\ \bar{c}_k = c_{fluid} \sqrt{1 + j\omega \frac{\left(\frac{4\mu}{3} + \mu_B\right)}{\rho_{fluid} c_{fluid}^2}} \end{cases} \quad (2.10)$$

In the above equations, ρ, c, α, μ, and μ_B denote the mass density, speed of sound, and attenuation coefficient, dynamic viscosity, and bulk viscosity in the corresponding domain of the fluid or PDMS, respectively.

To couple the acoustic fields and acoustic microparticle velocity, *P* and *v*, a simplified version of the momentum equation is used [111]:

$$v = -\frac{\nabla P}{j\omega \rho_{fluid}} \quad (2.11)$$

Coupling of the acoustic pressure in the fluid and PDMS domains and the guided SAW fields at the surface of $LiNbO_3$ is given by the continuity boundary condition along with the fluid/PDMS-$LiNbO_3$ interface. It is worth mentioning that no boundary condition is applied to the tangential direction at the fluid/PDMS-$LiNbO_3$ interface due to a negligible effect of a viscosity near the fluid viscosity boundary layer (compared to the microchannel dimensions) [114] near to the fluid viscosity boundary layer. When the SAW encounters the fluid and PDMS layers, it partially radiates into them at a Rayleigh angle which is defined as:

$$\theta_R = sin^{-1}\left(\frac{c_{fluid}\ \boldsymbol{OR}\ c_{PDMS}}{c_{piezo}}\right) \quad (2.12)$$

where c denotes the speed of sound in the corresponding domain.

The continuity boundary condition is applied as a normal component of the acceleration fields [143]:

$$n.\left(-\frac{1}{\bar{\rho}_{fluid}}\nabla P\right) = n.\left(-\frac{1}{\bar{\rho}_{PDMS}}\nabla P\right) = a_n \quad (2.13)$$

In the above equation, n and a_n are the unit normal vector and the normal component of acceleration in $LiNbO_3$, respectively.

In summary, Figure 2-4 shows the coupling procedures of different physics which should be solved simultaneously in order to calculate the acoustic pressure distribution in PDMS and the fluid. As mentioned before, the piezoelectricity law couples mechanical motion and the electrical field in

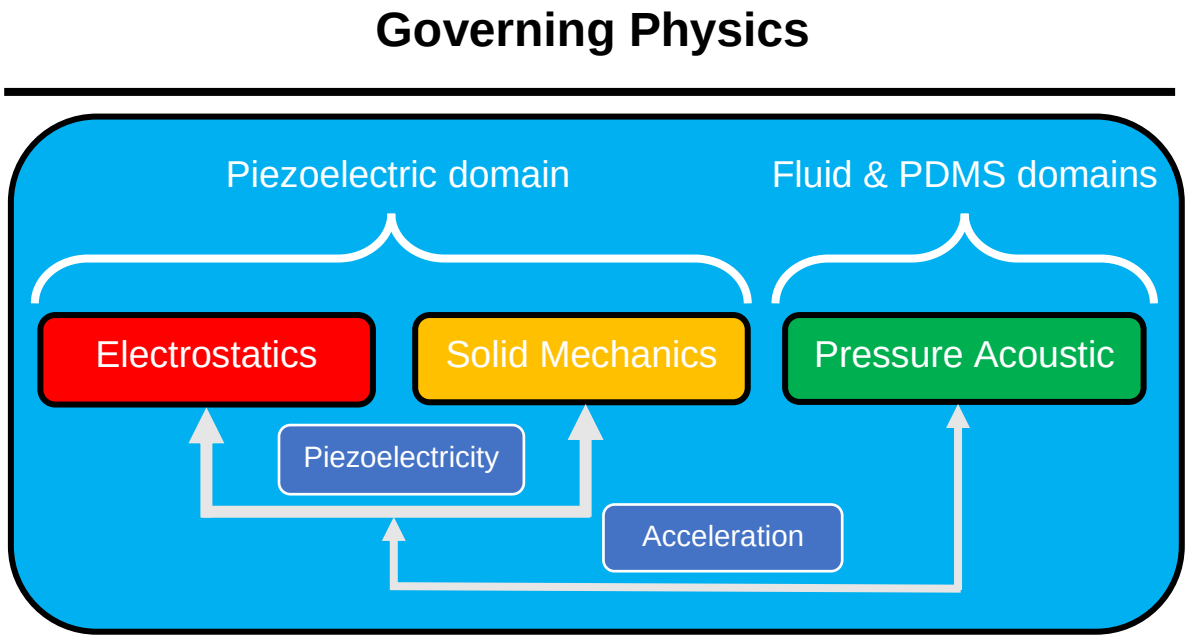

Figure 2-4. The coupling procedures of governing physics and their represented domains for numerically evaluating the acoustic pressure distribution inside the microchannel/PDMS.

the piezoelectric material. Reciprocally, the mechanical motion was coupled with the pressure acoustic in the PDMS and fluid by the acceleration fields.

One of the primary reasons for the lack of a detailed theoretical understanding of the physical processes involved in SAW devices is the difficulty in the identification of proper boundary conditions (BCs). From a numerical standpoint, the difference between BAW systems and SAW systems is limited to the differences in the actuation and wall BCs, while the governing equations remain the same [113]. There are three possibilities for BCs when dealing with sounds in the numerical simulation: 1) soft-wall BC, 2) hard-wall BC, and 3) impedance (lossy-wall) BC. The soft-wall BC, which is used when the medium interfacing with the liquid cannot sustain any appreciable pressure, is expressed as follows:

$$P = 0 \qquad (2.14)$$

The hard-wall BC applies when the liquid is interfacing with an infinitely hard wall and consequently, the normal velocity of the liquid at the wall is zero, which leads to a zero normal gradient of the pressure:

$$\boldsymbol{n}.\nabla P = 0 \qquad (2.15)$$

The lossy-wall BC is an approximate description of partial radiative acoustic losses from the liquid to the surrounding medium and can be expressed as follows:

$$\boldsymbol{n}.\nabla P = j\frac{\omega\rho_{fluid}}{\rho_{wall}c_{wall}}P \qquad (2.16)$$

The term $\rho_{wall}c_{wall}$ (the density of the wall multiply by the speed of the sound through the wall) is known as the specific acoustic impedance of the wall (here is made of PDMS) [131].

The soft-wall BC is recovered in the limit of zero impedance of the surrounding medium, while the hard-wall BC corresponds to infinitely large impedance. The hard-wall BC can be used for

BAW systems using typically silicon or glass walls, however, it is an inaccurate condition for SAW systems using PDMS walls [111], [113]. Another way to account for the influence of the PDMS walls is to consider the PDMS walls as a separate solid domain and solving Helmholtz equations [145] for both fluid and PDMS domains simultaneously.

In general, there are four forces acting on suspended microparticles inside the microchannel and in order to calculate microparticle trajectories they should be determined: 1) the acoustic radiation force (ARF), 2) the drag force, 3) the gravity force and 4) the buoyancy force. Since the gravity and buoyancy forces have the same magnitudes but applied in opposite directions [74], they are canceled out and were not implemented in the numerical study here. Upon obtaining the acoustic fields (P) inside the microchannel, the time-averaged radiation force potential (U) is calculated based on [146]:

$$U = V_P \left\{ f_1 \frac{1}{4\rho_{fluid} c_{fluid}^2} \boldsymbol{Real}(P \cdot P^*) - f_2 \frac{3\rho_{fluid}}{8} \boldsymbol{Real}(v \cdot v^*) \right\} \quad (2.17)$$

where V_P is the microparticle volume; $\rho_{particle}$ and ρ_{fluid} are the density of the microparticle and the fluid, respectively, $c_{particle}$ and c_{fluid} are the speed of the sound in the microparticle and the fluid, respectively. The Real notation indicates the real part of a complex number, and the asterisk (*) denotes complex conjugation. f_1 and f_2 are monopole and dipole coefficient defined as [146]:

$$f_1 = 1 - \frac{\rho_{fluid} c_{fluid}^2}{\rho_{particle} c_{particle}^2} \quad (2.18)$$

$$f_2 = \frac{2(\rho_{particle} - \rho_{fluid})}{(2\rho_{particle} + \rho_{fluid})} \quad (2.19)$$

Microparticles exposed to the standing field are subjected to a time-averaged ARF if the gradient of a radiation force potential is determined by adopting the theory of Gor'kov [147]:

$$F_{rad} = -\nabla U \quad (2.20)$$

where F_{rad} and ∇U are the ARF and gradient of the time-averaged radiation force potential. The drag force mainly causes by the relative velocity of microparticles to that of the fluid which is suspended in and due to induced acoustic streaming flow (ASF). The drag force is given by Stokes' law [143]:

$$F_{Drag} = 3\pi\mu d_P(\langle v\rangle - v_P) \quad (2.21)$$

Where μ is the fluid dynamic viscosity, d_P is microparticle diameter, $\langle v\rangle$ is the acoustic streaming flow velocity which is the time-averaged over the full acoustic time period, v_P is the microparticle velocity.

The motion of microparticles is governed by Newton's second law (constant mass) which is given as:

$$m_P \frac{dv_P}{dt} = F_{rad} + F_{Drag} \quad (2.22)$$

which can be simplified as [148]:

$$\frac{4\pi}{3}\left(\frac{d_P}{2}\right)^3 \rho_P \frac{dv_P}{dt} = F_{rad} + 6\pi\mu d_P(\langle v\rangle - v_P) \quad (2.23)$$

In the above equations: m_P is the mass of microparticle, ρ_P is the density of microparticle.

By solving Eq. (2.23) in the Spatio-temporal manner, v_P is derived which is then used to evaluate the microparticle trajectories.

It is worth mentioning that in both numerical and experimental setups, we used DI water as the fluid and hence fluid subscript is replaced with water from now on. The values for all the relevant properties of the DI water, as well as the typical operational parameters used in our numerical model, are listed in Table 2-3.

Table 2-3. Material properties of DI water, PDMS, and PS microparticles at a temperature of $T = 25$ ℃. Reproduced from [113] with permission.

	Parameter name	***Symbol***	***Value and Unit***
DI Water	Mass Density	ρ_{water}	997 $[kg/m^3]$
	Speed of Sound	c_{water}	1497 $[m/s]$
	Shear Viscosity	μ	0.899 $[mPa.s]$
	Bulk Viscosity	μ_B	2.47 $[mPa.s]$
PDMS	Mass Density	ρ_{PDMS}	920 kg/m^3
	Speed of Sound	c_{PDMS}	1076.5 m/s
	Attenuation Coefficient @ 6.65 MHz	α_{PDMS}	31 dB/cm
PS Microparticles	Mass Density	$\rho_{Particle}$	1060 kg/m^3
	Speed of Sound	$c_{Particle}$	2050 m/s

Chapter 3: Microfabrication procedures of Acoustofluidic chip and experimental setup details

3.1 Photolithography

Photolithography uses ultraviolet (UV) light as a patterning tool for transferring structures from a photomask to the photoresist-coated substrate. The photolithography technique has various steps:

1) The photomask is made from a transparent plastic (called miler photomask) with the designed structures printed on it. There are two types of a photomask (depending on the application): dark field and bright field used for negative and positive photoresists, respectively. The structures of this study were designed using the commercial software AutoCAD (Version 2019, Autodesk Inc.).

2) A microlayer of the photoresist is coated on the top surface of the substrate ($LiNbO_3$ YX 128° wafer) at a specific rotational speed for a certain amount of time.

3) The photoresist-coated substrate is heated up on a hot plate to evaporate unnecessary photoresist solvents.

4) Using a mask aligner device, the photomask is placed on top of the substrate and exposed to the UV light (with a specific wavelength and intensity) for a certain period of time (should be optimized for each type of the photoresist).

5) The UV light causes a photochemical reaction in the photoresists. For a positive photoresist, the exposed area is soluble to photoresist developers. In contrast, the exposed area is insoluble to the photoresist developer for a negative photoresist.

3.2 Designed masks for photolithography step

As can be seen from Table 3-1, there are three generations of designs of IDT pairs and microchannels. Both IDTs and microchannels were modified to increase the functionality of the acoustofluidic chip. For this purpose, four pads were replaced with two pads to reduce the complexity of the device and make it more ease of use. In the final design (third design), various feature sizes on a single $LiNbO_3$ wafer are implemented to minimize the material waste and make the fabrication more cost-effective.

Table 3-1. A different generation of the mask designed for the IDTs and the microchannels.

	First-generation design	**Second-generation design**	**Third-generation design**
IDTs	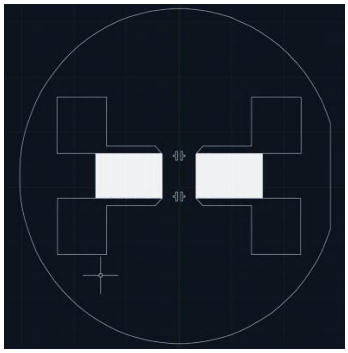	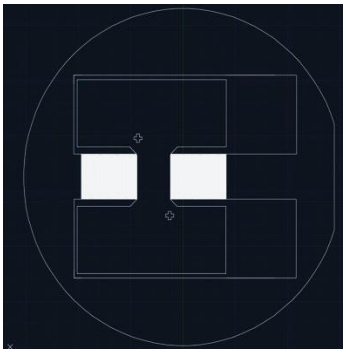	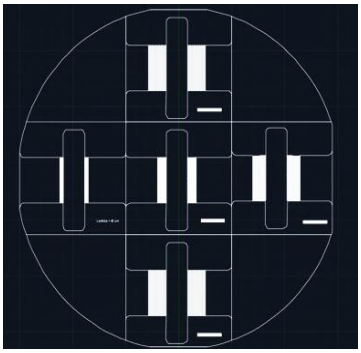
Microchannels	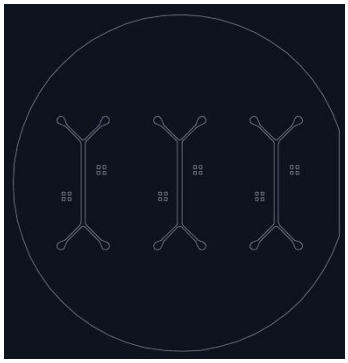	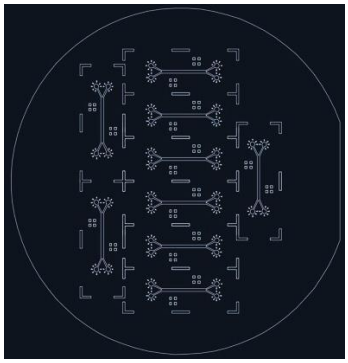	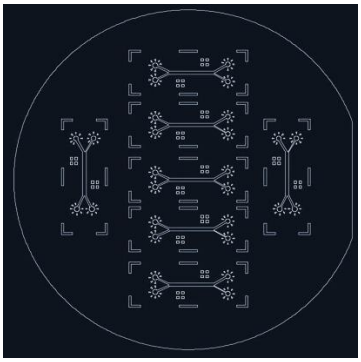

3.3 Microfabrication of interdigital transducer (IDT)

The standard photolithography processes were used to fabricate the IDT fingers. Inert and noble properties of gold (Au) such as resistant to oxidation, high conductivity, and stability in nature, have made it a promising metal for electrodes patterning. However, Au does not adhere well to the substrates due to its inability to form stable metal-oxide interfaces. Common oxide-forming metals such as titanium (Ti), aluminum (Al), chromium (Cr) can create these oxide interfaces. Due to the availability of Au and Cr metals in our cleanroom facility, the bilayers of Au/Cr were employed to fabricate the IDT fingers. The microfabrication sequence shown in Figure 3-1 was followed. First, a metal double layer (Cr 35 Å /Au 100 Å) was subsequently deposited to the surface of the $LiNbO_3$ wafer with a sputtering machine (Angstrom Engineering Inc.). Then, a layer of S1805 photoresist (MicroChem Corp.) was spin-coated onto the substrate, followed by soft bake and UV exposure through a lithographic mask using the mask aligner (Model 200, OAI). Next, a wet etching process was applied in the following order: (i) the unwanted photoresist was removed using MF-CD26 developing solution (MicroChem Corp.); (ii) the wafer was rinsed with gold and chromium etchants to remove unwanted deposited metal layers from the $LiNbO_3$ wafer; and (iii) the MF-319 photoresist stripper was used to remove the remaining photoresist.

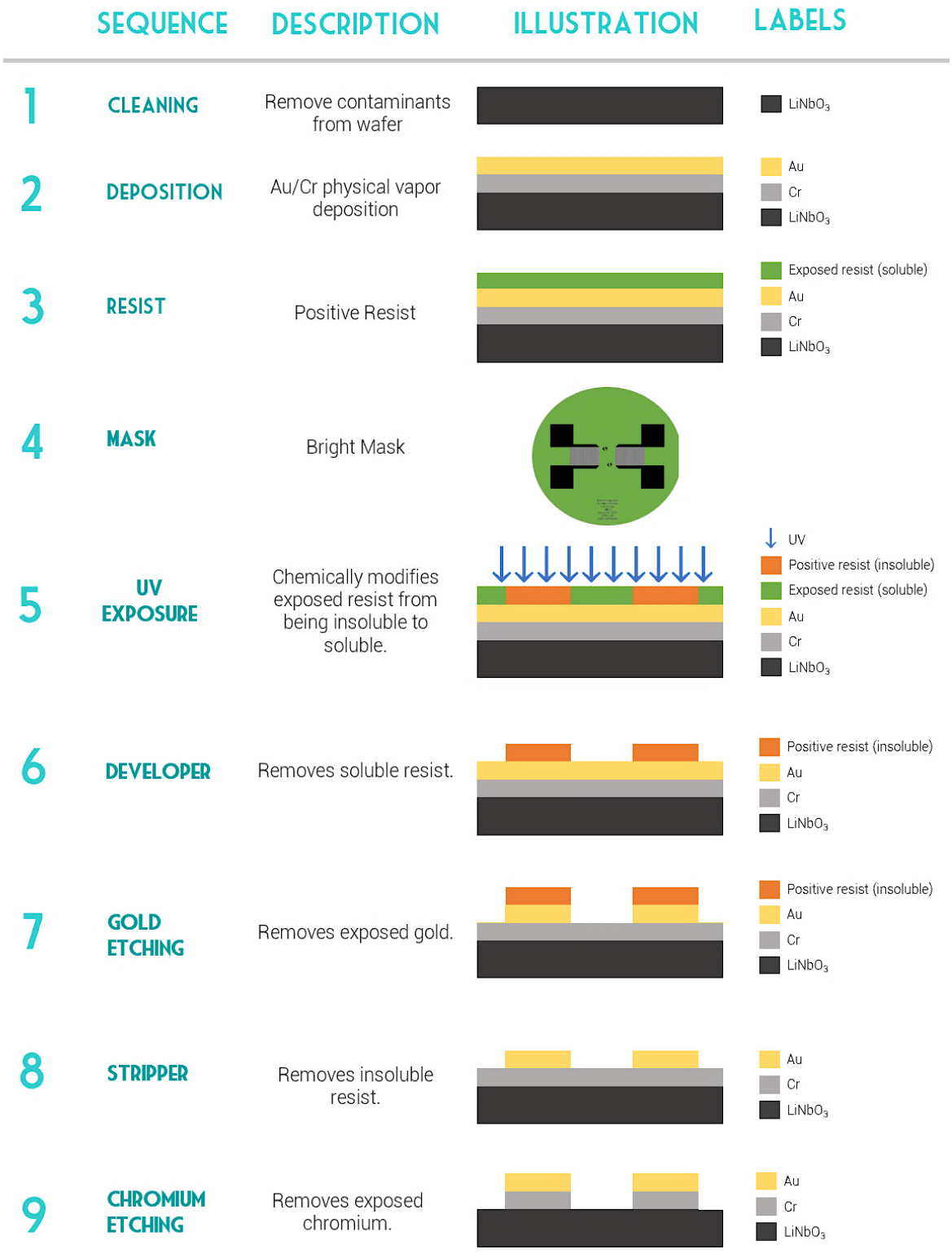

Figure 3-1. The procedures should be followed sequentially for the SSAW-device fabrication using wet etching protocols.

3.4 Microfabrication of microchannel

The biocompatible and optically transparent PDMS microchannels were fabricated based on the standard soft lithography technique using a negative photoresist SU8 (MicroChem Corp.). First, the SU8 photoresist was spun onto the silicon wafer at 3000 rpm for 45 seconds. Then, the photoresist coated wafer was soft baked for 5 min at 65 °C followed by 20 min at 95 °C. The wafer was then patterned with a UV light source with an exposure dose of 140 mJ/cm^2 followed by post-exposure baking for 5 min at 65 °C and 10 min at 95 °C. In the next step, the wafer was rinsed with SU-8 developer (MicroChem Corp.) for 15 min and then washed with isopropyl alcohol (IPA). In the last step, the fabricated SU-8 mold was hard-baked for 15 min at 150 °C. The Sylgard 184 Silicone Elastomer Curing Agent and Base (Dow Corning) were mixed at a 1:10 weight ratio, and then cast on top of the SU8 mold and cured at 75 °C overnight. A biopsy punch was used to drill holes in the PDMS channel to form inlets and outlets.

3.5 Acoustofluidic chip assembly

The PDMS microchannel and the LiNbO3 substrate were placed in an oxygen plasma device to bond them together (PE-50 series, Plasma Etch Inc.). The conditions that were used for activating both surfaces are 30 seconds at 40 sccm oxygen flow rate, 170 mTorr chamber pressure, and 40 W power.

3.6 Experimental system setup details

A syringe pump (78-8088C, Cole-Parmer Instrument Company LLC.) was used to push the samples containing the microparticles into the microfluidic channel at the fixed flow rate of 5 $\mu L/min$. To prepare the sample for the injection, 5.0% *w/w* color dyed polystyrene (PS) microparticles (Phosphorex Inc.) with a concentration of 10 mg/ml, the density of $\rho =$

1060 kg/m^3 and the compressibility of $\beta = 246\,TPa^{-1}$ were diluted in 1 mL aqueous solution including 0.1% *w/w* Tween-20 and 1.0% *w/w* Glycerol (mixture physical properties are $\rho = 1005\ kg/m^3$ and $\beta = 458\,TPa^{-1}$) for decreasing the adhesion of PS microparticles to the microchannel walls and $LiNbO_3$ surface. The various colors and sizes of PS microparticles used include Red 20 μm, Blue 15 μm, Red 10 μm, and Blue 5 μm.

The proposed acoustofluidic chip was mounted on the stages of an upright microscope (Z16APO, Leica Microsystems GmbH) equipped with a DFC340FX camera and an inverted microscope (REVOLVE 4, ECHO) which was equipped with an iPad Pro's camera (Apple Inc.) for capturing pictures and recording videos. An RF signal generator (81110A, Agilent Technologies Inc.) and an amplifier (325LA, Electronics & Innovation Ltd) with the capability of providing different frequencies and voltage amplitudes were used for applying RF signals to the IDTs (see Figure 3-2).

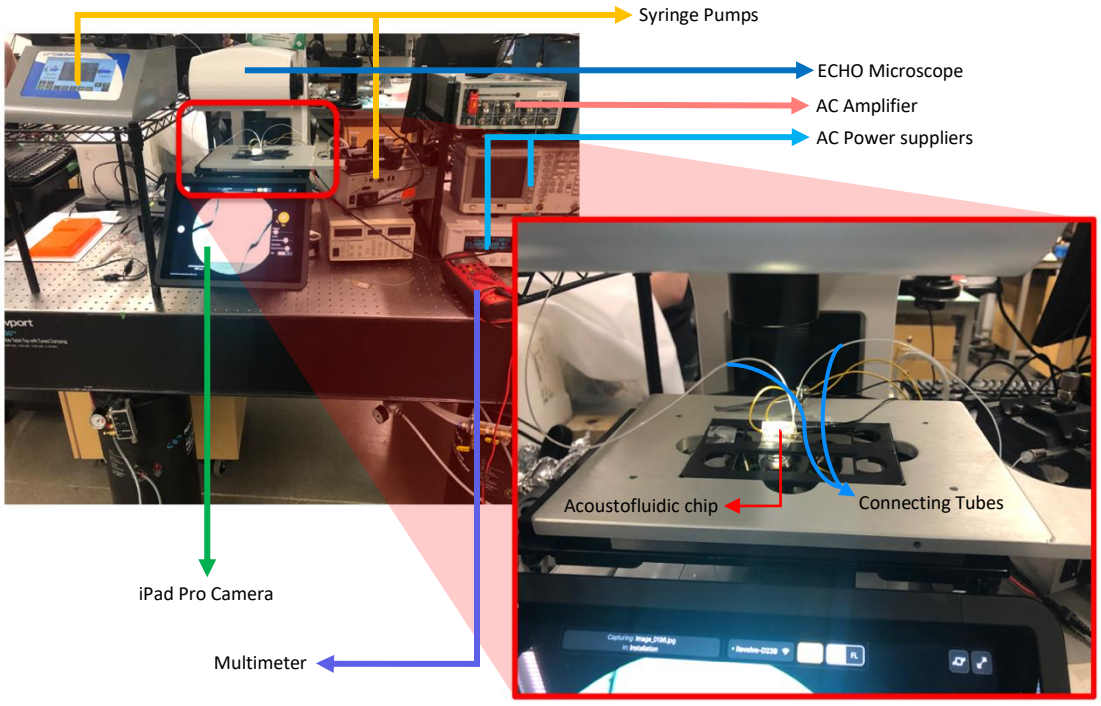

Figure 3-2. The experimental setup

To find the resonant frequency of the fabricated IDTs upon a surface of $LiNbO_3$ wafer one pair of IDTs was applied to RF signal to generate a TSAW while another IDT pair was connected to an oscilloscope. The best resonant frequency of the fabricated IDTs was found to be $f_0 = 39.63\ MHz$ at the wavelength of $\lambda_{SAW} = 100\ \mu m$ which is in agreement with our proposed numerical simulation (see Section 4.1.2).

The microfabricated IDT pairs along with their electrode pads are shown in Figure 3-3. There are five different designs on a 3-inch $LiNbO_3$ wafer (Figure 3-3, A). Next, the wafer was diced by a diamond cutter into small pieces ((Figure 3-3, B) where each of them containing IDT fingers and the electrode pads.

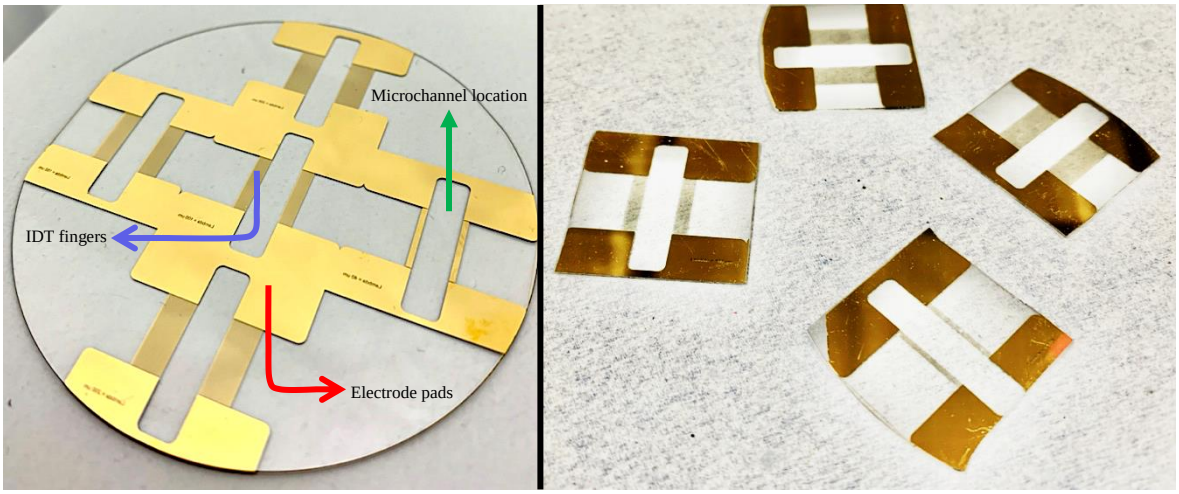

Figure 3-3. (A) The paternned IDT fingers on the 3-inch $LiNbO_3$, (B) The diced $LiNbO_3$ which is done by the diomond cutter.

Chapter 4: Precise microparticle manipulation with parallel Standing Surface Acoustic Wave

In order to manipulate cells/microparticles in a highly precise, controllable manner, the distribution of PNs or PANs inside the microchannel is needed to be well predicted. Additionally, the structure of the IDTs determines the bandwidth and direction of the generated SSAW. By changing the number, spacing, and aperture of the IDT fingers, one can change the characteristics of the resulting SSAW. As a result, a complete investigation of the influence of these key parameters in an acoustofluidic chip using a comprehensive numerical model is crucial prior to the fabrication of the device. The developed numerical model must be able to simulate the piezoelectricity effect in the $LiNbO_3$ substrate and the SSAW field in both fluid and PDMS domains.

In this research, the numerical simulation is developed and validated to conduct a parametric investigation of the device geometry characteristic and external parameters and to find the optimum conditions for subsequent chip fabrication and operation. Sequentially, the acoustic radiation force acting on suspended microparticles was calculated from the derived acoustic pressure in the fluid, based on which the trajectories of individual microparticles can be predicted to evaluate the acoustophoresis response to SAW excitation. In the last step, the simulated SSAW-induced acoustophoresis results are compared to the experimental test outcomes conducted with fabricated SSAW-based microfluidic devices.

4.1 Numerical simulation results and discussion

The commercialized finite element analysis (FEA) software package (COMSOL Multiphysics®, version 5.4) was used to simulate the SAW propagation and penetration in the $LiNbO_3$ substrate,

PDMS, and the fluid-filled microchannel. The SAW field is derived by solving Eqs. 2.6, 2.7, and 2.8 using both time-dependent and frequency-based solvers. The modules called “Electrostatics” and “Solid Mechanics” were used to simulate SAW generation and propagation in $LiNbO_3$, and the “Pressure Acoustics” module was used to numerically solve acoustic pressure (AP) distribution in the fluid and PDMS.

Upon evaluation of AP in the fluid domain, the “Microparticle Tracing” module was carried out to simulate microparticle deflection caused by the pressure nodes and anti-nodes. Since the SSAW field is uniform in the longitudinal direction of the channel, a two-dimensional (2D) modeling of the device cross-section is considered. In the computational domain, a fluid domain is sealed between the bottom $LiNbO_3$ substrate and the top PDMS domain (Figure 4-1). The IDTs patterned on the piezoelectric substrate are located symmetrically with respect to the channel center. The list of studied parameters along with their values is given in Table 4-1.

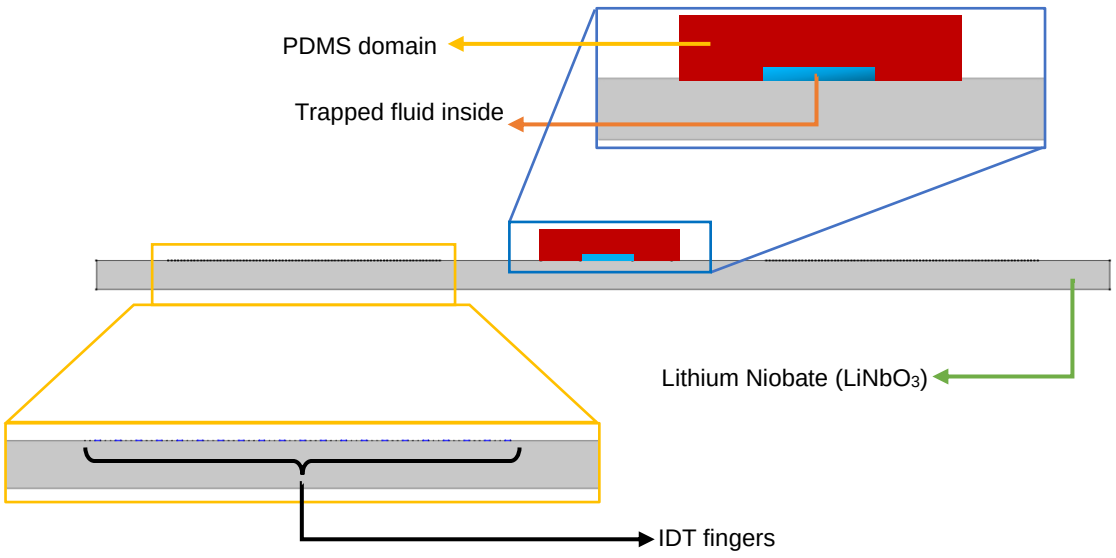

Figure 4-1. The computational domain used for the numerical simulation. The domain includes the piezoelectric substrate, PDMS, and fluid domains.

Table 4-1. Microfluidic device geometrical parameters implemented in the FEA simulation

	Parameter	***Symbol***	***Value***
IDT	Pitch = Lambda [μm]	$p = \lambda$	$\begin{cases}100\\150\\200\end{cases}$
	Width of fingers [μm]	$d = \lambda/4$	$\begin{cases}25\\37.5\\50\end{cases}$
	Aperture length [mm]	A	10
	Number of IDT fingers	N	$\begin{cases}10\\20\\30\\40\\50\\60\\70\\80\\90\\100\end{cases}$
Microchannel	Microchannel width [μm]	$W_{Channel}$	$\begin{cases}75\\150\\300\\800\end{cases}$
	Microchannel height [μm]	$H_{Channel}$	$\begin{cases}20\\40\\60\\80\\100\end{cases}$
PDMS	PDMS width [mm]	W_{PDMS}	$\begin{cases}1.0\\2.0\\5.0\end{cases}$
	PDMS height [mm]	H_{PDMS}	$\begin{cases}1.0\\3.0\\5.0\end{cases}$

4.1.1. Mesh independency analysis

In order to save computational resources and time, the mesh size is decreased at the piezoelectric substrate and progressively increased closer to the bottom of the substrate (as most of the relevant

physics is close to the top surface). The maximum magnitude of the AP is used as a parameter for mesh independency analysis (by solving a series of meshes with different maximum mesh element sizes). Results indicated that a coarse mesh size of $\frac{1}{5}\lambda_{SAW}$ near the bottom of the piezoelectric substrate and a fine mesh with the size of $\frac{1}{10}\lambda_{SAW}$ in the PDMS domain, the microfluidic microchannel as well as near the top of the piezoelectric substrate can provide acceptable accuracy and mesh-independency for the numerical results.

4.1.2. The resonance frequency of piezoelectric material

The first and foremost step after the mesh-independency evaluation is to identify the frequency at which maximum vibration occurs (referred to as the resonance frequency (f_0) occurring when the natural frequency of the proposed chip matches the RF signal frequency). The resonance frequency depends on the piezoelectric material and its orientation cut which determines the speed of sound. In order to find the resonance frequency, the variation of the averaged maximum value of the acoustic pressure (*AP*) inside the microchannel and the PDMS domain versus frequencies is studied. As most studies indicated the speed of sound of $LiNbO_3$ (YX 128° cut) to be around $\sim 3900\ m/s$, the initial value of f_0 was estimated as 39 MHz for $\lambda_{SAW} = 100\ \mu m$. Next, the RF signal frequency was changed by an increment of $\pm 0.01\ MHz$ in order to find the peak value of AP. This approach was carried out for $\lambda_{SAW} = \{150\ \mu m, 200\ \mu m\}$ to increase the accuracy. As can be seen from Table 4-2, the resonance frequency only occurs at a natural frequency which AP shows a peak value (P_0). To calculate the resonance frequency at each wavelength, the frequency at which P_0 happens was evaluated and then divided by the corresponding wavelength. As a result, the speed of the sound of $LiNbO_3$ was derived. It is worth mentioning that the efficiency of a SAW device is commonly linked to its quality factor defined as $Q = f_0/\Delta f$, where the width of the

resonant peak in the frequency space is measured at one-half of the peak's highest amplitude [149]. The quality factor is influenced by the dielectric losses of the piezoelectric materials, loading effects, ohmic losses, and acoustic leakage to the substrate [92]. The calculations for both the speed of the sound in lithium niobate (c_{LN}) and Q are listed along with each wavelength in Table 4-2. Q was calculated based on the aforementioned definition: for this purpose, P_0 and f_0 were identified followed by measuring two frequencies (f_1 and f_2) at the corresponding amplitude of $P_0/2$. As observed from figures in Table 4-2, by decreasing λ_{SAW}, the P_0 amplitude increases which is in agreement with Eq. (2.8). Also, Q has an upward trend as f_0 increases which promote the maximum power transmission. However, narrower bandwidths happen at higher values of Q; this causes a problem by deviating from f_0 (as compared to the case of lower Q). Furthermore, results indicate that the average value of c_{Piezo} is around $3853\ m/s$ (which is less than our initial guess by $150\ m/s$). This value of the speed of sound was used for next steps. Additionally, half of the bandwidth (*B/2*) of the IDT is shown for each wavelength in Table 4-2. Results indicate that by increasing the wavelength, *B/2* decreases proportionally. As an example, *B/2* changes from 2.25 to 1.01 by increasing λ_{SAW} from $100\ \mu m$ to $200\ \mu m$. The higher f_0 (lower λ_{SAW}) leads to a narrower *B* which is result in harder controllability of the experimental tests as a small shift from f_0 would cause a substantial reduction in the energy transmission to the microchannel (here *AP*) compared to the wider *B.*

Table 4-2. Resonance frequency of each wavelength by changing the frequency of the RF signals

Implemented parameters along with their values		Applied RF signal voltage = 20 [V] Number of IDT fingers = 21	Microchannel height = 100 [μm] Microchannel width = 800 [μm]
Wavelength (λ_{SAW})	Calculated Sound Speed	**The variation of the averaged maximum value of Acoustic Pressure (AP) in the fluid versus the RF signal frequency**	
$\lambda_{SAW} = 100\ [\mu m]$	$c_{LN} = 3{,}836\ m/s$	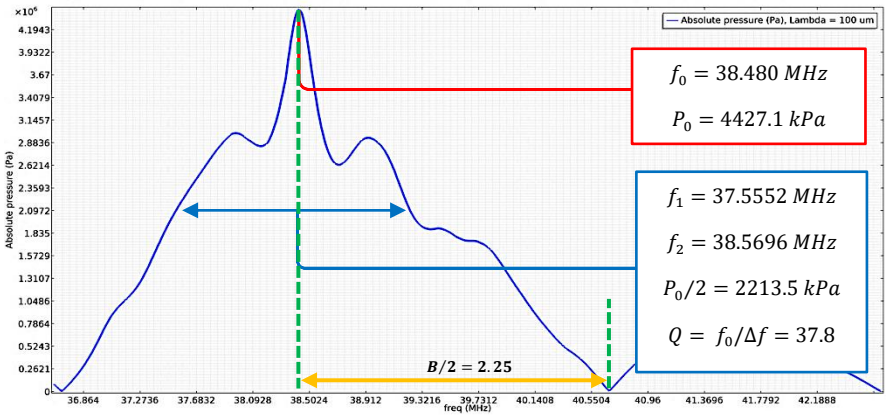	
$\lambda_{SAW} = 150\ [\mu m]$	$c_{LN} = 3{,}858\ m/s$	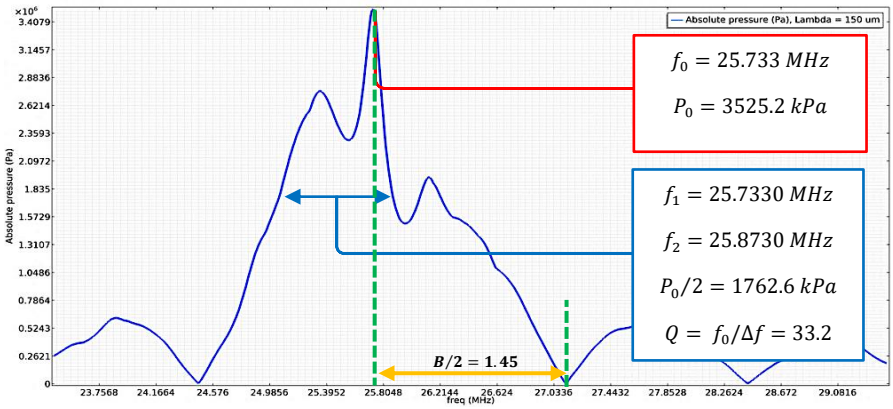	
$\lambda_{SAW} = 200\ [\mu m]$	$c_{LN} = 3{,}864\ m/s$	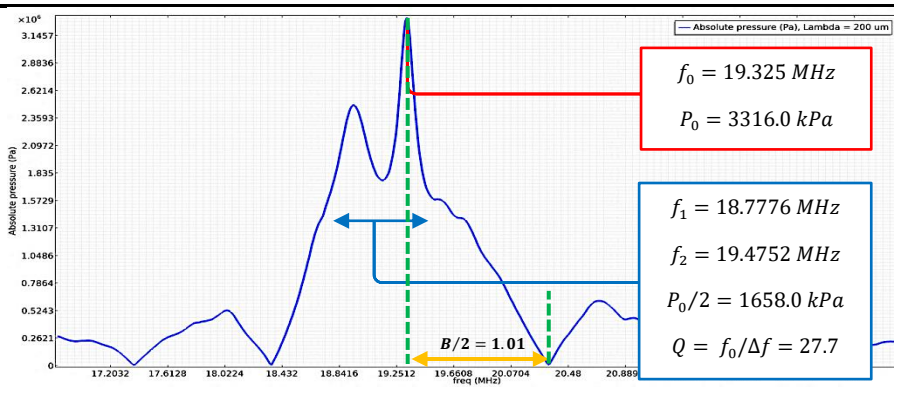	

4.1.3. PDMS wall boundary condition

In order to find the appropriate wall boundary condition (BC), hard and lossy (impedance) boundary PDMS walls were considered as separate domains with the same device characteristic (to eliminate bias for the numerical simulation). The results in Table 4-3 demonstrate that the hard-wall BC changes the locations of PNs and PANs while the lossy-wall BC increases the maximum value of the acoustic pressure (~ 68% higher). However, there is a third option, i.e., considering the PDMS walls as the separate domain and including the thickness of the walls which results in the dissipation of the majority of the acoustic energy into PDMS before reaching the fluid. This option is more realistic and the results obtained using this option are in better agreement with previous studies [111], [113], [144]. Considering this option results in the maximum value of the acoustic pressure lower than that obtained for the case of the lossy-wall BC and still higher than that obtained for the hard-wall BC. Nevertheless, using either assumption of the lossy wall or PDMS does not disrupt the morphology of PNs and PANs, indicating these methods to be good candidates for simulations. In this study, due to the advantages of the PDMS as a separate domain in comparison to other types of BCs, we have chosen it for further steps in our simulation.

Table 4-3. The comparison of wall BC effects on the amplitude and the morphology of acoustic pressure distribution and the normal acceleration

Parameter values	Applied RF signal voltage = 20 [V] Number of IDT fingers = 21 Lambda = 150 [μm]	Microchannel height = 100 [μm] Microchannel width = 800 [μm] PDMS width = 3 [mm] PDMS height = 1 [mm]
PDMS wall BC	**Acoustic pressure distribution [Pa] inside the microchannel and the PDMS walls** **The normal component of the acceleration [m/s^2]**	
Hard-wall BC	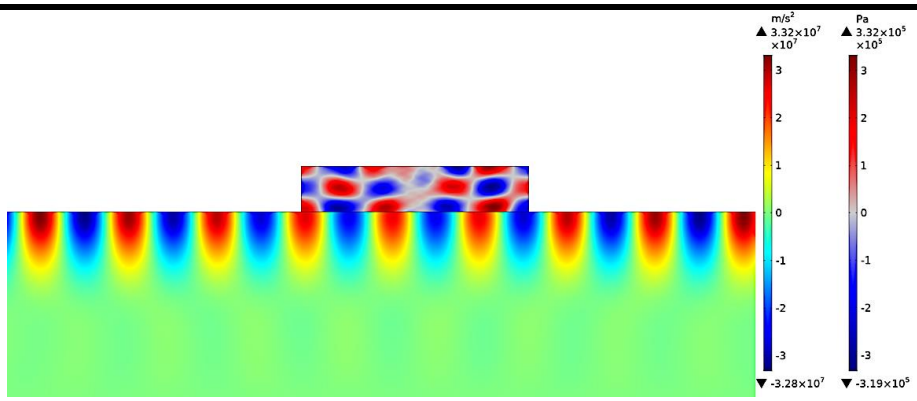	
Lossy-wall (Impedance) BC	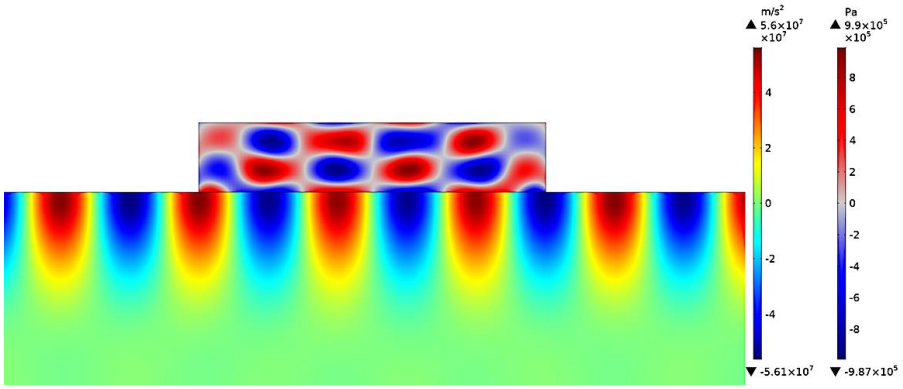	
PDMS as the separated acoustic propagation domain	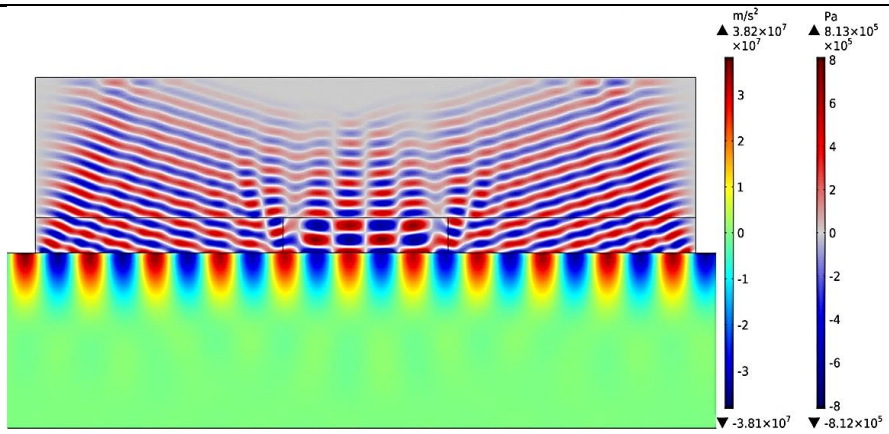	

4.1.4. Effects of width and height of the microchannel

In acoustofluidic, one of the most important parameters is the dimension of the microchannel. Previous studies [111], [113], [144] have shown that a small mismatch in the alignment of the microchannel in the bonding process can disrupt the positioning of the PNs and PANs in the designed acoustofluidic chip. Most of the research has assumed the width of the microchannel as the definitive factor for the locations of PNs and PANs. For instance, to have one PN in the microchannel, the width of the microchannel must be equal to $\lambda_{SAW}/2$, while the width should be λ_{SAW} for two PNs. Despite their efforts, none of the current studies have considered the microchannel's height as a parameter to be optimized. Herein, we carried out the parametric study to calculate the distribution of AP at various heights and widths of the microchannel. It is worth mentioning that the microchannel was shifted by $\lambda_{SAW}/4$ from the center of the delay line in order to locate one PN in the middle of the microchannel.

In general, the maximum amplitude of AP presents in PANs, where the mechanical displacement is maximized, while the location of PNs is determined where the minimum mechanical displacement occurs. Table 4-4 demonstrates the effects of the width and height of the microchannel on the locations of the PNs and PANs. Each figure in Table 4-4 demonstrates the contour showing positive values (red color) and negative values (blue color), called dipole AP, along with zero values (white color) of AP at different heights and widths of the microchannel. In all of these figures, the value of the AP was normalized. Results indicate that the height of $20\ \mu m$ provides only a vertical PN (yellow dashed lines); while larger heights promote one and three horizontal PNs at heights of $60\ \mu m$ and $100\ \mu m$, respectively. Additionally, the increase in the height induces multiple AP dipoles (across the height of the microchannel) which location of them is mirrored with respect to the previous AP dipole. While the width of the microchannel is half of

the wavelength, only one vertical PN occurs in the middle of the microchannel compared to three vertical PNs (i.e., one in the middle and two at sidewalls) when the width of the microchannel is the same as the wavelength. It is worth mentioning that the location of the horizontal PNs changes over time ($T = 1/f_0$); the horizontal PNs along with AP dipoles move to the top of the microchannel until their energy dissipates to PDMS.

Table 4-4. The distribution of the pressure nodes (PNs) and pressure anti-nodes (PANs) at different widths and heights of the microchannel

Parameter values	Applied RF signal voltage = 20 [V] Number of IDT fingers = 21 Lambda = 150 [μm]	PDMS width = 3 [mm] PDMS height = 1 [mm]

Microchannel width	75 [μm]	150 [μm]
Height of the microchannel 20 [μm]	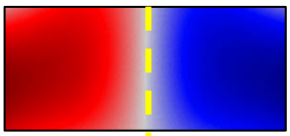	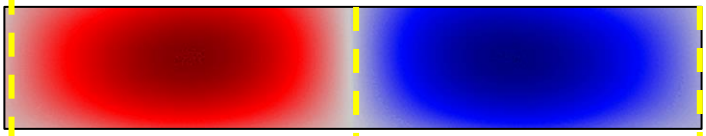
60 [μm]	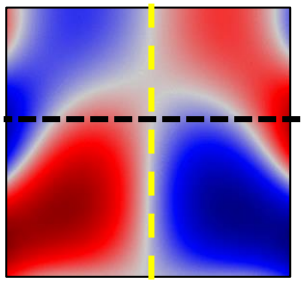	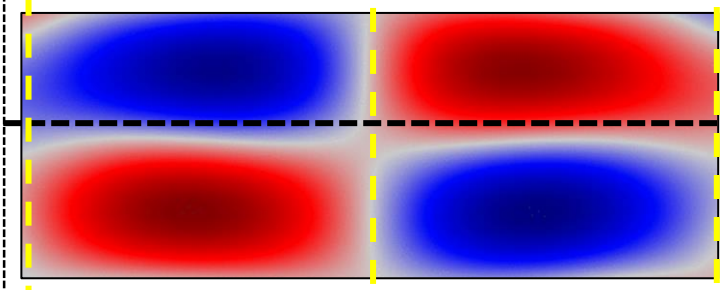
100 [μm]	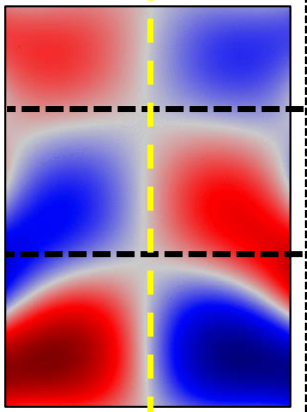	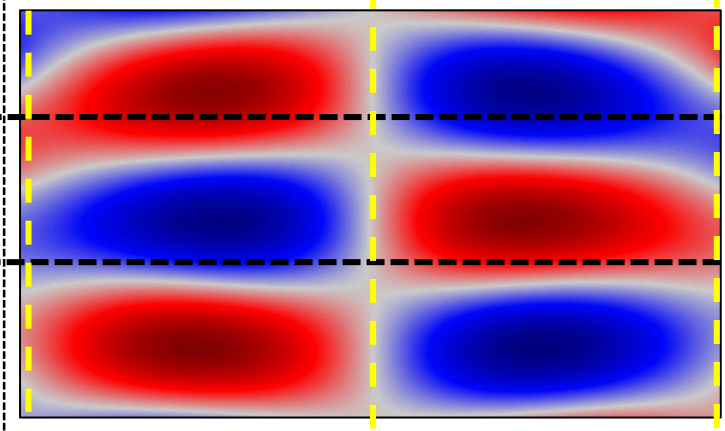

4.1.5. Effects of width and height of PDMS walls

As previously mentioned, sound waves propagate into the PDMS domain before reaching the middle-trapped fluid, dissipating most of the acoustic energy into the PDMS domain. Consequently, influences of the width (W_{PDMS}) and the height (H_{PDMS}) of the PDMS domain must be investigated prior to fabrication to minimize the energy dissipation in the final proposed acoustofluidic device. In essence, W_{PDMS} and H_{PDMS} of the PDMS domain should be studied for their influences on the distribution and the amplitude of Y (normal) component of the displacement and hence the acoustic pressure inside the microchannel. In order to measure the effects of W_{PDMS} and H_{PDMS} in the viscous fluid domain, the variation of the acoustic pressure inside the microchannel was studied in the middle of the microchannel. The same parameter values used in Section *4.1.3.* was used for this section except for the width and the height of PDMS.

In Table 4-5 and Table 4-6 the correlation between the normal component of the displacement measured at the top edge of $LiNbO_3$ in different W_{PDMS} (constant H_{PDMS}) and different H_{PDMS} (constant W_{PDMS}) is shown. Once acoustic waves reach the PDMS domain, they start to propagate in PDMS at the Rayleigh angle, and hence, the normal component amplitude of the displacement decreases exponentially before reaching the fluid domain. The results show that the displacement decreases from 30 Å to 15 Å by increasing W_{PDMS} from 1 mm to 4.5 mm at the constant H_{PDMS} (Table 4-5). However, this behavior was not followed by varying H_{PDMS} (at constant W_{PDMS}), and not a significant variation in the displacement magnitude was observed (about a 6% reduction in the displacement amplitude by raising H_{PDMS} from 1 mm to 5 mm at the constant W_{PDMS} (Table 4-6).

Table 4-5. Effects of the width of PDMS (at the constant PDMS height) on the normal component of the displacement in $LiNbO_3$ and on the acoustic pressure amplitude in the fluid

PDMS thickness		Y (normal) component of displacement (Å)
$H_{PDMS} = 4.0\ mm$	$W_{PDMS} = 1.0\ mm$	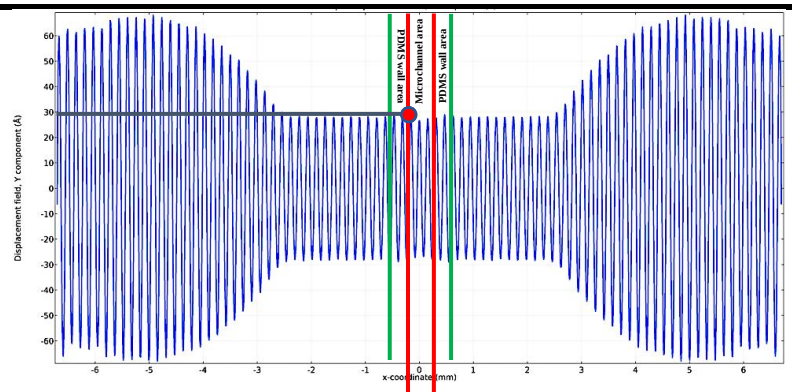
	$W_{PDMS} = 2.0\ mm$	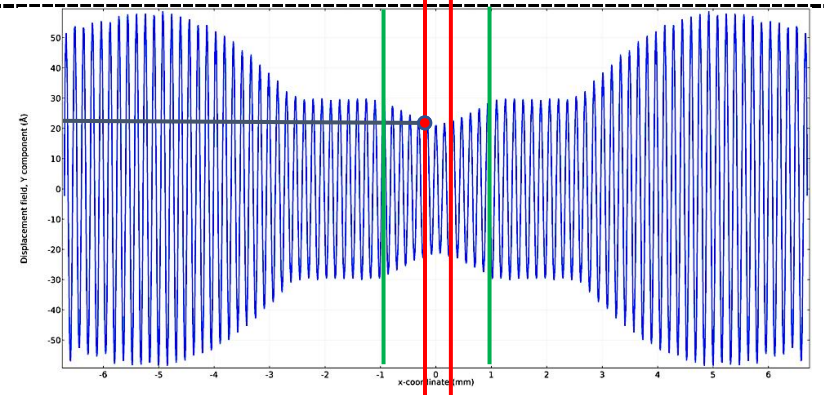
	$W_{PDMS} = 4.5\ mm$	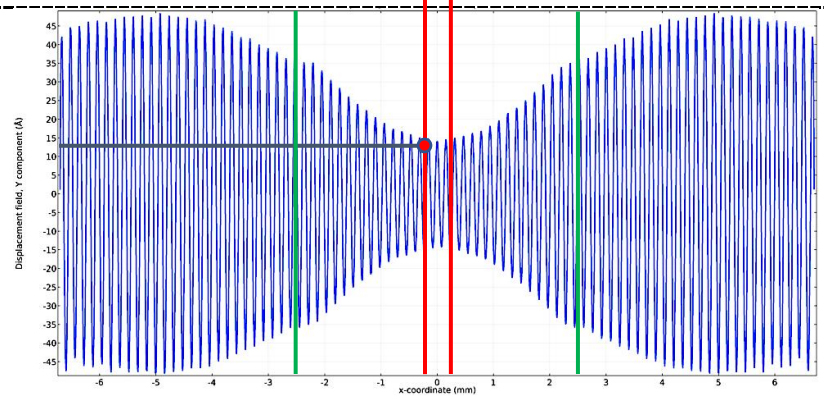

Table 4-6. Effects of the height of PDMS (at the constant PDMS width) on the normal component of the displacement in LiNbO3

PDMS thickness		Y (normal) component of displacement (Å)
$W_{PDMS} = 4.5\ mm$	$H_{PDMS} = 1\ mm$	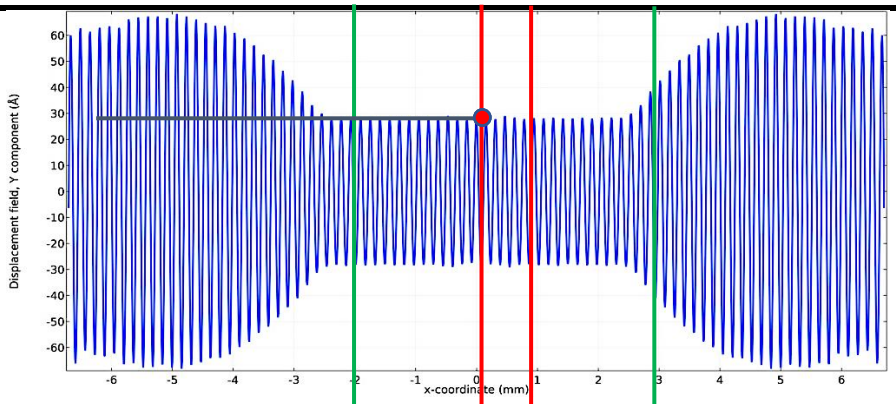
	$H_{PDMS} = 3\ mm$	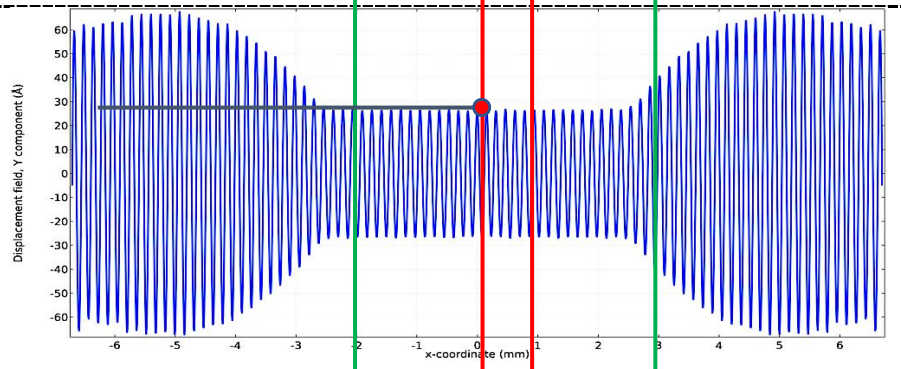
	$H_{PDMS} = 5\ mm$	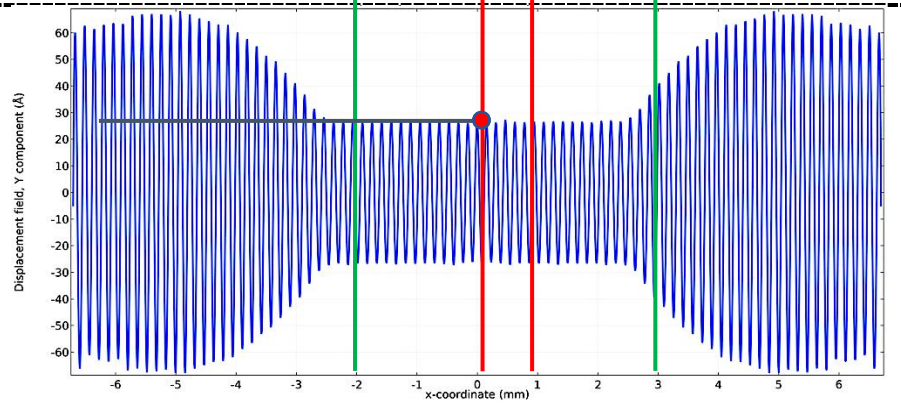

Furthermore, the same trends were followed by the acoustic pressure of the fluid trapped inside the microchannel. As it is shown in Table 4-7, the acoustic pressure decreases substantially from 1500 kPa to 900 kPa by increasing W_{PDMS} from 1 mm to 4.5 mm (at constant H_{PDMS}). However, in the vertical cutline (i.e., at the distance of 1.4 mm from the bottom of the PDMS), the acoustic pressure reaches ~ 0 kPa indicating that most of the SAW energy is dissipated within 1 mm from the bottom of PDMS. The results indicate that SAW energy dissipation is dependent only on W_{PDMS}; modifying H_{PDMS} does not affect the displacement magnitude and the acoustic pressure to a significant level, and hence will not be considered for the next steps of this study.

Table 4-7. The acoustic pressure variation at different widths and heights of PDMS across the vertical and horizontal cut-lines

Cutline Direction	Acoustic Pressure (AP) variation [kPa] across PDMS domain
Horizontal	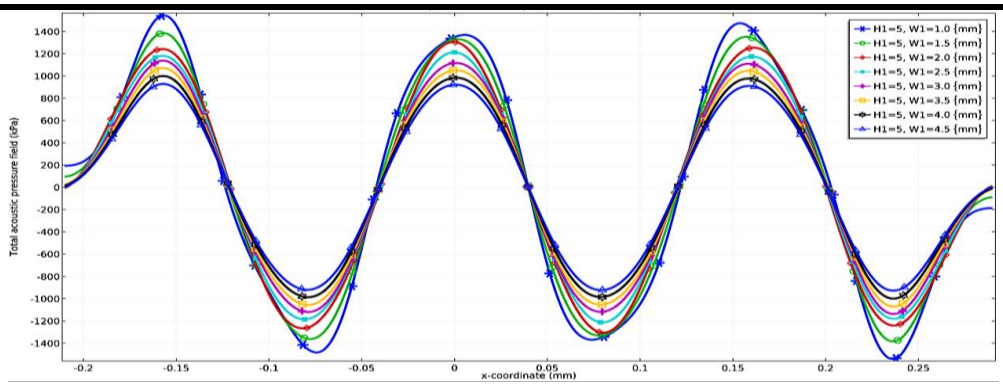
Vertical	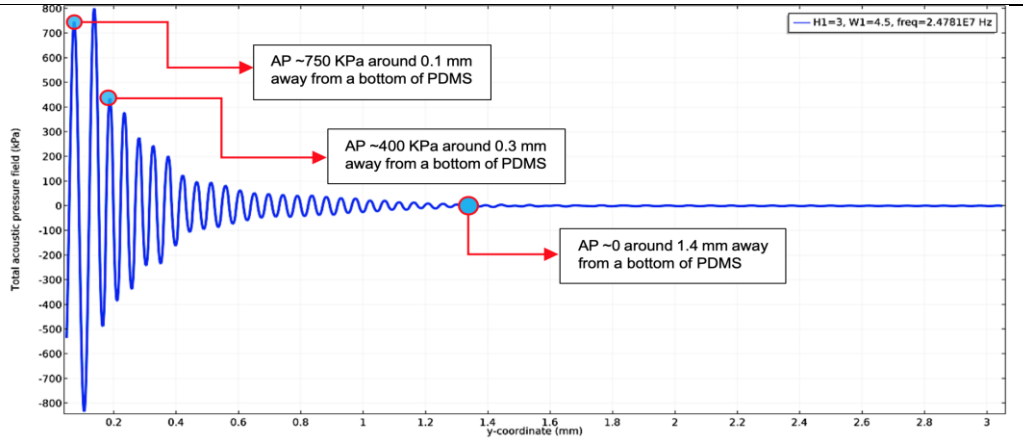

4.1.6. Effects of number of IDT fingers on the acoustic pressure amplitude

The number of finger pairs (N_p) of IDTs is an important parameter partially due to its effect on the quality factor [150] and the effective piezoelectric coupling coefficient of the substrate. The greater

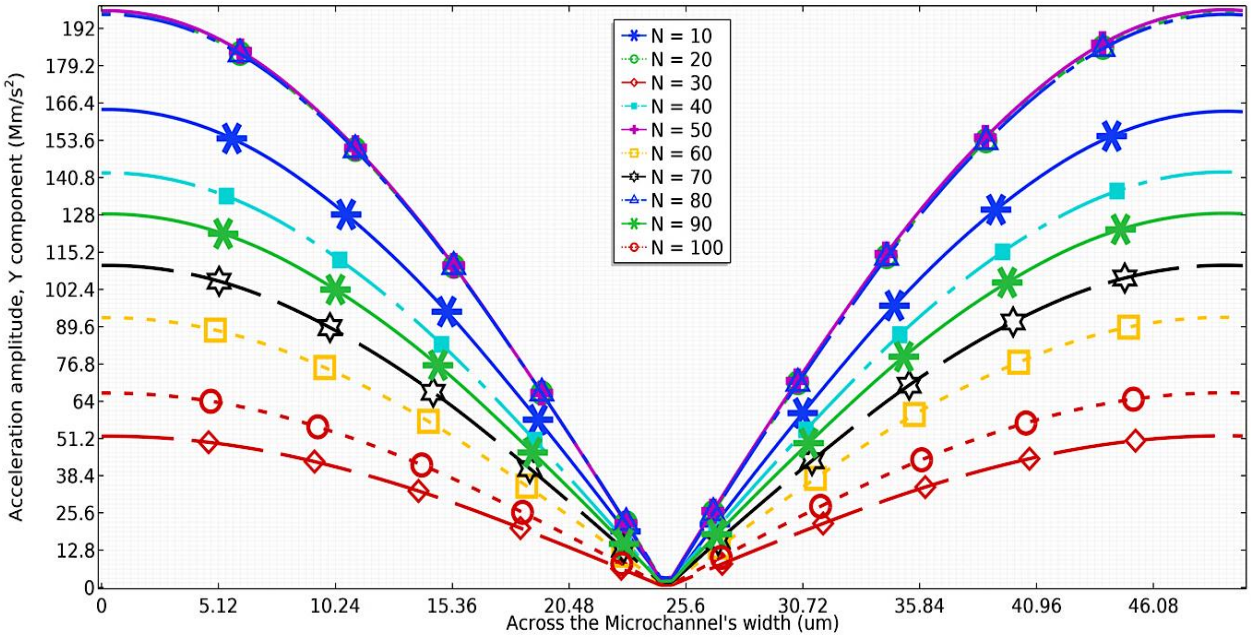

Figure 4-2. The variation of the normal component of the acceleration across the width of the microchannel for different values of the IDTs fingers.

the coupling coefficient, the greater the amount of energy that can be transduced in the IDTs (leading to a higher magnitude of AP). The energy transfer goes up by increasing N_p up to the material-dependent limit [95]. However, the bandwidth reduces due to mismatching that happened in the impedance between IDTs pairs and the signal source [92], [95]. The basic concept behind this phenomenon is explained in signal processing: when the voltage V_0 is applied to IDTs, the power is both absorbed and produced; this behavior is defined by the electrical admittance of the IDTs including capacitance, conductance, and susceptance. At a certain frequency, susceptance becomes negative and begins to counteract with capacitive. When these terms cancel out, the admittance becomes real and directly corresponds to a resistive load and to the most efficient

operation of the IDTs [90], [92]. As the majority of signal generators use a widely accepted standard of $50\ \Omega$ for their resistive load, a suitable N_p must be used in the final design to match the impedance of RF signal generator and IDTs [90]. To find a suitable number of IDT fingers providing maximum energy transmission, the relationship between the magnitude of the normal component of displacement (the absolute value) and energy transmission on N_p are studied parametrically. Figure 4-2 are in contact. Based on the result, $N_P = \{20, 50, 80\}$ provide the maximum magnitude of acceleration which is in the good agreement with the previous study [92] indicating $N_P = 21$ provides the most efficient operation of the IDTs. As for microfabrication of the IDTs, the number of IDT fingers of 21 is much easier than 50 and 80. Thus, $N_P = 21$ has been considered for fabricating IDTs.

4.1.7. Microparticle trajectories based on acoustic pressure field

The "Microparticle Tracing" module in COMSOL Multiphysics® software package was used to calculate trajectories in varies times inside the microchannel. This module evaluates the location of each microparticle independently at different time frames. It is worth mentioning that since the cross-section of the acoustofluidic chip was modeled in this study, the drag force imposed by the convection term of the fluid flow was neglected as the direction of the fluid flow is in/out of the computational domain and cannot distract X and Y directions of the microparticle motion. For this part of the simulation, 2000 microparticles were released at time = 0 [S] and distributed homogenously. Then, the ARF and the drag forces were applied to them. It is worth mentioning that the values of the applied parameters were the same as previous sections; however, to validate the results of this section, some of the parameters (the applied RF signal and the wavelength) were

adjusted based on the values of 1D HSW simulation of Shi et al. [151]. Consequently, the applied voltage was adjusted to provide the electrical power of $50\ mW$.

At first, the influences of the frequency and the microparticle's diameter were investigated by the parametric study. We evaluated the value of ARF along the horizontal cutline passed through the width of the microchannel by plotting ARF in different conditions represented in Eqs. (2.17) and (2.20). Note that the microchannel was shifted by $\lambda_{SAW}/4$. As it can be seen from Table 4-8, as the wavelength increases from $100\ \mu m$ and $200\ \mu m$, the maximum value of ARF for the particle diameter of $d_P = 10\ \mu m$ decreases from $\sim 0.210\ nN$ to $\sim 0.140\ nN$ (45.5% reduction). At each wavelength, by increasing the size of the microparticles from $5\ \mu m$ to $15\ \mu m$, ARF was increased around 2,500% which is in good agreement with Eq. (2.15). Additionally, three PNs and two PANs were formed inside the microchannel since the width of the microchannel is equal to the wavelength. The results demonstrate that both PNs and PANs are located where the amplitude of ARF reaches zero; however, PNs only occurs when the direction of ARF is inward while the PANs should be outward. This behavior can be due to various factors influencing ARF: based on the Eq. (2.17), the maximum value of ARF occurs when the acoustic potential field (U) experiences the maximum gradient. Table 4-8 demonstrates that the maxima of U are located between each PN and PAN where there is a maximum gradient of U. Nonetheless, the gradient of U at PNs and PANs locations is zero due to the occurrence of maxima and minima of the acoustic pressure (P) and acoustic velocity (v) in PANs and zero value of both P and v in PNs. These figures demonstrate that by moving closer to PNs and PANs, the magnitude of ARF decreases in which causes a longer time period for a microparticle migration.

Table 4-8. ARF distribution across the width of the microchannel

Wavelength	Acoustic Radiation Force (ARF) variation across the microchannel's width
$\lambda_{SAW} = 100\ \mu m$	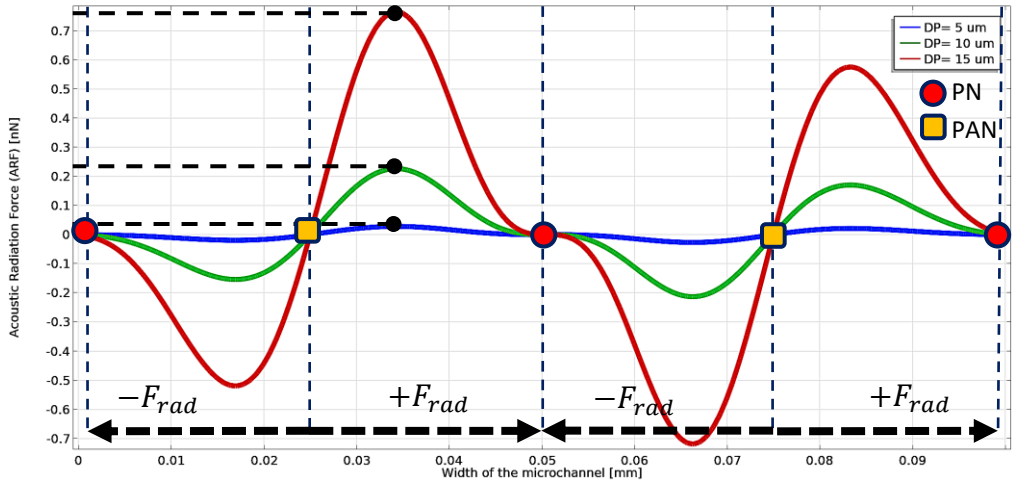
$\lambda_{SAW} = 200\ \mu m$	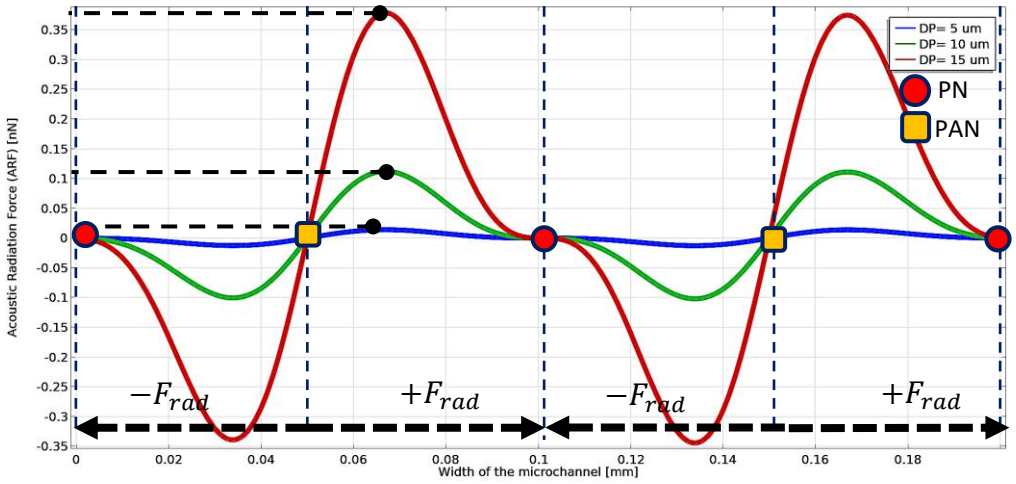

In the next step, the distribution of microparticles while ARF is acting on them was simulated. The distribution of the microparticles was shown in two different wavelengths (100 [μm] and 200 [μm]) at various time frames. The calculated optimum values of the previously discussed parameters were used for this step Table 4-9 shows the microparticles migration toward the PNs at two different time frames of 0.5 [s] and 1.0 [s]. It can be seen that microparticles move to the

middle of the microchannel and along the sidewalls which are the location of the PNs. The microparticles are shown as points along with the pathways their have followed from their initial to the final locations. The PNs and PANs locations are shown as the black and pink bars at each time frame. When the wavelength is $100\ \mu m$ ($f_0 \sim 38.5\ MHz$), the microparticles with the diameter of $d_P = \{1, 5, 10\}\ \mu m$ migrate toward PNs faster when the wavelength of $200\ \mu m$ ($f_0 \sim 19.3\ MHz$). As an example, the required time for the $1\ \mu m$ microparticle to move toward the middle PN is significantly longer at a constant wavelength compare to the $5\ \mu m$ and $10\ \mu m$ microparticles (as about 99% of the microparticles with a diameter of $5\ \mu m$ and $10\ \mu m$ microparticles have already reached the middle PN while this value for the $1\ \mu m$ is about 75%). The same behavior was observed for the wavelength of $200\ \mu m$ ($f_0 \sim 19.3\ [MHz]$). However, the percentage of the microparticles moved to PNs at the same time period (0.5 [s] and 1.0 [s]) relatively smaller in comparison to that evaluated at the wavelength of $100\ \mu m$ ($f_0 \sim 38.5\ MHz$): 90%, 60%, and 5% for $10\ , 5, 1\ [\mu m]$ microparticles, respectively. These results agree perfectly with previous studies: Shi et al. [151] claimed that the required times for $10, 5, 1\ [\mu m]$ microparticles to move from the sidewalls to the middle PN at $\lambda_{SAW} = 200\ [\mu m]$ are 0.2 [s], 0.5 [s], and 6 [s] by implementing the 1D HSW numerical simulation, respectively. Our results indicated half of these values for the complete course of the migration toward the middle PN. The main reason for this discrepancy is that three PN lines are were located in the microchannel and hence the half distance is required for the microparticles to positioned completely at PNs. Additionally, results revealed that ARF also has a vertical component acting on the microparticles and causes microparticles migration in the vertical direction. At the final stages of the microparticles movements to PNs, they hence have attached to the sidewalls of the microchannel. This means that if the height of the microchannel is relatively larger than the wavelength, multiples

PNs and PANs are created inside the microchannel leading not only the microparticles migration to vertical PNs but also to the horizontal PNs. These results show that 1D HSW simulations cannot predict the microparticle movement correctly and there is always a bias in the results of such simulations.

Table 4-9. The numerical simulation of the microparticles distribution while ARF is acting on different sizes of microparticles in two different time frames of 0.5 [s] and 1.0 [s] categorized based on the applied resonance frequency

Wavelength	Time	1 μm	5 μm	10 μm
$\lambda_{SAW} = 200\ \mu m$	0.5 [s]	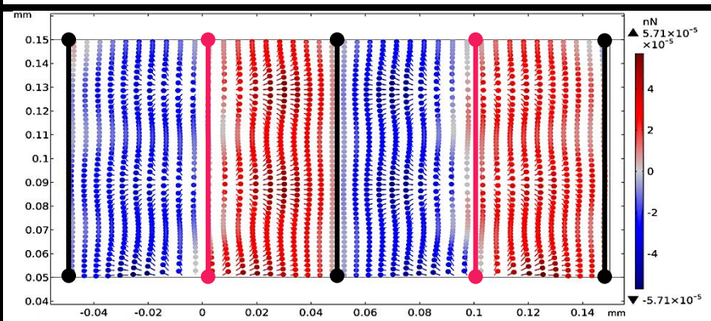	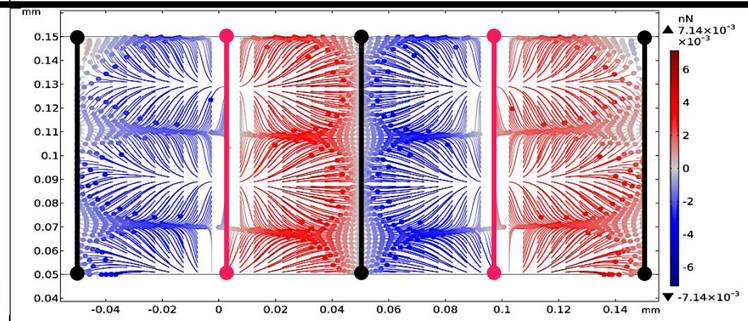	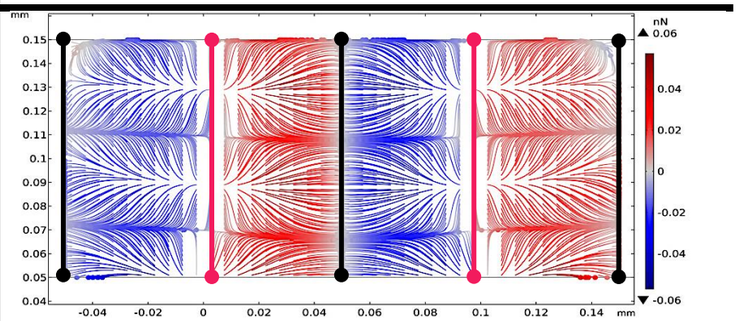
	1.0 [s]	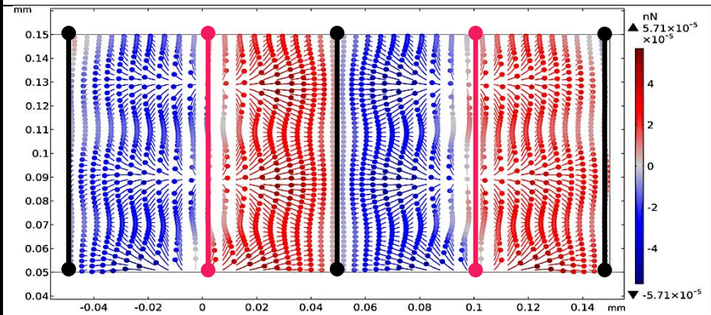	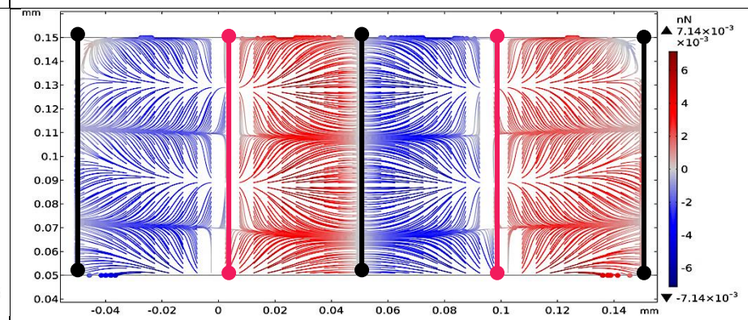	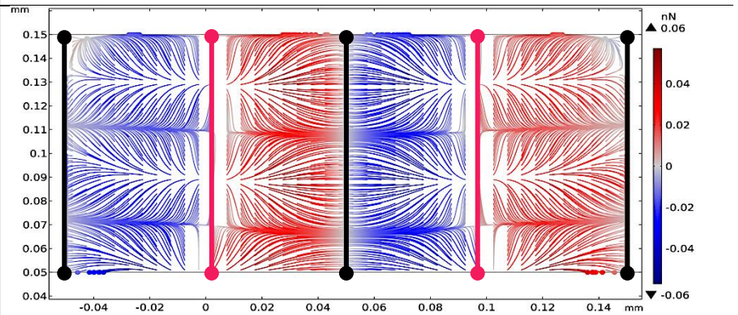
$\lambda_{SAW} = 100\ \mu m$	0.5 [s]	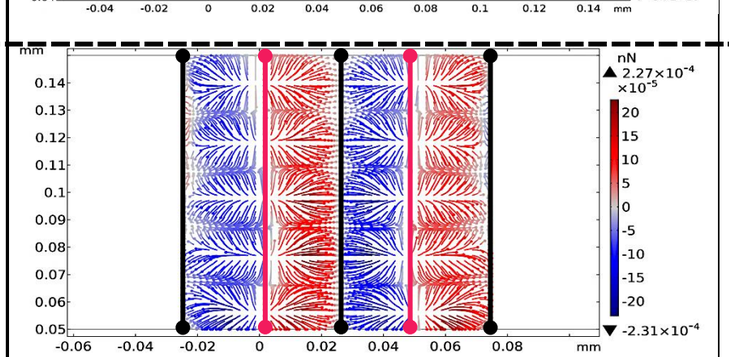	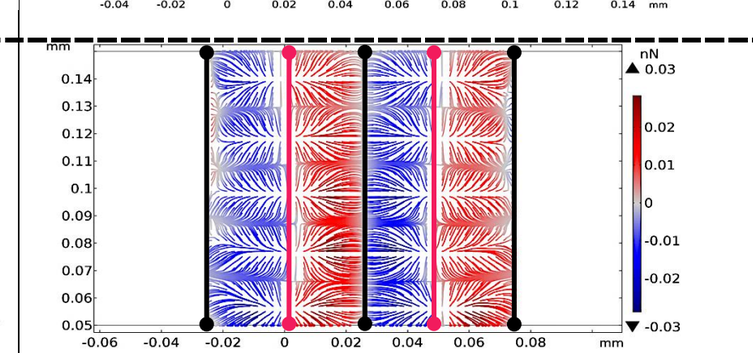	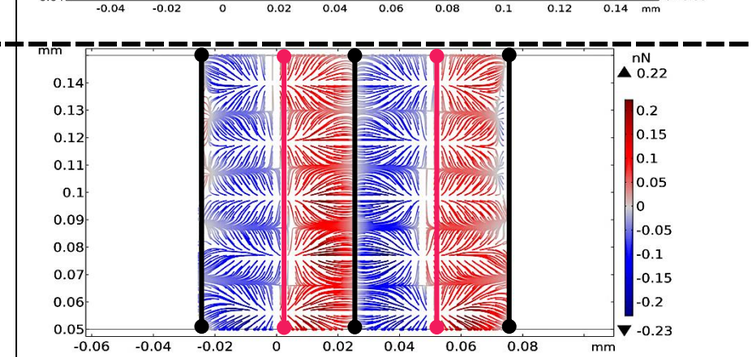
	1.0 [s]	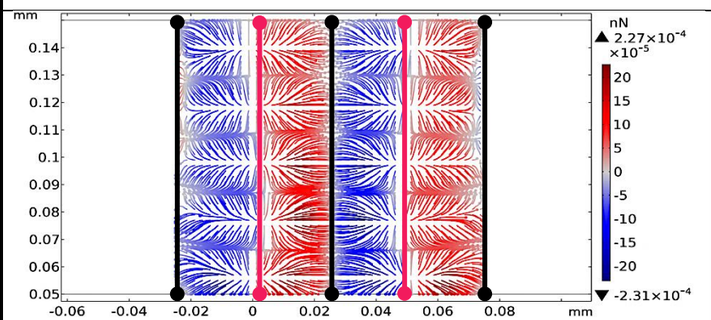	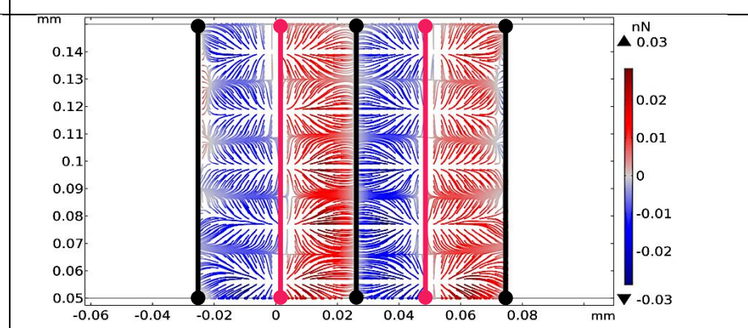	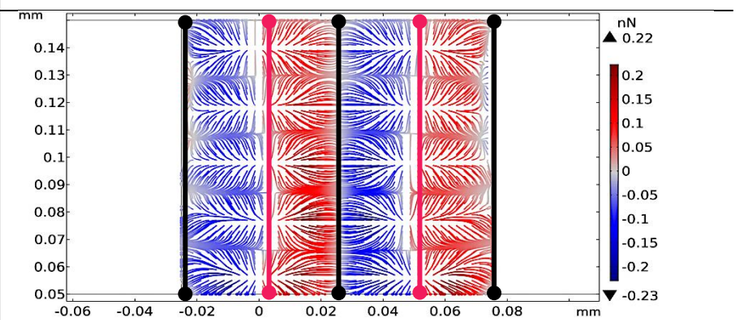

4.2 Experimental results

An experimental study was performed to validate our numerical results. The PS microparticles injected to the microchannel by the syringe pump at the fixed flow rate of $1\ \mu L/min$. To compare the results of our proposed numerical simulation, the same applied parameters were applied during the experiments. The following sections show the microparticle motion at different applied conditions. There are three approaches for validating the aforementioned numerical simulation results with the experimental tests: ARF acting duration, the amplitude of the applied voltage to the IDTs, and the number of IDT fingers. Herein, the operational conditions and/or device geometry characteristics of the acoustofluidic chip were modified to the employed parameters in the numerical simulation section.

4.2.1. Effects of ARF on the microparticle migration

ARF has a direct correlation to the RF power applied to IDTs and the volume of the microparticles. However, if the duration of ARF is long enough, all of the various sizes of the microparticles migrate eventually to PNs, regardless of their diameters and density. Thus, we experimentally studied the time scale for a complete course of the microparticle migration toward PNs. As it is shown in Table 4-10, the PS microparticles with the size of $5\ \mu m$ and $10\ \mu m$ were injected and filled out the microchannel homogenously (initial state). Next, the signal generator applied RF signal to the IDTs with the amplitude of $V_0 = 5\ [V]$ peak-to-peak. Result revealed that $5\ \mu m$ and $10\ \mu m$ PS microparticles required time $t = 1.0\ [\mathrm{s}]$ and $t = 0.25\ [\mathrm{s}]$ to complete their full migration course toward the nearest PNs. In the next step, we used an image analysis tool (MATLAB, version 2019a, Image Processing Toolbox) to increase the contrast of images and calculate the pixel values along each PN line (shown as red color bars in Table 4-10).

In the next step, a quantitative analysis was conducted by evaluating the average (AVE) of each PN line. This analysis was carried out by the developed MATLAB code provided in Appendix A. In this code, a green channel of color images also called RGB images (R: red, G: green, and B: blue) is derived due to its higher color contrast compared to the red and blue channels. The pixel values are between 0 and 255 (indicating the highest and lowest color intensity, respectively). These values are relative to each other as the color intensity of each size of the microparticles is different from one another. Thus, all data were normalized by dividing them to 255 (maximum value of the pixels). The evaluated data for 5 μm and 10 μm PS microparticles at their initial and final states are shown in Table 4-11. The last column indicates the cumulative averaged values of PN lines at each state where it is 0.2393 and 0.4767 for 5 μm PS microparticles at the initial and final states, respectively. However, 0.1836 and 0.0468 were evaluated for $10\,\mu m$ PS microparticles, respectively. In order to evaluate the microparticle deflection/manipulation acoustic radiation coefficient of performance in the acoustofluidic chip, we introduced the acoustic radiation coefficient of performance called COP_{rad}, which is expressed as:

$$COP_{rad} = \frac{AVE_f}{AVE_i} \qquad (4.1)$$

where *f* and *i* subscripts indicate final and initial states of the microparticles, respectively.

According to Eq. (4.1), the efficiency of $COP_{rad} \sim 2$ and 4 were derived for 5 μm and 10 μm PS microparticles, respectively. This result shows that the COP_{rad} is almost double for $10\,\mu m$ PS microparticles compared to 5 μm PS microparticles which agree well with those estimated from the numerical simulation (see Section 4.1.7) and the previously mentioned required time (t).

Table 4-10. The 5 μm and 10 μm PS microparticles migration to PNs at different time frames with the constant applied voltage

Test condition	Wavelength = 200 μm Applied RF signal amplitude = 5 [V] peak-to-peak Microchannel width and height = {800 and 100} [μm]			
	Microparticle size = 5 μm		Microparticle size = 10 μm	
Time	Intinal state/Acoustic OFF	Final state/Acoustic ON	Initial state/Acoustic OFF	Final state//Acoustic ON
Distribution of PS microparticles	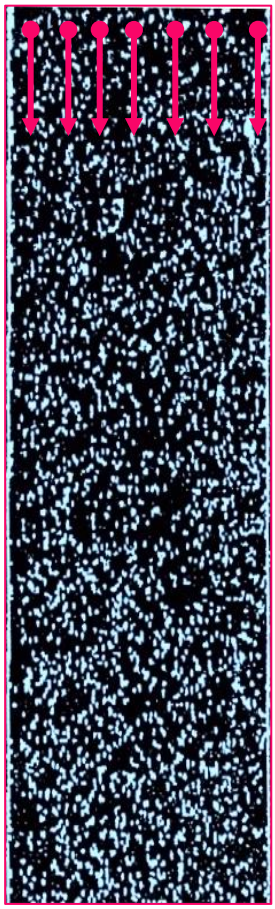	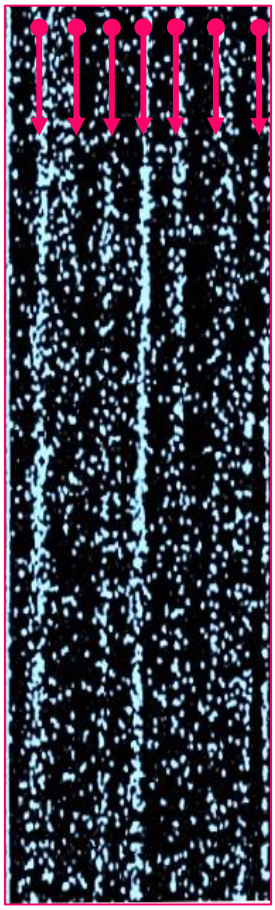		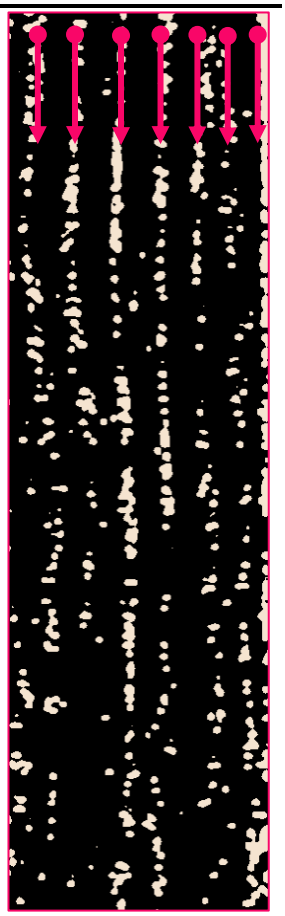

Table 4-11. The Averaged value of the PN lines for 5 μm and 10 μm PS microparticles at the intial and final states.

PN number		PN 1	PN 2	PN 3	PN 4	PN 5	PN 6	PN 7	Average
5 μm Microparticle	**Final state Acoustic ON**	0.4997	0.3476	0.2695	0.4499	0.7287	0.4344	0.6068	0.4767
	Intinal state Acoustic OFF	0.2363	0.2667	0.2594	0.2315	0.2076	0.2686	0.2048	0.2393
10 μm Microparticle	**Final state Acoustic ON**	0.1746	0.1684	0.1815	0.2082	0.1909	0.1929	0.1685	0.1836
	Initial state Acoustic OFF	0.0695	0.0391	0.0522	0.0709	0.0378	0.0304	0.0277	0.0468

4.2.2. Effects of applied RF signals on the microparticle migration

The amplitude of the applied RF signal (input power P_0) has a direct correlation to the magnitude of AP and ARF: the higher the input power, the higher the efficiency and the smaller the time period required. However, the increase in the input power and hence ARF would cause Joule heating and causes clot formation inside the microchannel, which can disturb the flow direction, throughput, and functionality of the microchip [152]. Herein, we carried out a test to investigate the effect of V_0 on 10 μm PS microparticle migration by increasing V_0 with a rate of 1 $[V/s]$. For each applied voltage, the corresponding numerical simulation with the same operational conditions is shown below the experimental result. The illustrated numerical results provide the

microparticles positions along with their migration pathways at the same V_0. It is worth mentioning that the 3 [ms] of exposure time was set in the microscope for a live recording of the microparticle motion. As a result, the trajectories of the microparticles were captured at $t_0 = 0.003\ [s]$ in the numerical simulation to match the experimental recording interval.

As can be seen from Table 4-12, as V_0 goes up from $0.0\ [V]$ to $5.0\ [V]$ with an increment of $2.5\ [V]$, a large number of PS microparticles moves toward the nearest PNs (almost 30% of the microparticles have reached PNs by $V_0 = 5.0\ [V]$. The same behavior was observed in the numerical simulation results as for $V_0 = \{2.5, 5.0\}\ [V]$, the majority of $10\ \mu m$ microparticles could not complete their migration course completely. When $V_0 = 5.0\ [V]$, $10\ \mu m$ microparticles are deflected by ARF. However, a small portion of them reached PNs (those which were closer to PNs). Then, we increased V_0 from $10.0\ [V]$ to $20.0\ [V]$ with a rate of $5\ [V/s]$ in order to minimize the impact (bias) of ARF action duration. Both numerical and experimental results showed that the majority of the microparticles reached their nearest PNs by $V_0 = 15.0\ [V]$. Nonetheless, we continued increasing the applied voltage to investigate the impact of the high voltage on the microparticles movement. The results indicated that at the voltage of $V_0 = 20.0\ [V]$ clot formation happens which disturbed the flow direction and there was no difference in the location of the microparticles in the numerical simulation compared to $V_0 = 15.0\ [V]$ and the onward values. The main reason behind this phenomenon is the vertical component of ARF which pushes the microparticles toward the top of the microchannel, and hence due to adhesion between the microparticles and the microchannel, they attached to walls of the microchannel creating an aggregation of the microparticles.

Table 4-12. Displacement of 10 *μm PS microparticles at the various applied RF signals amplitude*

$V_0 = 0.0\ [V]$	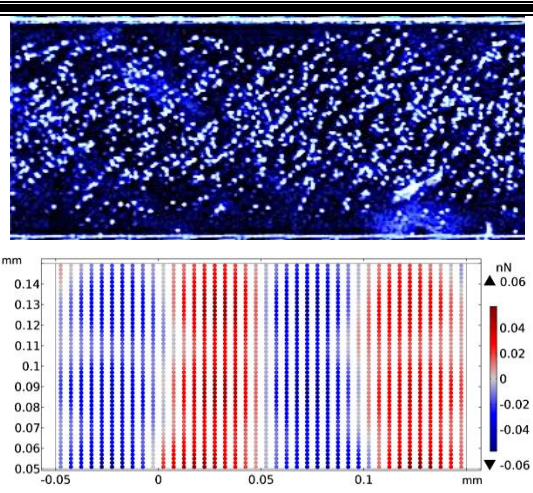	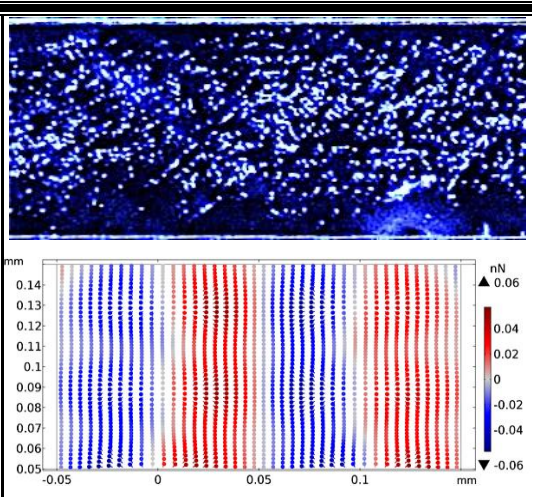
$V_0 = 5.0\ [V]$	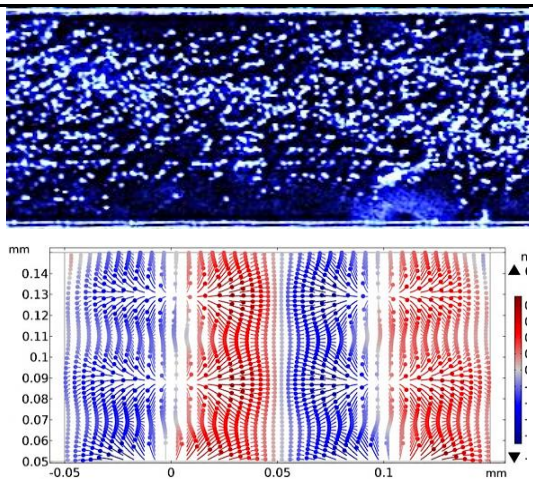	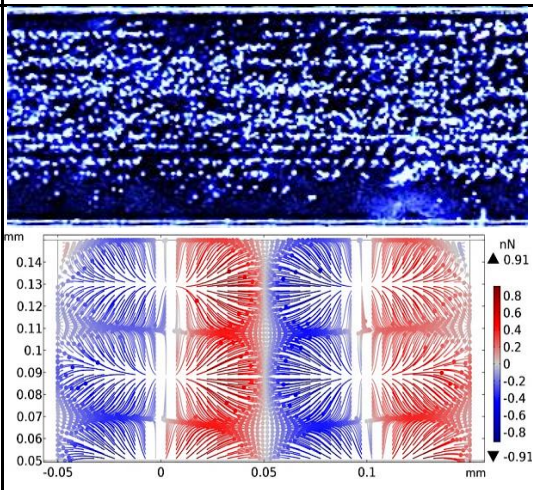
$V_0 = 15.0\ [V]$	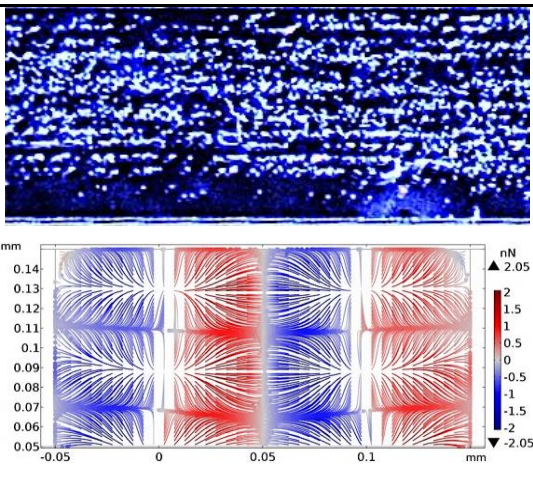	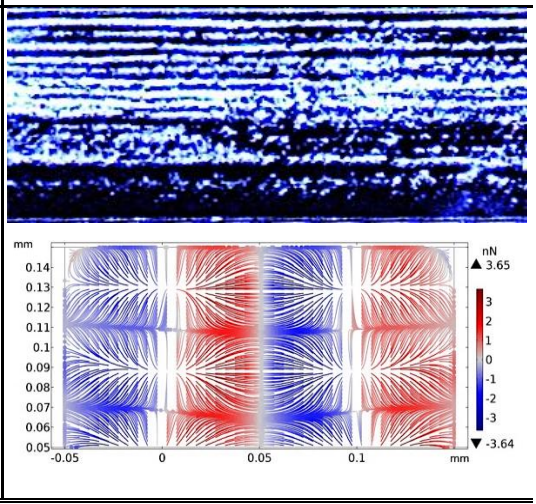
$V_0 = 20.0\ [V]$		

4.2.3. Effects of the number of IDT fingers

As aforementioned in the numerical simulation section, number of IDT fingers (N_P) plays an important role in the magnitude of AP and ARF. However, due to the nonlinearity and the complexity of the electrical circuit modeling of IDTs energy transmission, finding proper N_P is not a trivial task. The numerical simulation results demonstrated that $N_P = \{20, 50, 80\}$ provides the most efficient energy transmission for the acoustofluidic chips. In order to validate this, we designed two microchips with different $N_P = \{20, 100\}$ (see Figure 4-2). Table 4-13 shows PS microparticle migration toward PNs at two different test conditions: the first row demonstrates $5\ \mu m$ PS microparticles movement (at two different time frames) for $N_P = 20$, and the second row demonstrates $20\ \mu m$ PS microparticles movement (at two different time frames) for $N_P = 100$. Although the size of $20\ \mu m$ PS microparticles is 4 times larger than $5\ \mu m$ PS microparticles (and hence ARF would be 64 times larger in the magnitude) and the amplitude of V_0 is 1.5 times larger, they are not completely aligned along the PN lines due to inappropriate N_P values. The results of this section agree well with those presented in Section 4.1.6. and demonstrate the importance of N_P in the acoustofluidic chips designing.

Table 4-13. The comparison of the number of IDT fingers on 5 μm and 20 μm PS microparticles migration; yellow and black colored dash-lines indicate PN lines.

Test conditions	Wavelength $= 100\ [\mu m]$ PDMS width = 3 [mm] PDMS height = 1 [mm]	Microchannel's width = $800\ [\mu m]$ Microchannel's height = $100\ [\mu m]$
Microparticle size = $5\ [\mu m]$ $V_0 = 10.0\ [V], N_P = 20$	$Time = 1.0\ [S]$ 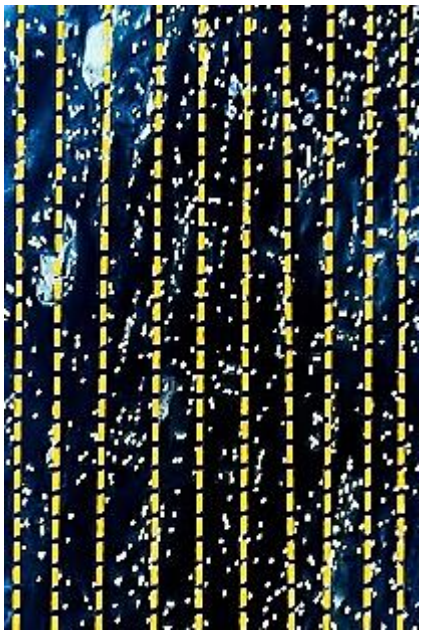	$Time = 2.0\ [S]$ 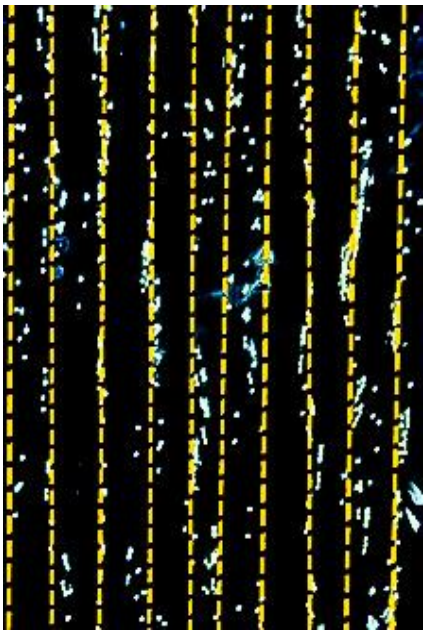
Microparticle size = $20\ [\mu m]$ $V_0 = 15.0\ [V], N_P = 100$	$Time = 1.0\ [S]$ 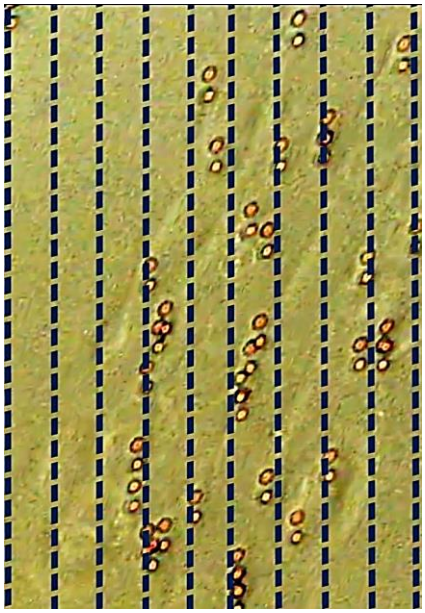	$Time = 2.0\ [S]$ 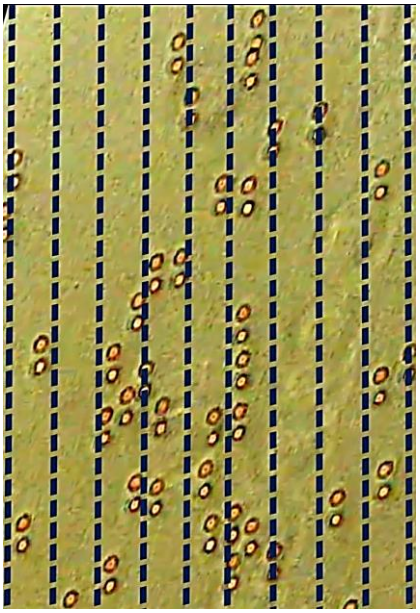

Chapter 5: Microparticle separation with tilted Standing Surface Acoustic Wave

5.1 Unique features of tilted standing surface acoustic wave (tSSAW)

Since the pressure nodes (PNs) lines are parallel to each other in pSSAW, the precise alignment is required for having specific numbers of PNs across the width of the microchannel [73]. In order to eliminate the precise alignment requirement for the microfabrication of pSSAW, a tilted standing surface acoustic wave (tSSAW) method was introduced by Ding et al. [110]. In this method, the microchannel is inclined at a specific angle instead of being parallel to IDT fingers. Such a modification causes the PN lines to be formed in the tilted direction to the fluid flow. As mentioned before, two forces are present inside the microchannel: the drag force and ARF. While the microchannel is inclined with respect to the fluid flow direction, the migration distance of the microparticles across the width of the microchannel is significantly longer (compared to the pSSAW case), which leads to better controllability of the separation or manipulation. Furthermore, the precise microchannel alignment does not have priority in this method (unlike pSSAW) due to the presence of the multiple tilted PN lines. The working mechanism of this method relies on escaping and re-capturing by different PN lines; in essence, the larger microparticles can be trapped again by the neighboring PN lines while the smaller ones are not affected by ARF and remain on the main flow stream [153]. Additionally, a lateral displacement of the microparticles in tSSAW is relatively higher than of pSSAW. This promotes more controllability and higher separation efficiency [154].

Figure 5-2 illustrates the working mechanism of the tSSAW microfluidic device. As it is shown, the PDMS microchannel is placed on a surface of the piezoelectric substrate containing patterned

pair of IDTs. The microchannel is tilted at a specific angle relative to IDTs fingers. The two traveling SAWs propagate in the opposite directions on the substrate surface and leak into the liquid inside the microchannel. The interference between them forms an SSAW field and causes an establishment of a series of PNs and PANs in the microchannel at an angle tilted to the fluid flow direction. As a result, the microparticles will travel through multiple regions of PN and PAN pairs which are incrementally moving them until they reach another sidewall of the microchannel.

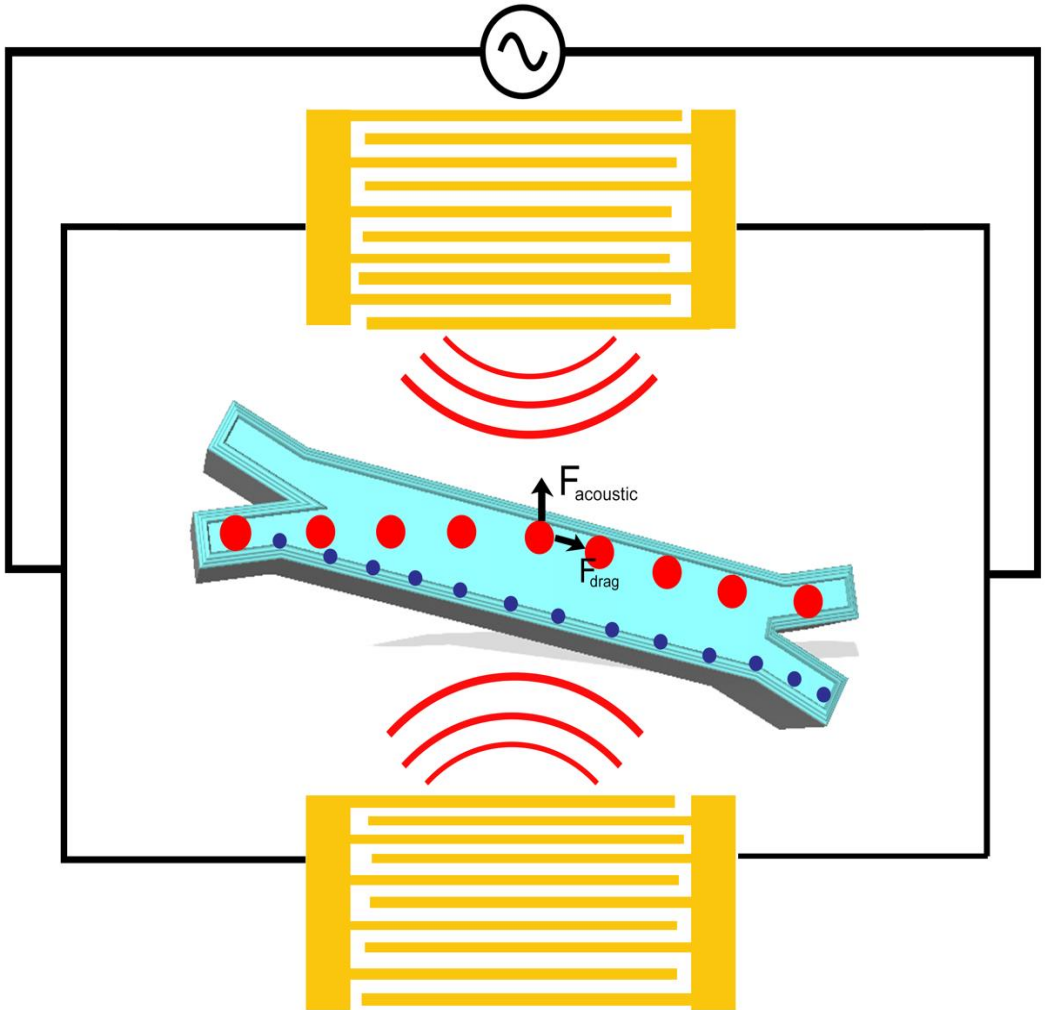

Figure 5-1. Schematic of the tSSAW device where the microchannel is titled with respect to the IDT fingers. The sample flow containing different sizes of the microparticles is injected from one the inlet along the with the injection of the sheath flow from another inlet. The microparticles larger than a cutoff size are deflected and move toward another sidewall of the microchannel while the smaller ones remain on the mainstream.

Thus, the tSSAW method does not have the limitation of pSSAW in the separation distance which is limited to a quarter of the wavelength [154].

For tSSAW, we again start with numerical simulation to eliminate bias errors encountered in the experiments and to determine optimized parameters that must be considered in the microfabrication step. Upon deriving the optimum values of the parameters, the chip is fabricated and tested with PS microparticles. The following sections explain the numerical simulation and experimental setup carried out for tSSAW.

5.2 Numerical simulation of tSSAW

The numerical simulation has been used recently for tSSAW [154], [155]. Most of the previously reported studies [111], [114] considered 2D cross-section of the acoustofluidic chip in their numerical analysis due to the uniformity of the pSSAW field in the longitudinal direction of the microchannel. However, this assumption is not valid for tSSAW as the microchannel is tilted respect to the traveling SAWs propagation and the SSAW field is different along the length of the microchannel. In order to overcome this limitation, 1D HSW was employed in the most recent studies [110], [155]. However, the actual acoustic pressure distribution in the microchannel is significantly different from that predicted by a 1D HSW model [111]. As a result, employing 3D simulation is inevitable for tSSAW modeling.

5.2.1. Numerical simulation procedures

The commercial software COMSOL Multiphysics® (version 5.4, www.comsol.com) was used to perform the numerical simulation based on the finite element analysis (FEA) method. Herein, a 3D computational domain including $LiNbO_3$ piezoelectric (used as a substrate patterned with IDT fingers upon a top surface of it) and tilted microchannel placed between two pairs of IDTs (Figure 5-2). The amount of angle that the microchannel is inclined is shown by θ symbol. Based on the results of the last chapter, the optimum values for the number of IDT fingers is 21 for each pair and then this value was implemented in this study. Additionally, it has been claimed that by increasing the magnitude of the applied RF signal, more microparticles are affected by ARF up to a limit which is determined by a buffer that microparticles are suspended in it. This limit should

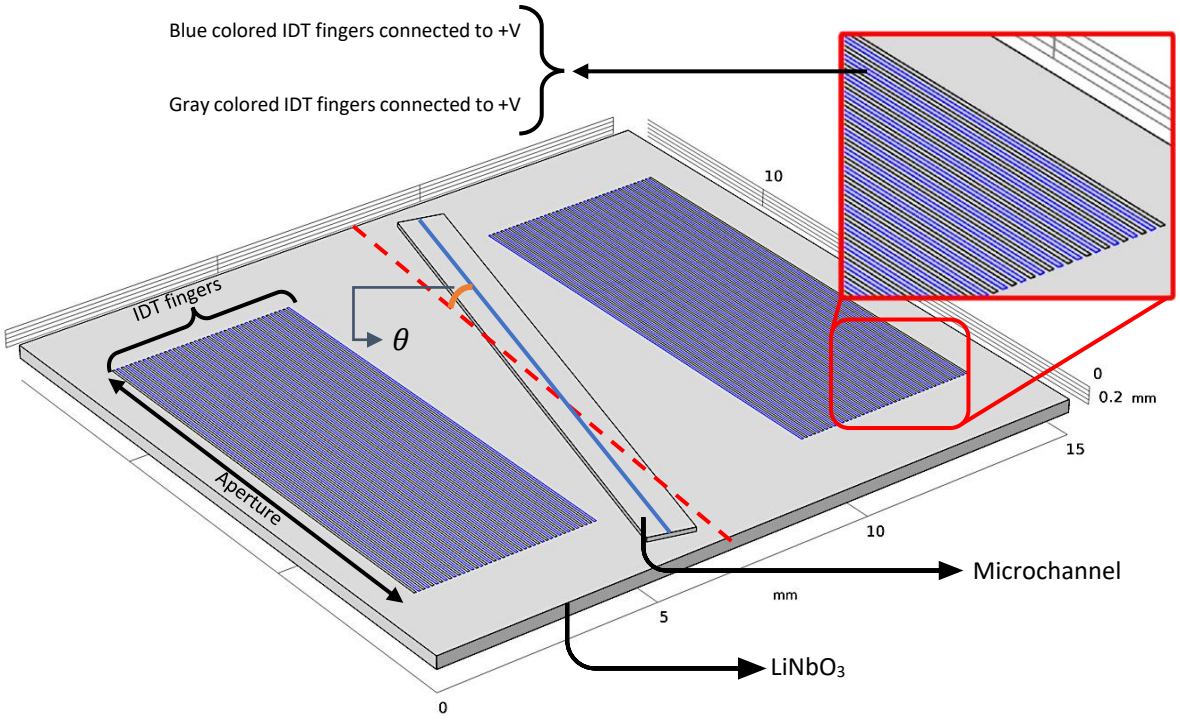

Figure 5-2. The employed computational domain consisted of the piezoelectric substrate ($LiNbO_3$) and microchannel.

be always considered for any experiments to prevent joule heating generation followed and bubbles generation in the fluid.

In order to simulate tSSAW generations and propagation in the substrate and the microchannel, three modules must be used in COMSOL Multiphysics®: 'Electrostatics', 'Solid Mechanics', and 'Pressure Acoustic, frequency domain'. The first two modules are fully coupled under the 'Piezoelectricity Multiphysics' section of the software. The 'Solid Mechanics' and 'Electrostatics' modules calculate the SAW field in the piezoelectric substrate. The substrate used again is lithium niobate (YX 128° cut) due to its high electromechanical coupling coefficient compared to other piezoelectric materials [92], [93], [103]. Unlike the 2D simulation that the piezoelectric material matrices must be rotated manually prior to using them in COMSOL Multiphysics®, this modification is done easily by changing the geometry orientation. To modify default material properties [156] of lithium niobate to YX 128° cut orientation, a rotating system should be defined in software properly. COMSOL Multiphysics® uses Euler notations (Z-X-Z; α, β, γ) for a geometry orientation and as a result, material matrices (the elasticity, electromechanical coupling coefficient, and relative permittivity) must be rotated by [$\alpha = 0$, $\beta = 38°$, $\gamma = 0$] for lithium niobate YX 128° cut. Additionally, the thickness of the substrate must be set to at least two times of the SAW wavelength ($2 \times \lambda_{SAW}$) to avoid disruption in the energy dissipation. Furthermore, a low-reflecting boundary condition was applied to all the four sides of the substrate as well as the bottom surface to minimize the reflection at the edges.

The geometry dimensions of the simulated acoustofluidic chip were defined based on the optimum values calculated in the last chapter. These parameters are listed in Table 5-1. However, the aperture length and the tilt angle cannot be studied in the 2D simulation due to the nonuniformity of the AP distribution and the inevitable role of the third dimension. Herein, the aperture length

and the tilt angle are an investigation by the parametric study. The studied values are provided in Table 5-1 in the cases. In essence, the device characteristics must be optimized in a way the drag force is dominated over ARF to maximize the separation efficiency.

Table 5-1. Dimensions of the simulated acoustofluidic chip. The parameters shown in bold are varied for the parametric study and the rest were constant in the simulation

	Parameter name	**Symbol**	**Value**
Interdigital Transducer (IDT)	Pitch = Lambda	$p = \lambda_{SAW}$	150 [μm]
	Width of fingers	$d = \lambda_{SAW}/4$	37.5 [μm]
	Aperture length	$\boldsymbol{A}$	$\begin{cases}\mathbf{5}\\ \mathbf{10}\\ \mathbf{15}\end{cases}$ [$\boldsymbol{mm}$]
	Number of IDT fingers	N_P	21
	Length of delay	L_D	5 [mm]
Microchannel	Width	W	800 [μm]
	Height	H	100 [μm]
	Tilt angle	$\boldsymbol{\theta}$	$\begin{cases}\mathbf{5}\\ \mathbf{10}\\ \mathbf{15}\\ \mathbf{20}\\ \mathbf{30}\\ \mathbf{45}\end{cases}$ [$\boldsymbol{Deg}$]
Substrate (LiNbO3)	Width	w	15 [mm]
	Height	h	16 [mm]
	Depth	l	0.5 [mm]

One of the primary reasons for the lack of a detailed theoretical understanding of the physical processes involved in SAW devices is the difficulty in the identification of proper boundary conditions. To save computation time and resources, the acoustic impedance boundary condition was employed in the numerical simulation. All relevant material parameters are listed in Table 5-2. As most of the relevant physics is close to the top surface, the mesh element size was fixed to the minimum element size ($\frac{1}{6}\lambda_{SAW}$) at this surface and progressively increased as getting closer to the bottom surface (up to the maximum element size ($\frac{1}{5}\lambda_{SAW}$)). As a result, computational resources are saved while accurate results were achieved by the FEA method.

Table 5-2. Material properties that are implemented in the numerical simulation (at temperature $T = 25°$) taken from the COMSOL Multiphysics® Material Library.

Domain	Parameter name	Symbol	Value
Lithium Niobate (YX 128°)	Mass Density	ρ_{LN}	4620 $[kg/m^3]$
	Sound Speed	c_{LN}	3994 $[m/s]$
Microchannel (DI water)	Mass Density	ρ_w	997 $[kg/m^3]$
	Sound Speed	c_w	1497 $[m/s]$
	Shear Viscosity	μ	0.89 $[mPa.s]$
	Bulk Viscosity	μ_B	2.47 $[mPa.s]$
PDMS	Mass Density	ρ_{PDMS}	920 $[kg/m^3]$
	Sound Speed	c_{PDMS}	1076.5 $[m/s]$
	Acoustic Impedance	$Z_{PDMS} = \rho_{PDMS} \times c_{PDMS}$	0.9903 $[MPa.s/m]$

5.2.2. Influence of the microchannel tilt angle on AP in tSSAW

At first, the tilt angle (θ) is investigated at the constant aperture length ($A = 10\ [mm]$). In order to find the best value of the tilt angle for the tSSAW-based acoustofluidic chip, the averaged value of the total displacement ($\epsilon_{total} = \sqrt[2]{u^2 + v^2}$) versus the tilt angle with an interval of 10° is calculated at the bottom surface area of the microchannel where it is in direct contact with $LiNbO_3$.

As can be seen from Figure 5-3, the highest value of the ϵ_{total} occurs where the $\theta = 0°$ (same as pSSAW case). This behavior agrees well with our previous study in the case of pSSAW as such devices always cause a higher amplitude of ϵ_{total} and *AP* in the microchannel compared to tSSAW at the same operating conditions. Figure 5-3 demonstrates as the tilt angle increases from $\theta = 0°$ (pSSAW) to 45°, ϵ_{total} decreases by almost ~10%. However, the range between $\theta = 5°$ to 10° provides the minimum reduction in ϵ_{total} value compared to $\theta = 0°$. Besides, there is a small drop in ϵ_{total} value in the higher tilt angles up to $\theta = 20°$. Nevertheless, ϵ_{total} experiences a sudden reduction from $\theta = 20°$ afterward.

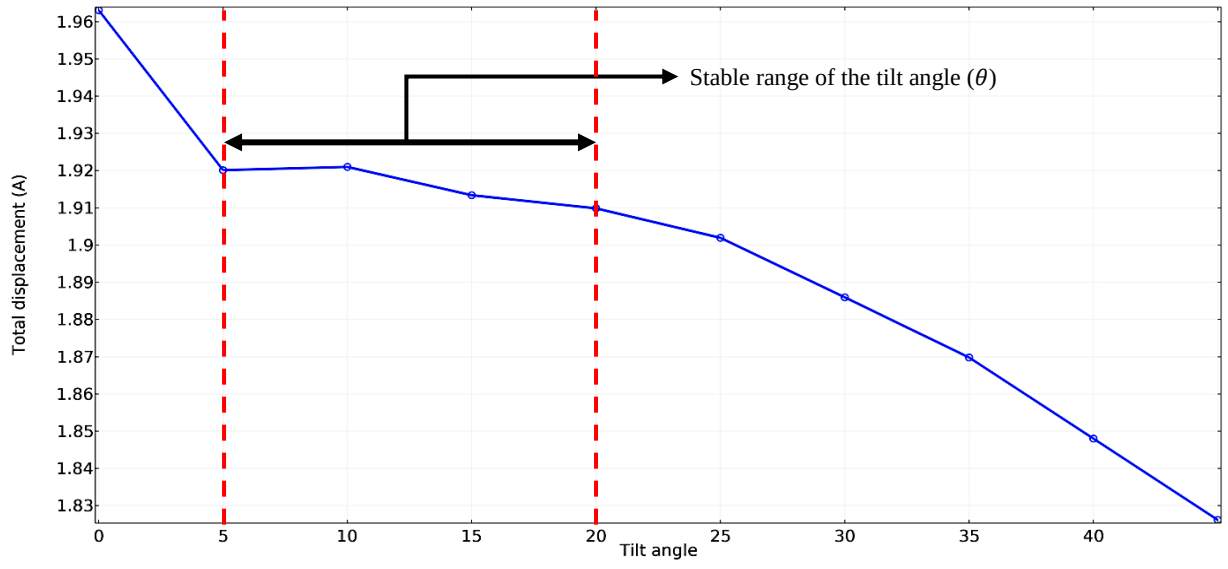

Figure 5-3. The averaged value of total displacement versus the tilted angle in the microchannel area at the constant aperture length.

The smaller tilt angles provide a fewer number of PNs and PANs compared to larger ones, which results in longer traveling times between PNs and PANs. However, the larger tilt angles decrease the chance of the microparticles migration to PNs as the overall resulting force tends to be parallel to the flow direction due to the drag force domination. Hence, the tilt angle between $5 \leq \theta \leq 15°$ is concluded to be the optimum value for the tilt angle.

5.2.3. Effects of IDT aperture length on acoustic pressure (AP) in tSSAW

Another parameter affecting the efficiency of the microparticle separation in tSSAW is the aperture length of IDTs. As SAW propagates through the piezoelectric substrate, the waves are diffracted, creating a near-field region of largely parallel wave-fronts known as the Fresnel region [92]. In practice, a larger aperture increases the time required for the longer lateral displacement of the microparticles. However, this behavior is only valid up to a specific length called an aperture cut-off length (A_c). The main reason for this phenomenon is the stored energy density in the piezoelectric substrate; if the aperture length is longer than the cut-off length ($A > A_c$), the energy density decreases in the substrate. Therefore, the optimum value of the IDT aperture length must be identified before fabrication.

Herein, after finding the optimum value for the tilt angle (here we used $\theta = 15°$), we modified our simulation to study the relationship between the total displacement at the surface of the piezoelectric and the aperture length at the same conditions of the previous section. The results indicate that any aperture length smaller than the microchannel length destruct the distribution of PNs and PANs. However, the aperture length with the same length of the microchannel provides a smooth distribution of the PNs and PANs except at the beginning and end of the microchannel. We observed that an aperture length of longer than the length of the microchannel provides the best distribution of the pressure acoustic compared to the smaller ones (see Table 5-3).

Table 5-3. The effects of the aperture length (A) on the distribution of the acoustic pressure in the microchannel at the constant tilt angle of $\theta = 15°$

$A = 3\ [mm]$	$A = 5\ [mm]$	$A = 7\ [mm]$
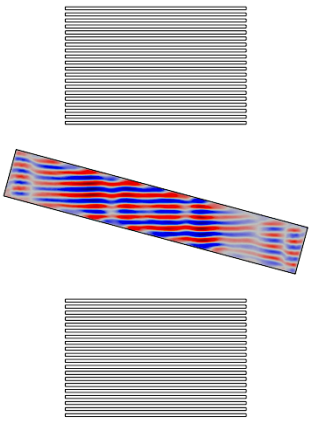	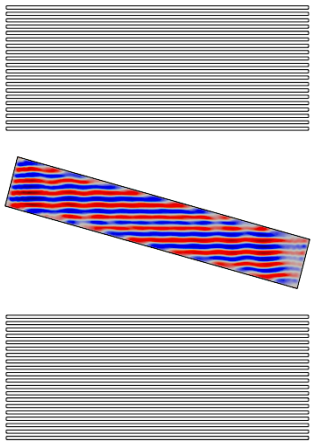	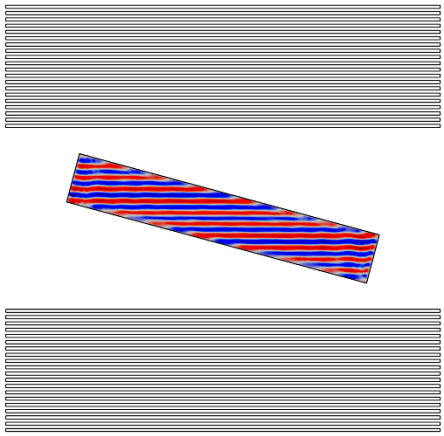
$A = 9\ [mm]$	$A = 11\ [mm]$	
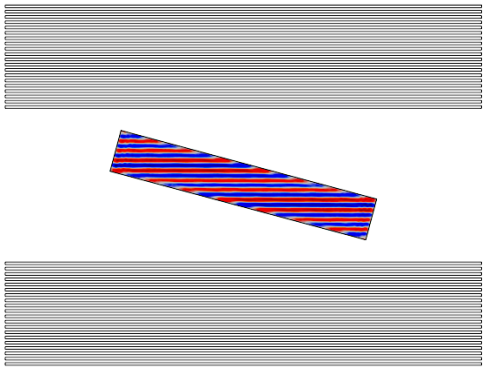	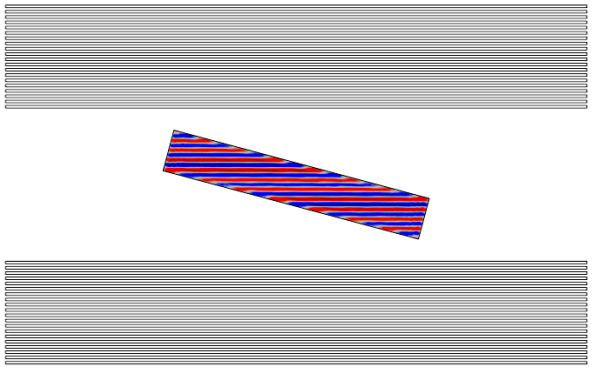	

Next, the averaged value of ϵ_{total} versus A (the aperture length) at different microchannel lengths was calculated at the bottom surface area. These results are shown in Figure 5-4 demonstrating that any aperture lengths longer than the microchannel length provide a stable ϵ_{total} value. This result indicates that there is a direct correlation between the microchannel length and the aperture length. Additionally, all of the parametric studies demonstrate that the total displacement reaches

a saturated value when the aperture length matches the microchannel length; beyond such a length no changes were observed.

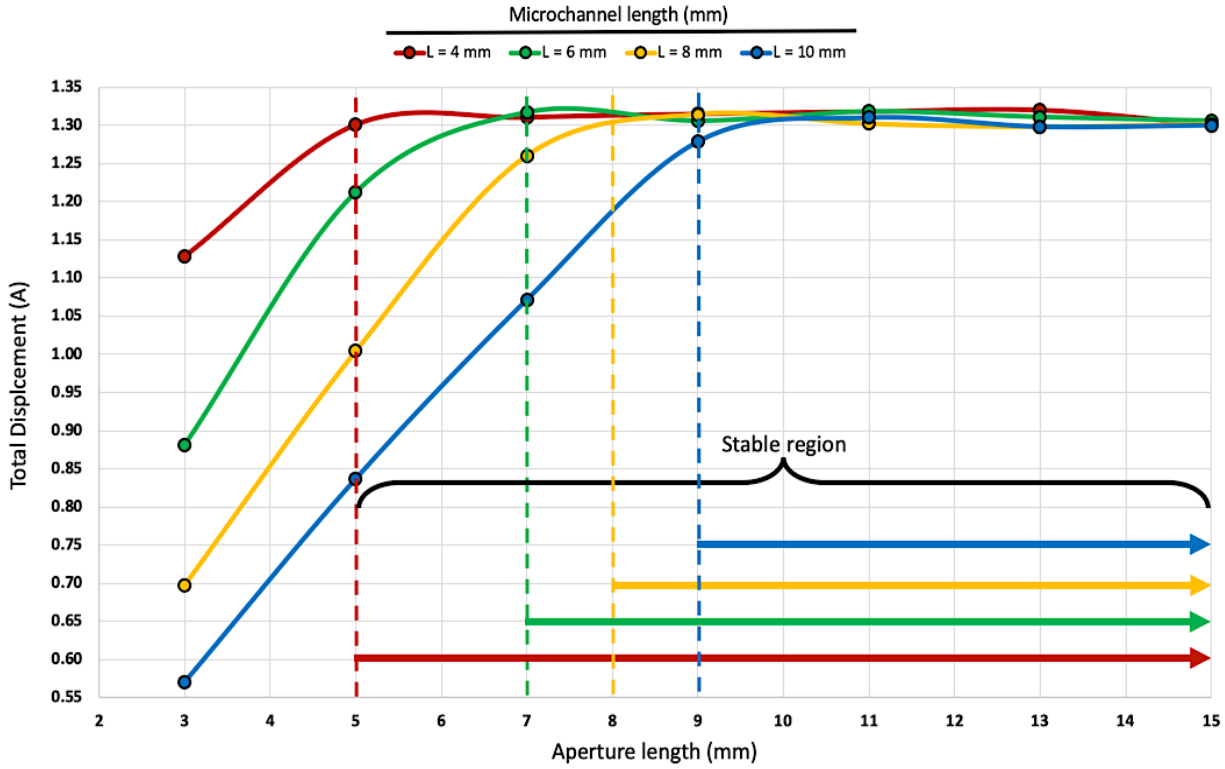

Figure 5-4. The averaged value of the total displacement versus the aperture length at the constant tilt angle of $\theta = 15°$

Most researchers [157] have used a dimensionless parameter called Fresnel parameter (F) to design the IDTs with minimum diffraction losses. The Fresnel parameter (F) is defined as $F = 4\lambda_{SAW}\mathrm{D}_F/\mathrm{A}^2$ where A and D_F are the aperture length and the distance between two pairs of IDT edges (the delay line), respectively. For each design of IDTs, F should be less than 1 ($F < 1$) to minimize the diffraction losses. Herein, we developed a MATLAB code to investigate the acceptable region for F at the various wavelengths (see Appendix B showing the details for the code). In this code, the delay line was assumed to be $\mathrm{D}_F = 2\ [cm]$. Figure 5-5 illustrates that as the wavelength increases, the required minimum value of the aperture length providing the

condition of $F < 1$ increases accordingly. Thus, the aperture lengths of $A = 1.4\ mm$ and 3.5 mm are required for the wavelengths of $\lambda_{SAW} = 50\ \mu m$ and $300\ \mu m$, respectively.

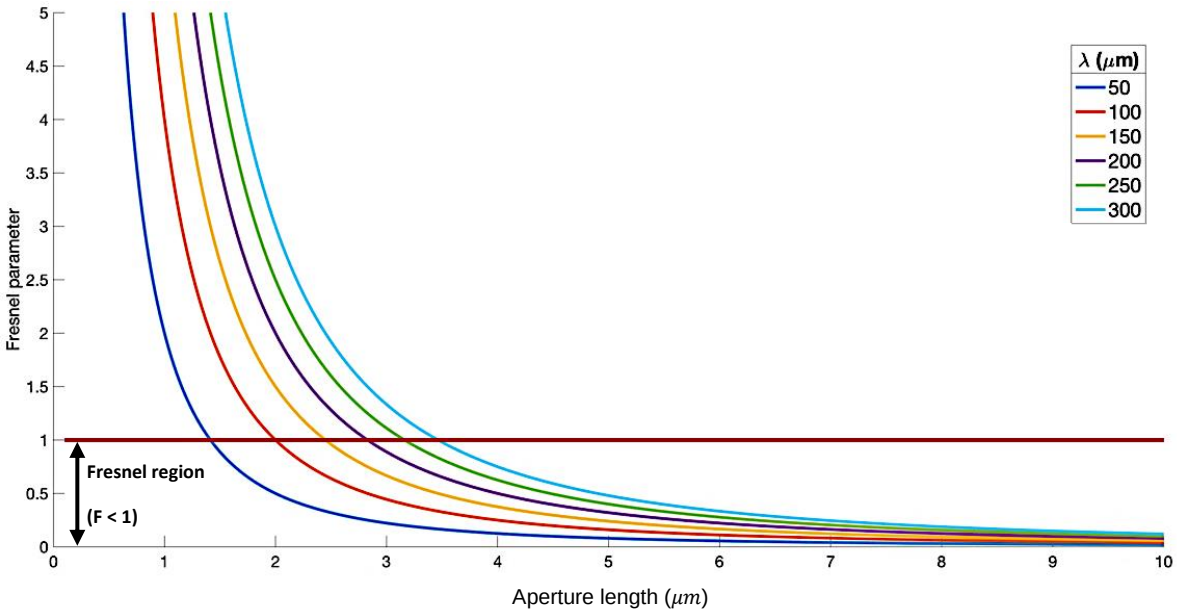

Figure 5-5. The Fresnel parameter (F) versus the aperture length (A) at different wavelengths.

5.3 Experimental results

The same microfabrication procedures and experimental setups explained in Chapter 3, were used for the tSSAW device. The PS microparticles with various sizes were used. Furthermore, the same operating conditions and equipment were used unless specified. The tSSAW device geometrical parameters were modified based on the outcomes of the numerical simulation. Herein, the aperture length and tilt angle were set to $A = 10\ [mm]$ and $\theta = 15$, respectively. The rest of the device characteristics were employed as listed in Table 5-1.

5.3.1. Separation of PS microparticles

To perform the separation of different PS microparticles, different particles ($20\ \mu m$, $15\ \mu m$, and $0.6\ \mu m$) were mixed homogeneously before infusing to the microchannel. Two syringe pumps

were used; one for the sample flow and another one for the sheath flow. The sheath flow was used for an initial focusing of the sample flow at one sidewall of the microchannel. This is a prerequisite step of the most microfluidic separation methods [1], [81], [158]. This method of focusing works based on a hydrodynamic force and the amount of the flow rates of these two flows, determining which of flow dominants another one. This splits the microchannel into two flow streams starting from an inlet junction. Once the PS microparticles enter the acoustic field region, they are deflected by ARF causing them to migrate from the sample flow to the sheath flow.

Herein, two factors play important roles in the separation efficiency: 1) the applied voltage to IDTs which affects the ARF magnitude, and 2) the flow rate which affects the drag force magnitude in both sheath and sample flow streams. Different sets of experiments with various applied voltages (input power) and the flow rates were conducted in order to examine the influence of these operational conditions on the efficiency of the separating of $0.6\ \mu m$ PS microparticles from $20\ \mu m$ and $15\ \mu m$ PS microparticles. These operational conditions along with the resulting separating efficiencies are shown in Figure 5-6. The separation efficiency is calculated as follows [116]:

$$Separation\ efficiency = \frac{Number\ of\ large\ microparticles\ in\ the\ target\ region}{Total\ number\ of\ presented\ large\ microparticles} \qquad (5.1)$$

In the above equation, the target region is defined as the bottom outlet channel in the experimental chip. Upon recording the videos (using the iPad Pro camera mounted on ECHO microscope; for more information refer to Section *3.6.*), a microparticle motion tracking software package

(Blender; version 2.80, www.blender.org) was used to track individually the paths of different sizes of the PS microparticles. Motion tracking was performed in the outlet regions of the microchannel containing two outlet channels called the top and bottom outlets here. As an example, Figure 5-6 demonstrates the positions of PS microparticles in a downstream side of the microchannel when the flow rate and the applied voltage are $Q = 5\ [\mu L/min]$ and $V_0 = 15\ [V]$, respectively. To ensure the reproducibility of these trajectories, they were calculated multiple times for different sizes of the microparticles.

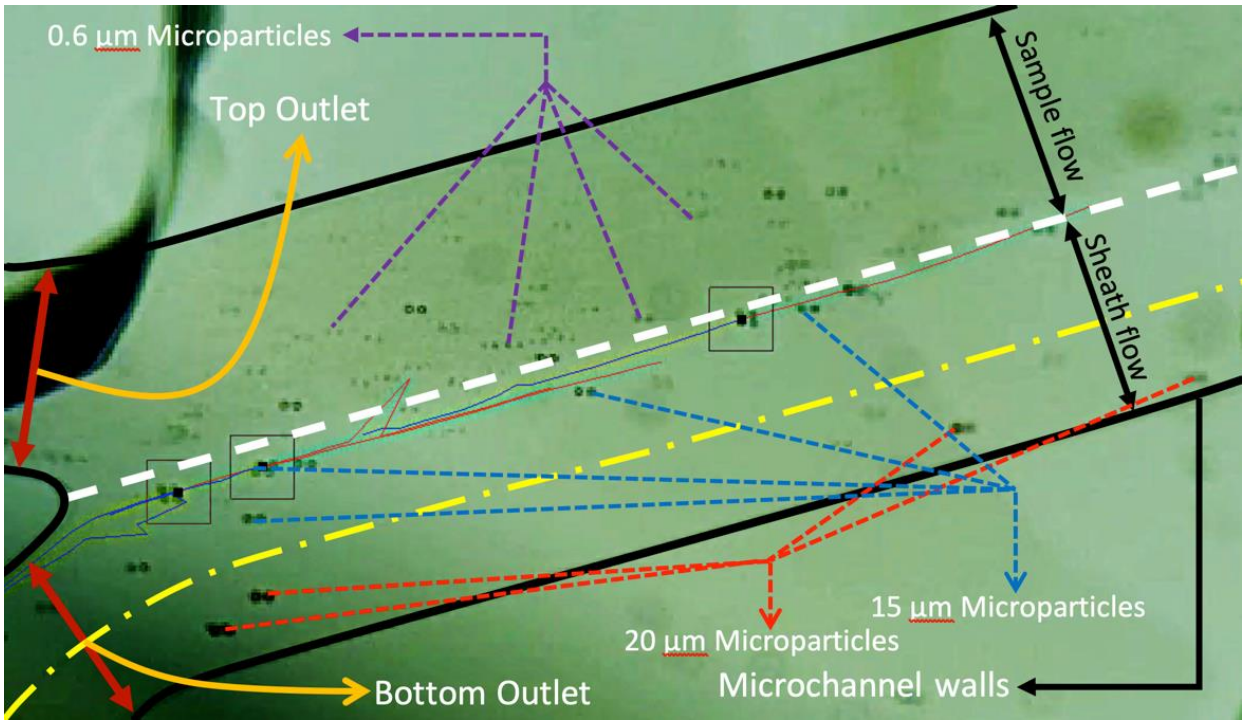

Figure 5-6. Downstream region of the microchannel showing the top and the bottom outlets. The pathways of the 20 µm and 15 µm microparticles represented by blue and red colored lines.

The separation efficiency was next calculated (Eq. (5.1)) at different operating conditions. As shown in Figure 5-6, the competition between ARF and the drag force influences the separation efficiency significantly. At each applied voltage, there is a threshold value for the flow rate (Q_c) below which a substantial reduction occurs in the separation efficiency. The results show when the flow rate is $Q = 1\ [\mu L/min]$, the majority of the applied voltages work perfectly. However,

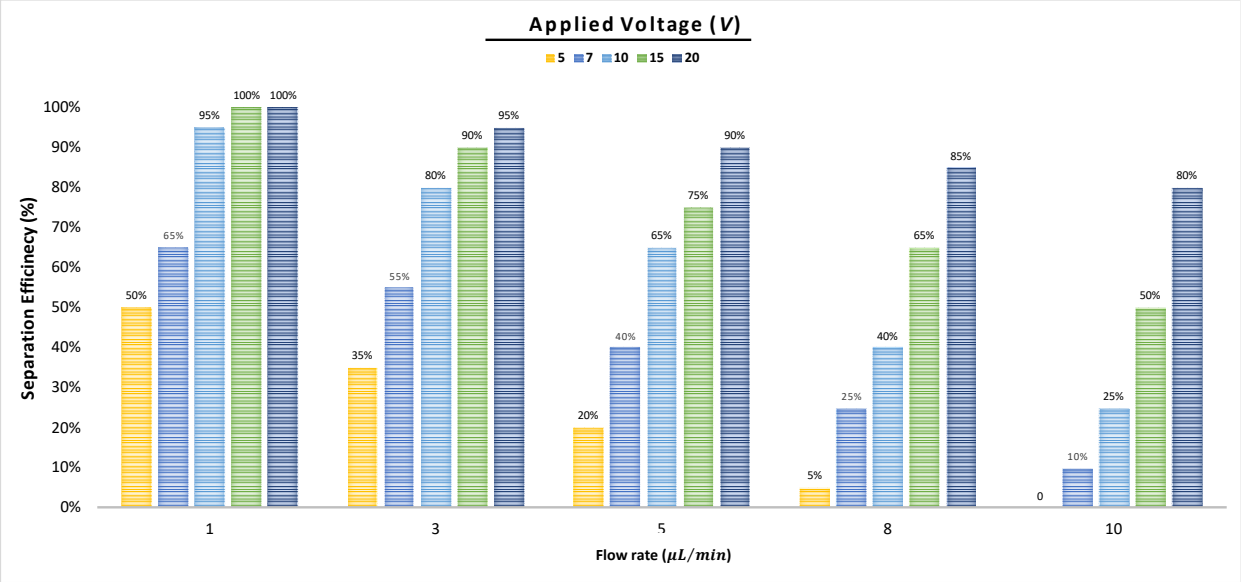

Figure 5-7. The separation efficiency of 0.6 µm PS microparticles from 15 µm and 20 µm PS microparticles at the different flow rates and applied voltages.

by increasing the flow rate to $Q = 10\,[\mu L/min]$, the efficiency decreases by 50% (on average). When the applied voltage is fixed at $V_0 = 20\,[V]$, the majority of the PS microparticles are deflected leading to higher separation efficiency. Nevertheless, the high voltages increase the chance of electrolysis caused by joule heating. This circumstance mostly happens when a high voltage is in direct contact with the fluid. Based on our experiments, we figured out that the $V_0 = 20\,[V]$ does not provide a stable separation for a long period of time due to Joule heating. Herein, the most stable operating condition happens when the applied voltage was set to V_0 =15 [V] which could provide an acceptable high separation efficiency (more than 65%) without the chance of joule heating. Next, the most suitable flow rate presenting high efficiency must be selected. Based on our observation, any flow rates below $Q_c = 8\,[\mu L/min]$ maintain the separation efficiency in. the acceptable range (upper than 65%).

5.3.2. Analysis of PS microparticles separation efficiency

Finally, the microparticle trajectories were investigated by extracting the microparticles tracking markers to a CSV file using a Python script provided on the GitHub website [159]. The extracted positions (*X* and *Y* locations) of the markers were inserted to Microsoft® Excel software (Version 2019, www.microsoft.com) for further analysis. Next, the markers' location values were rotated

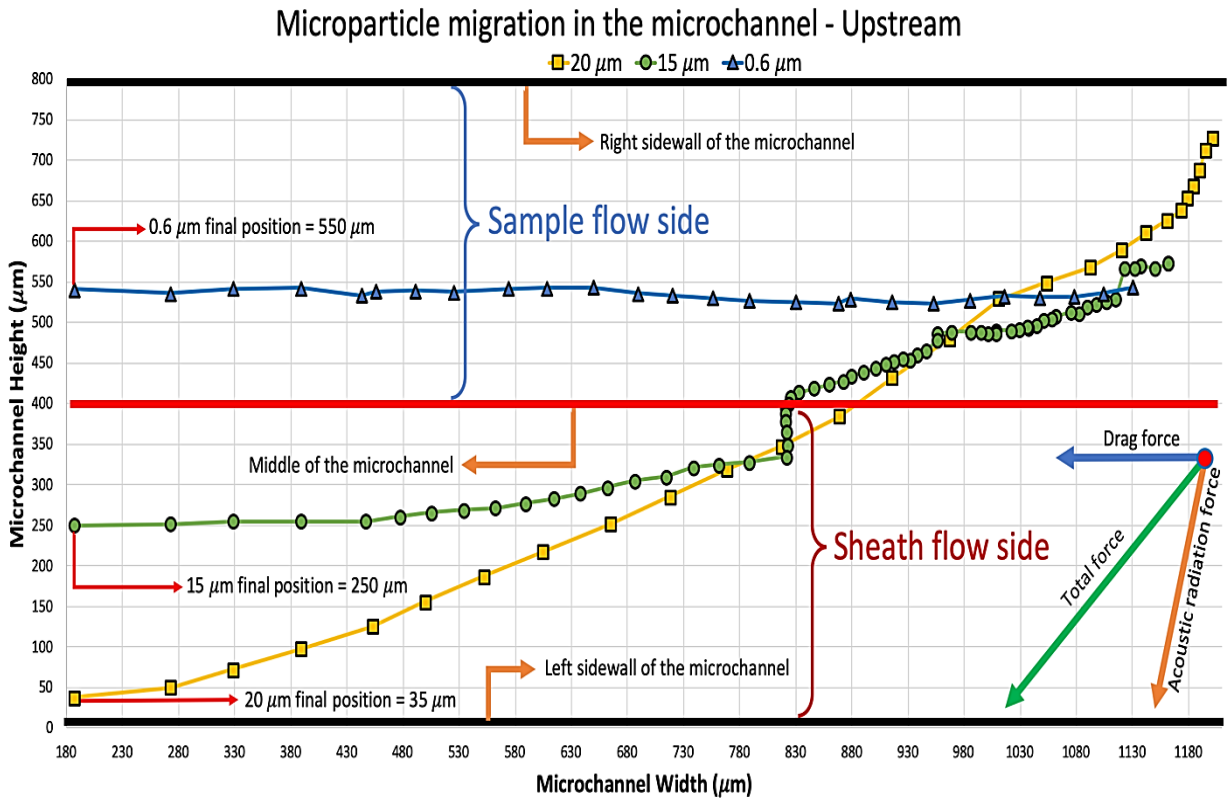

Figure 5-8. The migration path lines of the different sizes of the microparticles in the upstream region of the microchannel while the ARF and drag force present.

based on the rotation matrix formula. This step was necessary as the microchannel length direction was tilted by ~16° respect to the horizontal direction in the recorded microscope videos. Upon calculating the transformed values of the markers' locations, a scale factor was multiplied to them to change the unit of the values from pixels to the micrometer. The results of the microparticle trajectories in the upstream region are shown in Figure 5-8. As it is indicated, the 20 μm and

$15\ \mu m$ PS microparticles enter the sheath flow after moving $350\ \mu m$ along the length and ~$400\ \mu m$ across the width of the microchannel, respectively. After moving $850\ \mu m$ further along the length of the microchannel, $20\ \mu m$ and $15\ \mu m$ PS microparticles are located at the opposite sidewall of the microchannel. The $20\ \mu m$ and $15\ \mu m$ PS microparticles vertical positions are $35\ \mu m$ and $250\ \mu m$ with respect to the bottom sidewall, such that the distance between them is around $200\ \mu m$. In contrast, the $0.6\ \mu m$ PS microparticles are positioned $150\ \mu m$ above the middle of the microchannel without entering the sheath flow. This result demonstrates that the $0.6\ \mu m$ PS microparticles are not affected by ARF compared to the $20\ \mu m$ and $15\ \mu m$ PS microparticles. This agrees well with Eq. (5.1). Besides, the $20\ \mu m$ PS microparticles pass through the middle surface of the microchannel and enter the sheath flow without any restriction while the $15\ \mu m$ PS microparticles show a different trend when exiting the sample flow. As it can be seen from Figure 5-9, the $15\ \mu m$ PS microparticles follows a vertical path as soon as entering the sheath flow. However, the drag force caused by the sheath flow does not allow them to cross the microchannel width and push them along the length of the microchannel. The competition between ARF and the drag force determine the final positions of $20\ \mu m$ and $15\ \mu m$ PS microparticles in the sheath flow. The order of the drag force and ARF vary based on the microparticle's diameter. Due to that, $20\ \mu m$ and $15\ \mu m$ PS microparticles followed the different slope while moving toward the sheath flow. However, their slopes cannot be more than $15°$ which is the tilt angle of the microchannel.

The same approach was followed for the downstream region of the microchannel. Figure 5-9 demonstrates the $20\ \mu m$ and $15\ \mu m$ PS microparticles trajectories in the sheath side and the outlet microchannel. As illustrated, their vertical positions remained almost the same as the upstream region ($250\ \mu m$) until they exit the main microchannel. The reason for this observation is the

laminar flow regime leading to straight movement of the microparticles along the flow stream. Additionally, a sufficient aperture length (A) must be employed in the acoustofluidic chip (in essence, a very long aperture length causes all microparticles to reach another sidewall of the microchannel regardless of their sizes).

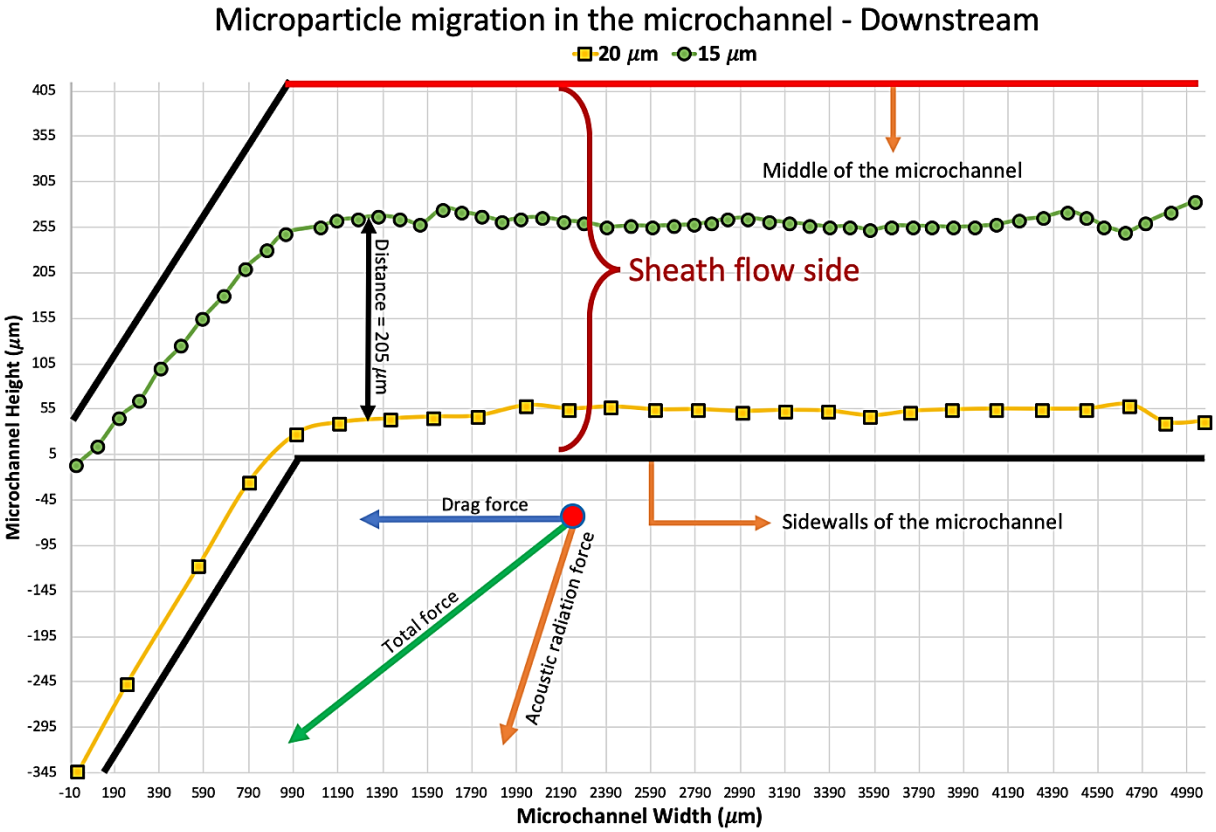

Figure 5-9. The migration path lines of the 20 μm and 15 μm PS microparticles in the downstream region of the microchannel in the presence of ARF and the drag force.

Chapter 6: Summary, contributions and future works

6.1 Summary

One of the goals of this study was to demonstrate the capability of the acoustofluidic chip a highly precise and fast-acting platform for manipulation and separation of microparticles. To achieve this goal, various steps were taken into account including carrying out the parameter optimization, developing the 2D and 3D numerical simulation, and conducting experiments. As a first step, the proposed lab-on-a-chip acoustofluidic chip was studied parametrically by the FEM method. This step was necessary to gain an insight into the phenomena occurring in the chip. The optimum values of the parameters were derived by the numerical simulation. In the next step, these optimized parameters were implemented in our designs to validate the outcomes of the numerical simulation with the experimental tests.

The simulation results indicated that the applied voltage and the number of IDT fingers play an important role in the efficiency of the acoustofluidic chip. As expected, there is a direct correlation between ARF and the applied voltage. Furthermore, the need for precise alignment has been shown: a small shift in the microchannel location can disturb the morphology of ARF in the fluid completely. Thus, as the first step, we designed the parallel SSAW (pSSAW) to examine the role of different key parameters. Both experimental and numerical simulations demonstrated that the number of IDT fingers (N_p) and the applied voltage (V_0) play the most important roles in increasing separation efficiency. However, there is a threshold for the applied voltage due to the joule heating phenomenon. According to the results, $V_0 = 15.0\ [V]$ is the maximum value of the applied voltage that should be supplied to the chip to ensure stable tests. Additionally, it was shown numerically

that only $N_p = \{20, 50, 80\}$ provide the highest energy transfer and a small variation from the optimum N_p would cause a substantial reduction in ARF.

To reduce the impact of misalignment, the tilted SSAW (tSSAW) method was studied numerically and experimentally. As the concept of tSSAW occurs in a 3D medium and it is not symmetrical in any directions, the 3D simulation was developed. However, the optimized parameter values which had been calculated in the pSSAW previously were employed in the tSSAW to minimize repetition in both numerical and experimental tests. The outcomes of the 3D simulation of tSSAW indicated that the optimum values of the microchannel tilt angle and the aperture length must be between $5 \leq \theta \leq 15°$ and the same as the microchannel length, respectively. Those derived optimum values were considered for the tSSAW chip design. The results demonstrated the high capability of tSSAW in the microparticles deflection and hence its power for label-free separation.

6.2 Limitation and future works

- The proposed acoustofluidic chip has proven its capability in the manipulation and separation of synthetic (PS) microparticles. For future studies, a similar study must be repeated with the bioparticles as there is a slight variation in some of their physical properties (such as compressibility) as compared to PS particles.
- The 3D numerical simulation can be extended to cover both parametric study and particle tracing together.
- The throughput of the acoustofluidic chip should be studied by minimizing energy losses.
- A multi-functional acoustofluidic chip can be developed by combining on-chip detection with separation.

- An acoustofluidic chip can be combined by immunoaffinity-based methods to detect a highly specific type of EVs.

6.3 Contributions

1) A comprehensive numerical simulation was developed to investigate the effect of different parameters including device characteristics and operating conditions on the microparticles manipulation and the separation efficiency. The model was used to (i) obtain optimum values for different components of the acoustofluidic chip, and (ii) identify optimum operational conditions. This model can be used for various applications besides the separation and manipulation purposes as it covers all the necessary governing equations.
2) The experimental setup was prepared for conducting tests on the fabricated acoustofluidic chips based on the optimum device characteristic parameters. The experimental results were analyzed with image processing techniques and the particle tracking processor software to compare the chip efficiency at different operational conditions.

Bibliography

[1] X. Li *et al.*, “Challenges and opportunities in exosome research—Perspectives from biology, engineering, and cancer therapy,” *APL Bioeng.*, vol. 3, no. 1, p. 011503, 2019.

[2] C. Théry, L. Zitvogel, and S. Amigorena, “Exosomes: composition, biogenesis and function,” *Nat. Rev. Immunol.*, vol. 2, no. 8, p. 569, 2002.

[3] J. C. Contreras-Naranjo, H.-J. Wu, and V. M. Ugaz, “Microfluidics for exosome isolation and analysis: enabling liquid biopsy for personalized medicine,” *Lab. Chip*, vol. 17, no. 21, pp. 3558–3577, 2017.

[4] P. A. Gonzales *et al.*, “Large-scale proteomics and phosphoproteomics of urinary exosomes,” *J. Am. Soc. Nephrol.*, vol. 20, no. 2, pp. 363–379, 2009.

[5] C. Lässer *et al.*, “Human saliva, plasma and breast milk exosomes contain RNA: uptake by macrophages,” *J. Transl. Med.*, vol. 9, no. 1, p. 9, 2011.

[6] M. Wu *et al.*, “Isolation of exosomes from whole blood by integrating acoustics and microfluidics,” *Proc. Natl. Acad. Sci.*, p. 201709210, 2017.

[7] H.-K. Woo *et al.*, “Exodisc for rapid, size-selective, and efficient isolation and analysis of nanoscale extracellular vesicles from biological samples,” *ACS Nano*, vol. 11, no. 2, pp. 1360–1370, 2017.

[8] S. E. Andaloussi, I. Mäger, X. O. Breakefield, and M. J. Wood, “Extracellular vesicles: biology and emerging therapeutic opportunities,” *Nat. Rev. Drug Discov.*, vol. 12, no. 5, p. 347, 2013.

[9] A. V. Vlassov, S. Magdaleno, R. Setterquist, and R. Conrad, “Exosomes: current knowledge of their composition, biological functions, and diagnostic and therapeutic potentials,” *Biochim. Biophys. Acta BBA-Gen. Subj.*, vol. 1820, no. 7, pp. 940–948, 2012.

[10] C. Théry, M. Ostrowski, and E. Segura, “Membrane vesicles as conveyors of immune responses,” *Nat. Rev. Immunol.*, vol. 9, no. 8, p. 581, 2009.

[11] J. Skog *et al.*, “Glioblastoma microvesicles transport RNA and proteins that promote tumour growth and provide diagnostic biomarkers,” *Nat. Cell Biol.*, vol. 10, no. 12, p. 1470, 2008.

[12] L. Balaj *et al.*, “Tumour microvesicles contain retrotransposon elements and amplified oncogene sequences,” *Nat. Commun.*, vol. 2, p. 180, 2011.

[13] H. Valadi, K. Ekström, A. Bossios, M. Sjöstrand, J. J. Lee, and J. O. Lötvall, "Exosome-mediated transfer of mRNAs and microRNAs is a novel mechanism of genetic exchange between cells," *Nat. Cell Biol.*, vol. 9, no. 6, p. 654, 2007.

[14] J. H. Ellwanger, T. D. Veit, and J. A. B. Chies, "Exosomes in HIV infection: A review and critical look," *Infect. Genet. Evol.*, vol. 53, pp. 146–154, 2017.

[15] B. K. Thakur *et al.*, "Double-stranded DNA in exosomes: a novel biomarker in cancer detection," *Cell Res.*, vol. 24, no. 6, p. 766, 2014.

[16] E. Zeringer, T. Barta, M. Li, and A. V. Vlassov, "Strategies for isolation of exosomes," *Cold Spring Harb. Protoc.*, vol. 2015, no. 4, p. pdb-top074476, 2015.

[17] M. Logozzi *et al.*, "High levels of exosomes expressing CD63 and caveolin-1 in plasma of melanoma patients," *PloS One*, vol. 4, no. 4, p. e5219, 2009.

[18] T. Kogure, I. K. Yan, W.-L. Lin, and T. Patel, "Extracellular vesicle–mediated transfer of a novel long noncoding RNA TUC339: a mechanism of intercellular signaling in human hepatocellular cancer," *Genes Cancer*, vol. 4, no. 7–8, pp. 261–272, 2013.

[19] F. Cappello *et al.*, "Exosome levels in human body fluids: a tumor marker by themselves?," *Eur. J. Pharm. Sci.*, vol. 96, pp. 93–98, 2017.

[20] S. Gholizadeh *et al.*, "Microfluidic approaches for isolation, detection, and characterization of extracellular vesicles: current status and future directions," *Biosens. Bioelectron.*, vol. 91, pp. 588–605, 2017.

[21] K. B. Johnsen, J. M. Gudbergsson, M. N. Skov, L. Pilgaard, T. Moos, and M. Duroux, "A comprehensive overview of exosomes as drug delivery vehicles—endogenous nanocarriers for targeted cancer therapy," *Biochim. Biophys. Acta BBA-Rev. Cancer*, vol. 1846, no. 1, pp. 75–87, 2014.

[22] A. Sharma, Z. Khatun, and A. Shiras, "Tumor exosomes: cellular postmen of cancer diagnosis and personalized therapy," *Nanomed.*, vol. 11, no. 4, pp. 421–437, 2016.

[23] F. Properzi, M. Logozzi, and S. Fais, "Exosomes: the future of biomarkers in medicine," *Biomark. Med.*, vol. 7, no. 5, pp. 769–778, 2013.

[24] C. Lawson, J. M. Vicencio, D. M. Yellon, and S. M. Davidson, "Microvesicles and exosomes: new players in metabolic and cardiovascular disease," *J. Endocrinol.*, vol. 228, no. 2, pp. R57–R71, 2016.

[25] M. J. Saeedi Borujeni, E. Esfandiary, G. Taheripak, P. Codoñer-Franch, E. Alonso-Iglesias, and H. Mirzaei, “Molecular aspects of diabetes mellitus: Resistin, microRNA, and exosome,” *J. Cell. Biochem.*, vol. 119, no. 2, pp. 1257–1272, 2018.

[26] T. Xiao, W. Zhang, B. Jiao, C.-Z. Pan, X. Liu, and L. Shen, “The role of exosomes in the pathogenesis of Alzheimer’disease,” *Transl. Neurodegener.*, vol. 6, no. 1, p. 3, 2017.

[27] T. Malm, S. Loppi, and K. M. Kanninen, “Exosomes in Alzheimer’s disease,” *Neurochem. Int.*, vol. 97, pp. 193–199, 2016.

[28] K. Yuyama and Y. Igarashi, “Exosomes as Carriers of Alzheimer’s Amyloid-ß,” *Front. Neurosci.*, vol. 11, p. 229, 2017.

[29] X. Wu, T. Zheng, and B. Zhang, “Exosomes in Parkinson’s disease,” *Neurosci. Bull.*, vol. 33, no. 3, pp. 331–338, 2017.

[30] G. K. Tofaris, “A Critical Assessment of Exosomes in the Pathogenesis and Stratification of Parkinson’s Disease,” *J. Park. Dis.*, vol. 7, no. 4, pp. 569–576, 2017.

[31] P. B. Devhare, R. Sasaki, S. Shrivastava, A. M. Di Bisceglie, R. Ray, and R. B. Ray, “Exosome-mediated intercellular communication between hepatitis C virus-infected hepatocytes and hepatic stellate cells,” *J. Virol.*, vol. 91, no. 6, pp. e02225-16, 2017.

[32] T. N. Bukong, F. Momen-Heravi, K. Kodys, S. Bala, and G. Szabo, “Exosomes from hepatitis C infected patients transmit HCV infection and contain replication competent viral RNA in complex with Ago2-miR122-HSP90,” *PLoS Pathog.*, vol. 10, no. 10, p. e1004424, 2014.

[33] B. W. Van Balkom, T. Pisitkun, M. C. Verhaar, and M. A. Knepper, “Exosomes and the kidney: prospects for diagnosis and therapy of renal diseases,” *Kidney Int.*, vol. 80, no. 11, pp. 1138–1145, 2011.

[34] C. Grange, C. Iampietro, and B. Bussolati, “Stem cell extracellular vesicles and kidney injury,” *Stem Cell Investig.*, vol. 4, 2017.

[35] M. L. Alvarez, M. Khosroheidari, R. K. Ravi, and J. K. DiStefano, “Comparison of protein, microRNA, and mRNA yields using different methods of urinary exosome isolation for the discovery of kidney disease biomarkers,” *Kidney Int.*, vol. 82, no. 9, pp. 1024–1032, 2012.

[36] T. B. Steinbichler, J. Dudás, H. Riechelmann, and I.-I. Skvortsova, “The role of exosomes in cancer metastasis,” presented at the Seminars in cancer biology, 2017, vol. 44, pp. 170–181.

[37] Y. H. Soung, S. Ford, V. Zhang, and J. Chung, “Exosomes in cancer diagnostics,” *Cancers*, vol. 9, no. 1, p. 8, 2017.

[38] X. Zhang, X. Yuan, H. Shi, L. Wu, H. Qian, and W. Xu, “Exosomes in cancer: small particle, big player,” *J. Hematol. Oncol.J Hematol Oncol*, vol. 8, no. 1, p. 83, 2015.

[39] W. Guo *et al.*, “Exosomes: New players in cancer,” *Oncol. Rep.*, vol. 38, no. 2, pp. 665–675, 2017.

[40] S. Halvaei *et al.*, “Exosomes in cancer liquid biopsy: a focus on breast cancer,” *Mol. Ther.-Nucleic Acids*, 2017.

[41] W. Sun, J. Luo, H. Jiang, and D. D. Duan, “Tumor exosomes: a double-edged sword in cancer therapy,” *Acta Pharmacol. Sin.*, 2018.

[42] N. Chaput and C. Théry, “Exosomes: immune properties and potential clinical implementations,” presented at the Seminars in immunopathology, 2011, vol. 33, pp. 419–440.

[43] M. Colombo, G. Raposo, and C. Théry, “Biogenesis, secretion, and intercellular interactions of exosomes and other extracellular vesicles,” *Annu. Rev. Cell Dev. Biol.*, vol. 30, pp. 255–289, 2014.

[44] P. D. Robbins, A. Dorronsoro, and C. N. Booker, “Regulation of chronic inflammatory and immune processes by extracellular vesicles,” *J. Clin. Invest.*, vol. 126, no. 4, pp. 1173–1180, 2016.

[45] F. M. Kashkooli, M. Soltani, M. Rezaeian, E. Taatizadeh, and M.-H. Hamedi, “Image-based spatio-temporal model of drug delivery in a heterogeneous vasculature of a solid tumor—Computational approach,” *Microvasc. Res.*, 2019.

[46] Y. Yuana, J. Levels, A. Grootemaat, A. Sturk, and R. Nieuwland, “Co-isolation of extracellular vesicles and high-density lipoproteins using density gradient ultracentrifugation,” *J. Extracell. Vesicles*, vol. 3, no. 1, p. 23262, 2014.

[47] J. Caradec, G. Kharmate, E. Hosseini-Beheshti, H. Adomat, M. Gleave, and E. Guns, “Reproducibility and efficiency of serum-derived exosome extraction methods,” *Clin. Biochem.*, vol. 47, no. 13–14, pp. 1286–1292, 2014.

[48] A. Liga, A. Vliegenthart, W. Oosthuyzen, J. Dear, and M. Kersaudy-Kerhoas, “Exosome isolation: a microfluidic road-map,” *Lab. Chip*, vol. 15, no. 11, pp. 2388–2394, 2015.

[49] S. S. Kanwar, C. J. Dunlay, D. M. Simeone, and S. Nagrath, “Microfluidic device (ExoChip) for on-chip isolation, quantification and characterization of circulating exosomes,” *Lab. Chip*, vol. 14, no. 11, pp. 1891–1900, 2014.

[50] C. Chen *et al.*, “Microfluidic isolation and transcriptome analysis of serum microvesicles,” *Lab. Chip*, vol. 10, no. 4, pp. 505–511, 2010.

[51] S. Nahavandi *et al.*, “Microfluidic platforms for biomarker analysis,” *Lab. Chip*, vol. 14, no. 9, pp. 1496–1514, 2014.

[52] J. Rho *et al.*, “Magnetic nanosensor for detection and profiling of erythrocyte-derived microvesicles,” *ACS Nano*, vol. 7, no. 12, pp. 11227–11233, 2013.

[53] S. Gurunathan, M.-H. Kang, M. Jeyaraj, M. Qasim, and J.-H. Kim, “Review of the isolation, characterization, biological function, and multifarious therapeutic approaches of exosomes,” *Cells*, vol. 8, no. 4, p. 307, 2019.

[54] C. Théry, S. Amigorena, G. Raposo, and A. Clayton, “Isolation and characterization of exosomes from cell culture supernatants and biological fluids,” *Curr. Protoc. Cell Biol.*, pp. 3–22, 2006.

[55] B. J. Tauro *et al.*, “Comparison of ultracentrifugation, density gradient separation, and immunoaffinity capture methods for isolating human colon cancer cell line LIM1863-derived exosomes,” *Methods*, vol. 56, no. 2, pp. 293–304, 2012.

[56] N. Zarovni *et al.*, “Integrated isolation and quantitative analysis of exosome shuttled proteins and nucleic acids using immunocapture approaches,” *Methods*, vol. 87, pp. 46–58, 2015.

[57] A. Bobrie, M. Colombo, S. Krumeich, G. Raposo, and C. Théry, “Diverse subpopulations of vesicles secreted by different intracellular mechanisms are present in exosome preparations obtained by differential ultracentrifugation,” *J. Extracell. Vesicles*, vol. 1, no. 1, p. 18397, 2012.

[58] M. Li *et al.*, “An optimized procedure for exosome isolation and analysis using serum samples: Application to cancer biomarker discovery,” *Methods*, vol. 87, pp. 26–30, 2015.

[59] D. W. Greening, R. Xu, H. Ji, B. J. Tauro, and R. J. Simpson, “A protocol for exosome isolation and characterization: evaluation of ultracentrifugation, density-gradient separation, and immunoaffinity capture methods,” *Proteomic Profiling Methods Protoc.*, pp. 179–209, 2015.

[60] H. G. Lamparski *et al.*, “Production and characterization of clinical grade exosomes derived from dendritic cells,” *J. Immunol. Methods*, vol. 270, no. 2, pp. 211–226, 2002.

[61] K. W. Witwer *et al.*, “Standardization of sample collection, isolation and analysis methods in extracellular vesicle research,” *J. Extracell. Vesicles*, vol. 2, no. 1, p. 20360, 2013.

[62] J. Van Deun *et al.*, “The impact of disparate isolation methods for extracellular vesicles on downstream RNA profiling,” *J. Extracell. Vesicles*, vol. 3, no. 1, p. 24858, 2014.

[63] F. Yang, X. Liao, Y. Tian, and G. Li, “Exosome separation using microfluidic systems: size-based, immunoaffinity-based and dynamic methodologies,” *Biotechnol. J.*, 2017.

[64] R. Linares, S. Tan, C. Gounou, N. Arraud, and A. R. Brisson, “High-speed centrifugation induces aggregation of extracellular vesicles,” *J. Extracell. Vesicles*, vol. 4, no. 1, p. 29509, 2015.

[65] J. F. Quintana *et al.*, “Extracellular Onchocerca-derived small RNAs in host nodules and blood,” *Parasit. Vectors*, vol. 8, no. 1, p. 58, 2015.

[66] P. Li, M. Kaslan, S. H. Lee, J. Yao, and Z. Gao, “Progress in exosome isolation techniques,” *Theranostics*, vol. 7, no. 3, p. 789, 2017.

[67] D. Müller, S. Cattaneo, F. Meier, R. Welz, and A. J. deMello, “Nanoparticle separation with a miniaturized asymmetrical flow field-flow fractionation cartridge,” *Front. Chem.*, vol. 3, p. 45, 2015.

[68] L.-L. Yu *et al.*, “A Comparison of Traditional and Novel Methods for the Separation of Exosomes from Human Samples,” *BioMed Res. Int.*, vol. 2018, 2018.

[69] A. Cheruvanky *et al.*, “Rapid isolation of urinary exosomal biomarkers using a nanomembrane ultrafiltration concentrator,” *Am. J. Physiol.-Ren. Physiol.*, vol. 292, no. 5, pp. F1657–F1661, 2007.

[70] B. J. Tauro, D. W. Greening, R. A. Mathias, S. Mathivanan, H. Ji, and R. J. Simpson, “Two distinct populations of exosomes are released from LIM1863 colon carcinoma cell-derived organoids,” *Mol. Cell. Proteomics*, p. mcp-M112, 2012.

[71] E. Pariset, V. Agache, and A. Millet, “Extracellular Vesicles: Isolation Methods,” *Adv. Biosyst.*, 2017.

[72] F. Momen-Heravi *et al.*, “Current methods for the isolation of extracellular vesicles,” *Biol. Chem.*, vol. 394, no. 10, pp. 1253–1262, 2013.

[73] S. Li, F. Ma, H. Bachman, C. E. Cameron, X. Zeng, and T. J. Huang, “Acoustofluidic bacteria separation,” *J. Micromechanics Microengineering*, vol. 27, no. 1, p. 015031, 2016.

[74] R. Guldiken, M. C. Jo, N. D. Gallant, U. Demirci, and J. Zhe, “Sheathless size-based acoustic particle separation,” *Sensors*, vol. 12, no. 1, pp. 905–922, 2012.

[75] G. M. Whitesides, “The origins and the future of microfluidics,” *Nature*, vol. 442, no. 7101, p. 368, 2006.

[76] A. Dietzel, “A Brief Introduction to Microfluidics,” in *Microsystems for Pharmatechnology*, Springer, 2016, pp. 1–21.

[77] J. M. Ng, I. Gitlin, A. D. Stroock, and G. M. Whitesides, “Components for integrated poly (dimethylsiloxane) microfluidic systems,” *Electrophoresis*, vol. 23, no. 20, pp. 3461–3473, 2002.

[78] P. N. Nge, C. I. Rogers, and A. T. Woolley, “Advances in microfluidic materials, functions, integration, and applications,” *Chem. Rev.*, vol. 113, no. 4, pp. 2550–2583, 2013.

[79] S.-C. Guo, S.-C. Tao, and H. Dawn, “Microfluidics-based on-a-chip systems for isolating and analysing extracellular vesicles,” *J. Extracell. Vesicles*, vol. 7, no. 1, p. 1508271, 2018.

[80] T. Salafi, K. K. Zeming, and Y. Zhang, “Advancements in microfluidics for nanoparticle separation,” *Lab. Chip*, vol. 17, no. 1, pp. 11–33, 2017.

[81] A. Dalili, E. Samiei, and M. Hoorfar, “A review of sorting, separation and isolation of cells and microbeads for biomedical applications: microfluidic approaches,” *Analyst*, vol. 144, no. 1, pp. 87–113, 2019.

[82] R. T. Davies, J. Kim, S. C. Jang, E.-J. Choi, Y. S. Gho, and J. Park, “Microfluidic filtration system to isolate extracellular vesicles from blood,” *Lab. Chip*, vol. 12, no. 24, pp. 5202–5210, 2012.

[83] L.-G. Liang *et al.*, “An integrated double-filtration microfluidic device for isolation, enrichment and quantification of urinary extracellular vesicles for detection of bladder cancer,” *Sci. Rep.*, vol. 7, p. 46224, 2017.

[84] M. He, J. Crow, M. Roth, Y. Zeng, and A. K. Godwin, “Integrated immunoisolation and protein analysis of circulating exosomes using microfluidic technology,” *Lab. Chip*, vol. 14, no. 19, pp. 3773–3780, 2014.

[85] J. S. Dudani, D. R. Gossett, H. T. Tse, R. J. Lamm, R. P. Kulkarni, and D. D. Carlo, “Rapid inertial solution exchange for enrichment and flow cytometric detection of microvesicles,” *Biomicrofluidics*, vol. 9, no. 1, p. 014112, 2015.

[86] Z. Zhao, Y. Yang, Y. Zeng, and M. He, “A microfluidic ExoSearch chip for multiplexed exosome detection towards blood-based ovarian cancer diagnosis,” *Lab. Chip*, vol. 16, no. 3, pp. 489–496, 2016.

[87] J. C. Yeo, Kenry, Z. Zhao, P. Zhang, Z. Wang, and C. T. Lim, “Label-free extraction of extracellular vesicles using centrifugal microfluidics,” *Biomicrofluidics*, vol. 12, no. 2, p. 024103, 2018.

[88] B. H. Wunsch *et al.*, “Nanoscale lateral displacement arrays for the separation of exosomes and colloids down to 20 nm,” *Nat. Nanotechnol.*, vol. 11, no. 11, p. 936, 2016.

[89] C. Liu *et al.*, “Field-free isolation of exosomes from extracellular vesicles by microfluidic viscoelastic flows,” *ACS Nano*, vol. 11, no. 7, pp. 6968–6976, 2017.

[90] K. Lee, H. Shao, R. Weissleder, and H. Lee, “Acoustic purification of extracellular microvesicles,” *ACS Nano*, vol. 9, no. 3, pp. 2321–2327, 2015.

[91] A. Dalili, E. Taatizadeh, and M. Hoorfar, “Characterization of the electrodes of DEP-based micro-separator,” 2018.

[92] W. Connacher *et al.*, “Micro/nano acoustofluidics: materials, phenomena, design, devices, and applications,” *Lab. Chip*, 2018.

[93] X. Ding *et al.*, “Surface acoustic wave microfluidics,” *Lab. Chip*, vol. 13, no. 18, pp. 3626–3649, 2013.

[94] D. L. Miller *et al.*, “Overview of therapeutic ultrasound applications and safety considerations,” *J. Ultrasound Med.*, vol. 31, no. 4, pp. 623–634, 2012.

[95] M. C. Jo, “An Acoustic-based Microfluidic Platform for Active Separation and Mixing,” 2013.

[96] J. Friend and L. Y. Yeo, “Microscale acoustofluidics: Microfluidics driven via acoustics and ultrasonics,” *Rev Mod Phys*, vol. 83, no. 2, pp. 647–704, Jun. 2011.

[97] A. Arnau, *Piezoelectric transducers and applications*, vol. 2004. Springer, 2004.

[98] I. Leibacher, P. Reichert, and J. Dual, “Microfluidic droplet handling by bulk acoustic wave (BAW) acoustophoresis,” *Lab. Chip*, vol. 15, no. 13, pp. 2896–2905, 2015.

[99] K. Länge, B. E. Rapp, and M. Rapp, “Surface acoustic wave biosensors: a review,” *Anal. Bioanal. Chem.*, vol. 391, no. 5, pp. 1509–1519, 2008.

[100] M.-I. Rocha-Gaso, C. March-Iborra, Á. Montoya-Baides, and A. Arnau-Vives, “Surface generated acoustic wave biosensors for the detection of pathogens: A review,” *Sensors*, vol. 9, no. 7, pp. 5740–5769, 2009.

[101] J. C. Andle, J. F. Vetelino, M. W. Lade, and D. J. McAllister, “An acoustic plate mode biosensor,” *Sens. Actuators B Chem.*, vol. 8, no. 2, pp. 191–198, 1992.

[102] M. Gedge and M. Hill, “Theory of Surface Acoustic Wave Devices for Particle Manipulation,” in *Microscale Acoustofluidics*, Royal Society of Chemistry, 2014, pp. 337–353.

[103] G. Destgeer and H. J. Sung, “Recent advances in microfluidic actuation and micro-object manipulation via surface acoustic waves,” *Lab. Chip*, vol. 15, no. 13, pp. 2722–2738, 2015.

[104] Y. Ai, C. K. Sanders, and B. L. Marrone, “Separation of Escherichia coli bacteria from peripheral blood mononuclear cells using standing surface acoustic waves,” *Anal. Chem.*, vol. 85, no. 19, pp. 9126–9134, 2013.

[105] J. Shi, D. Ahmed, X. Mao, S.-C. S. Lin, A. Lawit, and T. J. Huang, “Acoustic tweezers: patterning cells and microparticles using standing surface acoustic waves (SSAW),” *Lab. Chip*, vol. 9, no. 20, pp. 2890–2895, 2009.

[106] M. Wu *et al.*, “Circulating Tumor Cell Phenotyping via High-Throughput Acoustic Separation,” *Small*, vol. 14, no. 32, p. 1801131, 2018.

[107] A. Ozcelik *et al.*, “Acoustic tweezers for the life sciences,” *Nat. Methods*, p. 1, 2018.

[108] Y. Chen *et al.*, “Continuous enrichment of low-abundance cell samples using standing surface acoustic waves (SSAW),” *Lab. Chip*, vol. 14, no. 5, pp. 924–930, 2014.

[109] G. Destgeer, A. Alazzam, and H. J. Sung, “High frequency travelling surface acoustic waves for microparticle separation,” *J. Mech. Sci. Technol.*, vol. 30, no. 9, pp. 3945–3952, 2016.

[110] X. Ding *et al.*, “Cell separation using tilted-angle standing surface acoustic waves,” *Proc. Natl. Acad. Sci.*, vol. 111, no. 36, pp. 12992–12997, 2014.

[111] Z. Mao *et al.*, “Experimental and numerical studies on standing surface acoustic wave microfluidics,” *Lab. Chip*, vol. 16, no. 3, pp. 515–524, 2016.

[112] L. Johansson, J. Enlund, S. Johansson, I. Katardjiev, and V. Yantchev, “Surface acoustic wave induced particle manipulation in a PDMS channel—principle concepts for continuous flow applications,” *Biomed. Microdevices*, vol. 14, no. 2, pp. 279–289, 2012.

[113] N. Nama, R. Barnkob, Z. Mao, C. J. Kähler, F. Costanzo, and T. J. Huang, “Numerical study of acoustophoretic motion of particles in a PDMS microchannel driven by surface acoustic waves,” *Lab. Chip*, vol. 15, no. 12, pp. 2700–2709, 2015.

[114] J.-C. Hsu, C.-H. Hsu, and Y.-W. Huang, “Acoustophoretic Control of Microparticle Transport Using Dual-Wavelength Surface Acoustic Wave Devices,” *Micromachines*, vol. 10, no. 1, p. 52, 2019.

[115] P. B. Muller, R. Barnkob, M. J. H. Jensen, and H. Bruus, “A numerical study of microparticle acoustophoresis driven by acoustic radiation forces and streaming-induced drag forces,” *Lab. Chip*, vol. 12, no. 22, pp. 4617–4627, 2012.

[116] J. Lee, C. Rhyou, B. Kang, and H. Lee, “Continuously phase-modulated standing surface acoustic waves for separation of particles and cells in microfluidic channels containing multiple pressure nodes,” *J. Phys. Appl. Phys.*, vol. 50, no. 16, p. 165401, 2017.

[117] W. G. Cady, *Piezoelectricity: Volume Two: An Introduction to the Theory and Applications of Electromechanical Phenomena in Crystals*. Courier Dover Publications, 2018.

[118] W. Wang, Y. Jia, X. Xue, Y. Liang, and Z. Du, “Magnetostrictive effect in micro-dotted FeCo film coated surface acoustic wave devices,” *Smart Mater. Struct.*, vol. 27, no. 10, p. 105040, 2018.

[119] D. Xiang and R. Gordon, “Nanoparticle electrostriction acoustic resonance enhanced nonlinearity,” in *Optical Trapping and Optical Micromanipulation XIII*, 2016, vol. 9922, p. 992223.

[120] M. Hirao and H. Ogi, *Electromagnetic acoustic transducers*. Springer, 2017.

[121] T. Pezeril, “Laser generation and detection of ultrafast shear acoustic waves in solids and liquids,” *Opt. Laser Technol.*, vol. 83, pp. 177–188, 2016.

[122] J. Dual and D. Möller, “Acoustofluidics 4: Piezoelectricity and application in the excitation of acoustic fields for ultrasonic particle manipulation,” *Lab. Chip*, vol. 12, no. 3, pp. 506–514, 2012.

[123] D. J. Collins, A. Neild, and Y. Ai, “Highly focused high-frequency travelling surface acoustic waves (SAW) for rapid single-particle sorting,” *Lab. Chip*, vol. 16, no. 3, pp. 471–479, 2016.

[124] J. Curie and P. Curie, “Contractions and expansions produced by voltages in hemihedral crystals with inclined faces,” *Comptes Rendus*, vol. 93, pp. 1137–1140, 1881.

[125] A. J. Pointon, “Piezoelectric devices,” *IEE Proc. Phys. Sci. Meas. Instrum. Manag. Educ. Rev.*, vol. 129, no. 5, pp. 285–307, 1982.

[126] C. S. Hartmann, “Systems impact of modern Rayleigh wave technology,” in *Rayleigh-Wave Theory and Application*, Springer, 1985, pp. 238–253.

[127] D. J. Collins, “Manipulation in Microfluidic Systems Using Surface Acoustic Waves (SAW),” Monash University, 2014.

[128] S. Bhagavat and I. Kao, “Nanoindentation of lithium niobate: hardness anisotropy and pop-in phenomenon,” *Mater. Sci. Eng. A*, vol. 393, no. 1–2, pp. 327–331, 2005.

[129] K. Shibayama, K. Yamanouchi, H. Sato, and T. Meguro, “Optimum cut for rotated Y-cut LiNbO 3 crystal used as the substrate of acoustic-surface-wave filters,” *Proc. IEEE*, vol. 64, no. 5, pp. 595–597, 1976.

[130] G. Destgeer *et al.*, “Characterization of microchannel anechoic corners formed by surface acoustic waves,” *Appl. Phys. Lett.*, vol. 112, no. 8, p. 083501, 2018.

[131] H. Bruus, T. Laurell, and A. Lenshof, “Perturbation theory and ultrasound resonances,” *Microscale Acoustofluidics Ed T Laurell Lenshof*, pp. 29–45, 2014.

[132] Y. Wu, A. G. Stewart, and P. V. Lee, “On-chip cell mechanophenotyping using phase modulated surface acoustic wave,” *Biomicrofluidics*, vol. 13, no. 2, p. 024107, 2019.

[133] A. Urbansky, P. Ohlsson, A. Lenshof, F. Garofalo, S. Scheding, and T. Laurell, “Rapid and effective enrichment of mononuclear cells from blood using acoustophoresis,” *Sci. Rep.*, vol. 7, no. 1, p. 17161, 2017.

[134] A. M. Soliman, M. A. Eldosoky, and T. E. Taha, “The Separation of Blood Components Using Standing Surface Acoustic Waves (SSAWs) Microfluidic Devices: Analysis and Simulation,” *Bioengineering*, vol. 4, no. 2, p. 28, 2017.

[135] A. Renaudin, J.-P. Sozanski, B. Verbeke, V. Zhang, P. Tabourier, and C. Druon, “Monitoring SAW-actuated microdroplets in view of biological applications,” *Sens. Actuators B Chem.*, vol. 138, no. 1, pp. 374–382, 2009.

[136] G. Destgeer, B. H. Ha, J. H. Jung, and H. J. Sung, "Submicron separation of microspheres via travelling surface acoustic waves," *Lab. Chip*, vol. 14, no. 24, pp. 4665–4672, 2014.

[137] L. V. King, "On the acoustic radiation pressure on spheres," *Proc. R. Soc. Lond. Ser. -Math. Phys. Sci.*, vol. 147, no. 861, pp. 212–240, 1934.

[138] K. Yosioka and Y. Kawasima, "Acoustic radiation pressure on a compressible sphere," *Acta Acust. United Acust.*, vol. 5, no. 3, pp. 167–173, 1955.

[139] S. Li *et al.*, "Standing surface acoustic wave (SSAW)-based cell washing," *Lab. Chip*, vol. 15, no. 1, pp. 331–338, 2015.

[140] J. Nam, H. Lim, C. Kim, J. Yoon Kang, and S. Shin, "Density-dependent separation of encapsulated cells in a microfluidic channel by using a standing surface acoustic wave," *Biomicrofluidics*, vol. 6, no. 2, p. 024120, 2012.

[141] S. M. Ben Khelil and A. Lozzi, "Nano-SAW devices for RFID and sensing applications: study of lithium niobate behavior," 2015.

[142] P. B. Muller and H. Bruus, "Theoretical study of time-dependent, ultrasound-induced acoustic streaming in microchannels," *Phys. Rev. E*, vol. 92, no. 6, p. 063018, 2015.

[143] J.-C. Hsu, Y.-W. Huang, and C.-H. Hsu, "Transportation control of microfluidic particles using mode switching between surface acoustic waves and plate waves," *Jpn. J. Appl. Phys.*, vol. 56, no. 7S1, p. 07JD05, 2017.

[144] J. Guo, Y. Kang, and Y. Ai, "Radiation dominated acoustophoresis driven by surface acoustic waves," *J. Colloid Interface Sci.*, vol. 455, pp. 203–211, 2015.

[145] N. Skov and H. Bruus, "Modeling of microdevices for SAW-based acoustophoresis—a study of boundary conditions," *Micromachines*, vol. 7, no. 10, p. 182, 2016.

[146] H. Bruus, "Acoustofluidics 7: The acoustic radiation force on small particles," *Lab. Chip*, vol. 12, no. 6, pp. 1014–1021, 2012.

[147] K. Beissner, "Acoustic radiation pressure in the near field," *J. Sound Vib.*, vol. 93, no. 4, pp. 537–548, 1984.

[148] R. Barnkob and H. Bruus, "Physics of microparticle acoustophoresis: Bridging theory and experiment," 2012.

[149] Z. Ma, A. Teo, S. Tan, Y. Ai, and N.-T. Nguyen, "Self-aligned interdigitated transducers for acoustofluidics," *Micromachines*, vol. 7, no. 12, p. 216, 2016.

[150] D. Morgan, *Surface acoustic wave filters: With applications to electronic communications and signal processing*. Academic Press, 2010.

[151] J. Shi, H. Huang, Z. Stratton, Y. Huang, and T. J. Huang, "Continuous particle separation in a microfluidic channel via standing surface acoustic waves (SSAW)," *Lab. Chip*, vol. 9, no. 23, pp. 3354–3359, 2009.

[152] R. Zhang, "Acoustic Isolation of Extracellular Vesicles," 2016.

[153] M. Wu, A. Ozcelik, J. Rufo, Z. Wang, R. Fang, and T. J. Huang, "Acoustofluidic separation of cells and particles," *Microsyst. Nanoeng.*, vol. 5, no. 1, p. 32, 2019.

[154] P. Li *et al.*, "Acoustic separation of circulating tumor cells," *Proc. Natl. Acad. Sci.*, vol. 112, no. 16, pp. 4970–4975, 2015.

[155] M. Wu *et al.*, "Acoustic separation of nanoparticles in continuous flow," *Adv. Funct. Mater.*, vol. 27, no. 14, p. 1606039, 2017.

[156] B. A. Auld, *Acoustic fields and waves in solids*. Рипол Классик, 1973.

[157] C. Campbell, *Surface Acoustic Wave Devices for Mobile and Wireless Communications, Four-Volume Set*. Academic press, 1998.

[158] W. Su, H. Li, W. Chen, and J. Qin, "Microfluidic strategies for label-free exosomes isolation and analysis," *TrAC Trends Anal. Chem.*, vol. 118, pp. 686–698, Sep. 2019.

[159] 262588213843476, "Blender python script to export the motion tracking markers to .csv files.," *Gist*. [Online]. Available: https://gist.github.com/anonymous/5663418. [Accessed: 03-Nov-2019].

Appendix

Appendix A: The developed MATLAB code for calculating the Fresnel parameter

```
clc;

close all;

clear;

workspace;  % Make sure the workspace panel is showing



N = input('How many Pressure nodes does this image have: '); % Number of Pressure nodes nodes

[file,ruta] = uigetfile('*.png','Select an image');

cd(ruta);

I = file(:,:,1);

I1 = imread(I);

I2 = I1(:,:,2);

I3 = imadjust(I2);



figure(1)
```

```
imshow(I3)



for i = 1:1:N

    imshow(I3);

    [X, Y, C] = improfile();

    NUM = num2str(i);

    Pre = 'PN';

    Merge = append(Pre, NUM);

    AVE = mean(C ./ max(max(C)));



    [PN_LINE.(Merge)] = struct('Pixel_Value_Vector', ...

        C, 'AVE_Value', AVE);

end

close all;
```

Appendix B: The developed MATLAB code for calculating the Fresnel parameter

```
clear;

clc;

close all;



z = 0;

D_F = 1e-2;

N = 1000;

L = zeros(1, 1);

A = linspace(0.1e-3, 20e-3, N);

F = zeros(1, N);

F1 = zeros(1, N);

X = ones(1, N);



for j = 50e-6 : 50e-6 : 300e-6

    z = z + 1;

    for i = 1 : 1 : N

        L(1, z) = j;
```

```
        F(z, i) = 4 * L(1, z) * D_F ./ ((A(1, i)) .^2);

        F1(z, i) = 4 * L(1, z) * D_F * (1 - 2 * 0.49) ./ ((A(1,
i)) .^2);

    end

    hold on

    plot(A .* 1000, F(z, :))

    xlim ([0 5])

    ylim([0 4])

end

plot(A .* 1000, X)
```